GEOLOGICA ULTRAIECTINA

Mededelingen van de
Faculteit Aardwetenschappen
Universiteit Utrecht

No. 185

Multi-component wavefield separation with application to land seismic data

Sandra M. Richwalski

GEOLOGICA ULTRAIECTINA

Mededelingen van de
Faculteit Aardwetenschappen
Universiteit Utrecht

No. 185

Multi-component wavefield separation with application to land seismic data

Sandra M. Richwalski

Promotor :	Prof. Dr. J.C. Mondt Institute of Earth Sciences Utrecht University
Co-Promotor :	Dr. K. Roy-Chowdhury Institute of Earth Sciences Utrecht University

Members of the dissertation committee :

Dr. J. Brouwer	OYO-Center of Applied Geosciences
Prof. Dr. ir. J.T. Fokkema	Faculty of Applied Earth Sciences Delft University of Technology
Prof. Dr. S.A. Shapiro	Fachrichtung Geophysik Technische Universität Berlin
Prof. Dr. R. Snieder	Institute of Earth Sciences Utrecht University
Prof. Dr. ir. C.P.A. Wapenaar	Faculty of Applied Earth Sciences Delft University of Technology

Multi-component wavefield separation with application to land seismic data

Meer-componenten golfveld separatie
met toepassing op land-seismische gegevens

(met samenvatting in het Nederlands)
(mit einer Zusammenfassung in deutscher Sprache)

PROEFSCHRIFT

TER VERKRIJGING VAN DE GRAAD VAN DOCTOR AAN DE UNIVERSITEIT UTRECHT, OP GEZAG VAN DE RECTOR MAGNIFICUS, PROF. DR H.O. VOORMA, INGEVOLGE HET BESLUIT VAN HET COLLEGE VOOR PROMOTIES IN HET OPENBAAR TE VERDEDIGEN OP WOENSDAG 12 JANUARI 2000 DES NAMIDDAGS TE 2.30 UUR

DOOR

Sandra M. Richwalski

Geboren op 18 september 1969, te Bad Mergentheim

Promotor : Prof. Dr. J.C. Mondt
Institute of Earth Sciences
Utrecht University
Co-Promotor : Dr. K. Roy-Chowdhury
Institute of Earth Sciences
Utrecht University

The research described in this thesis was carried out at :

Department of Geophysics
Utrecht University
PO Box 80021
3508 TA Utrecht
The Netherlands

This work was conducted under the programme of the Vening Meinesz Research School of Geodynamics.

ISBN 90-5744-043-1

Music was my first love and it will be my last.
Music of the future and music of the past.
To live without my music would be impossible to do.
In this world of troubles my music pulls me through.

John Miles, Music, 1976

Für Thomas

Parts of this thesis have been accepted as

Richwalski, S., Roy-Chowdhury, K. and Mondt, J.C. (1999). Practical aspects of wavefield separation of two-component surface seismic data based on polarisation and slowness estimates. *Geophysical Prospecting*.

A manuscript based on Chapter 6 is in preparation for the *European Journal of Environmental and Engineering Geophysics*.

Parts of this thesis have been presented as

Richwalski, S., Mondt, J.C. and Roy-Chowdhury, K. (1997). Wellenfeldtrennung mit Hilfe der Eigenwertanalyse von Mehrkomponentenregistrierungen. 57. Jahrestagung der Deutschen Geophysikalischen Gesellschaft, Potsdam, paper SK29.

Richwalski, S., Roy-Chowdhury, K. and Mondt, J.C. (1998). Multi-component wavefield separation based on polarization and slowness estimates. 60th EAGE Conference Leipzig, *Extended Abstracts*, paper 5-46.

Richwalski, S., Roy-Chowdhury, K. and Mondt, J.C. (1998). Removal of the ground-roll in shallow seismics using multi-component data. *Proceedings of the 4th Meeting of the Environmental and Engineering Geophysical Society (European Section)*, Barcelona, 617-620.

Richwalski, S., Roy-Chowdhury, K. and Mondt, J.C. (1999). Two-component wavefield separation - The challenge of real data. 61th EAGE Conference Helsinki, *Extended Abstracts*, paper P061.

Contents

Chapter 1

INTRODUCTION

The image of the sub-surface obtained from P-wave reflection profiling is only one piece in the seismic jigsaw puzzle. This image may sometimes be the only one we are interested in. S-waves, however, have proven to be of critical importance if we also want to infer information about rock properties from seismic data. Surface waves, normally considered by reflection seismologists an unwanted signal which has to be removed from the recorded data, can further help to complete the puzzle. The trend of (mainly) the S-wave velocity with depth can be deduced from an analysis of these dispersive waves. Each piece of information can be either obtained independently or the puzzle can be solved in a joint manner.

Multi-component seismics aims at recording the full elastic wavefield. Sources should therefore ideally radiate all types of waves with equal strength and the wavefield should be recorded using receivers sensitive in all directions. In practice, P- and S-wave sources together with three-component receivers are used, which leads to the same results with greater expense though. The recorded shot gathers cannot be directly interpreted, but have to be translated first into a suitable image of the sub-surface, most of the time a depth section. Many of the processing steps that take the raw field data to this final depth section are tailored for one wave type only, e.g. Common Midpoint (CMP) sorting or all algorithms that use a velocity profile. One solution to this problem is full wavefield processing, the other is separation of the elastic wavefield into its components and processing of each wave-type independently.

Many separation methods are reported in the literature. They can be divided roughly into two groups: filter methods and elastic decomposition schemes, which both need a priori information about sub-surface parameters, and data dependent methods. Depending on the type and quality of the data and the amount of a priori information available the most suitable method should be chosen.

We decided to evaluate a method presented by Cho and Spencer (1992). It is based on the assumption that the recorded wavefield can locally be considered as being composed of a finite number of plane waves. These have distinct parameters which can be inferred by means of an eigenanalysis in the frequency domain. This **estimation** is carried out using moving analysis windows in a predefined data window. After estimation the very same parameters are used for **separation** of the waves present in the analysis window. If waves differ significantly in amplitude an iterative approach can be used. Only one of the separated waves, the most dominant, is then **projected back** onto the receiver components and **subtracted** from the data. The analysis can then be repeated with the residual data set. These four steps are the basis for applying this method successfully to real data. The analysis of real data is however rendered more difficult by the following issues:

noise, non-linear events, non-continuous events, coupling differences between receiver positions, coupling differences between receiver components, additional time shifts between adjacent receivers (statics), insufficient move-out differences between events, spatial aliasing, and dispersion. We illustrate these effects and show how these issues can be dealt with. A solution, however, could not always be found. Note that since land seismic data are recorded at the surface, they do not record the true motion of the up-going waves, but rather their interaction with the boundary. This interaction gives rise to coupled wave systems, consisting of the up- as well as down-going reflected and converted waves. It will therefore only be possible to estimate the parameters of the coupled system. A decomposition of the coupled systems can be accomplished if the amplitude and the angle of incidence for the up-going wave are known. They can in principle be inferred from the data itself by means of an inversion.

The method is attractive especially for shallow seismics, because it does not need a priori information, is not restricted to certain wave types, can handle dispersive waves, and operates with small apertures. High-resolution P-wave seismics is already a widely applied method for shallow sub-surface exploration for engineering and environmental purposes. Over the last two decades, special equipment has evolved from that used in routine exploration seismic work aiming at greater depths. SH-wave surveys can now be conducted as efficiently as P-wave surveys due to recent developments in S-wave sources. For water-logged sediments as well as for areas with peat layers preventing P-wave energy from penetrating deeper, SH-wave profiling can provide good quality data. S-waves have the additional advantage of mapping material properties more directly. Again, each wave-type on its own and all of them together provide information and should therefore be recorded and interpreted to solve the seismic jigsaw puzzle.

The general goal of this project was to investigate the extent to which elastic wave propagation theory can be used to extract information about the properties of the shallow sub-surface. The seismic image will be of assistance for engineering and environmental purposes as well as for the seismic exploration industry. Sampling the elastic wavefield at different locations in The Netherlands using proper equipment and suitable acquisition geometries, developing processing as well as analysis tools and applying them to the data and evaluating the results were the steps which were taken during this project towards the above mentioned goal.

This thesis is structured as follows:

The theory for two-component wavefield separation method published by Cho and Spencer (1992) is reviewed and extended for three-component data in **Chapter 2**. **Chapter 3** illustrates practical aspects of applying the method to synthetic data. These issues are methodological as well as data related. The application of the method to more realistic data, including effects caused by statics, coupling differences, and the free surface, is presented in **Chapter 4**. In **Chapter 5** results from applying the method to industry data are shown and discussed. Finally, **Chapter 6** focuses on shallow multi-component data. The recorded data are evaluated and results from two- as well as three-component wavefield separation are presented.

Chapter 2

WAVEFIELD SEPARATION: THEORY

2.1 Introduction

Seismic multi-component field observations improve our ability to obtain knowledge of the sub-surface significantly since the combined use of P- and S-wave data provides more accurate information about rock properties than P-wave data alone. The ratio of P- to S-wave velocities, specifically, can be used to determine lithology (e.g. Domenico (1984)), porosity and pore shape (e.g. Robertson (1987)), or pore fluid type (bright spot identification, e.g. Ensley (1984)). Other important parameters for reservoir characterisation are fracture orientation (e.g. Winterstein and Meadows (1991)) and, to some extent, fracture density (e.g. Squires et al. (1989)). These can be deduced from the polarisation direction and the arrival time difference between split S-waves, respectively.

Careful processing of the recorded data is necessary in order to first preserve and later extract this information. Optimal processing requires that the recorded wavefield be first separated into its constituent waves. This may be relatively easy for data from areas where a very low velocity layer at the surface forces the incoming waves to have a near vertical incidence. For an isotropic, horizontally stratified medium, P- and SV-waves (polarised in the vertical plane defined by the source, receiver and reflection point) are then already well separated on the vertical and inline-horizontal receiver components, respectively. For larger offsets, however, or in the absence of such a layer (e.g. carbonate outcrops, volcanic layers, permafrost regions), energy of both wave-types will be recorded on both receiver components. SH-waves, polarised perpendicular to the above mentioned vertical plane, are recorded only on the cross-line horizontal component. In general, however, the recording of events on all three receiver components is expected for a complex sub-surface with dipping layers, inhomogeneities and/or anisotropy.

A number of methods have been developed for wavefield separation. Single trace polarisation filters are mainly useful if waves are not interfering (e.g. Perelberg and Hornbostel (1994)), otherwise the slowness information can be used in addition. Methods operating with two-dimensional transform techniques (f-k or τ-p) implicitly model the input data as the sum of a large number of plane waves: Dankbaar (1985) computes a receiver response filter in the f-k domain to separate P- from SV-waves (recorded at the free surface), that requires a priori information about both velocities in the uppermost layer. Donati and Stewart (1996) use the geophone responses at a liquid-solid interface (sea-bottom) to separate P- from SV-waves. Their algorithm, an extension of Dankbaar's method, works in the τ-p domain and additionally requires the density values of the two layers separated by the interface. Greenhalgh et al. (1990) combine energy from two-component panels in the τ-p domain based on a velocity profile to produce P- or S-wave sections. Additionally,

linearly polarised energy is enhanced before back-transformation. The decomposition scheme proposed by Wapenaar et al. (1991) also needs a priori information. Recently, Schalkwijk et al. (1998) have extended this scheme for ocean-bottom data using the pressure component too. They perform the decomposition in two steps by first separating the data into up- and down-going wavefields and then into P- and S-waves. Using the absence of certain waves on the separated panels as a constraint they can invert for the unknown medium parameters. Another decomposition scheme for land data. proposed by Jin et al. (1998), needs the elastic parameters at the surface. Esmersoy (1990) developed a nonlinear inversion technique for VSP (vertical seismic profile) data by minimising the squared error between observed and modelled spectra. The method needs no a priori information and has a greater lateral resolution than the above mentioned transform techniques since the data are modelled as a superposition of a small number of plane waves. The method was originally developed for separating down-going P- and SV-waves, but was extended by Leaney (1990) to separate down- and up-going P- and SV-waves in order to avoid an extra velocity filtering.

Unfortunately, the methods discussed above suffer from one or more of the following disadvantages: the necessity to include a priori information about the parameters of the uppermost layer, the restriction to certain wave types, the assumption that parameters have to be frequency-independent, the limitation to non-interfering waves, or the necessity to have a large recording aperture.

Cho and Spencer (1992) presented an algorithm to estimate polarisation and slowness from two-component VSP data. Using two interfering plane waves they show that the method is neither sensitive to the overlap in time between the waves nor the similarity in their waveforms (frequency content). In his thesis, Cho (1991) presents the separation of a dispersive Rayleigh wave from a P-wave reflection using noise-free two-component synthetic surface seismic data.

The method is based on the assumption that the wavefield, recorded on equidistant two-component receivers, can be treated locally as being composed of a finite number of plane waves with distinct characteristic parameters: apparent slowness (in case of surface seismics this is the horizontal slowness), polarisation angle, and phase difference between the receiver components. Furthermore, a change in amplitude between adjacent receivers can be considered which is useful if non-planar waves are to be analysed. The method operates in the frequency domain and therefore these parameters are allowed to vary with frequency which makes it possible to also treat dispersive waves. The advantages of this method are that no a priori information about the parameters of the sub-surface is needed, that the method is not restricted to certain wave types, and that the parameters are allowed to vary with frequency. Only an estimate of the number of waves present is required. To keep this number small and ensure a good lateral resolution, the data set has to be divided into data windows. There is a disadvantage this methods shares with the parametric method developed by Esmersoy (1990): the free surface effect is not taken into account. This means that only the parameters of the coupled systems can be estimated, not the ones of the individual up- or down-going waves.

2.2 A review of the method

In the following we give a review of the method that is applied to subsets of the recorded data, limited in time and/or space. These subsets are called **data windows**. The traces in such a subset are analysed by a moving window, which we call the **analysis window**. The minimum number of receivers that form an analysis window is prescribed by the expected number of waves (see Eq. 2.7 below) and the maximum number is restricted by the expected lateral variation of the characteristic parameters. These parameters have to be constant inside the analysis window. Each window consists of several **units**. This is the smallest form of an array and contains the spectra of one or more adjacent two-component receivers. Spectra in two neighbouring units are connected by a so-called transfer matrix (see Eq. 2.5 below) from which the characteristic parameters needed for wavefield separation are deduced by means of an eigenanalysis.

2.2.1 Plane-wave model of the data

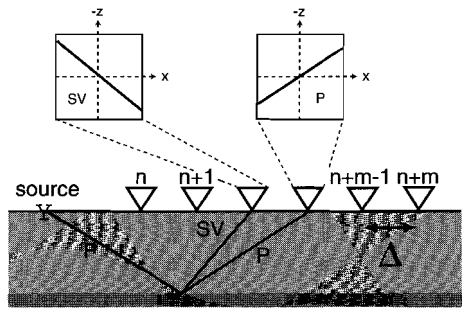

Figure 2.1: *Two-component receivers n through $(n+m)$ are planted at regular intervals Δ at the surface. For a coordinate system with positive axes pointing down and away from the source a phase difference of 180° between the receiver components denotes a P-wave motion and one of 0° an SV-wave motion (both waves have a positive slowness). In the upper part of the figure the corresponding particle motion diagrams are shown.*

Consider $(m+1)$ two-component receivers inside an analysis window, where the first and the last receiver positions are denoted by n and $(n+m)$, respectively (see Fig. 2.1). Transformation of the recorded traces to the frequency domain yields complex spectra and the equations below are valid for each frequency component. The complex spectra $U_i^n, U_i^{n+1}, \cdots, U_i^{n+m}$ can be described as a superposition of spectra of k different plane waves W^j, each propagating with its slowness p^j along the receivers and projected onto the receiver components by its complex polarisation vector $\boldsymbol{a}^j$. Here subscript i refers to either the vertical ($i=3$) or inline-horizontal ($i=1$) component of a receiver and superscript j denotes a certain plane wave. At the first $l+1$ receivers n through $n+l$

(which represents a unit) the recorded spectra can be modelled as:

$$\begin{pmatrix} U_3^n \\ U_1^n \\ \vdots \\ U_3^{n+l} \\ U_1^{n+l} \end{pmatrix} = \begin{pmatrix} a_3^\alpha & a_3^\beta & \cdots & a_3^\kappa \\ a_1^\alpha & a_1^\beta & \cdots & a_1^\kappa \\ \vdots & \vdots & \vdots & \vdots \\ a_3^\alpha (g^\alpha)^l e^{il\Phi^\alpha} & a_3^\beta (g^\beta)^l e^{il\Phi^\beta} & \cdots & a_3^\kappa (g^\kappa)^l e^{il\Phi^\kappa} \\ a_1^\alpha (g^\alpha)^l e^{il\Phi^\alpha} & a_1^\beta (g^\beta)^l e^{il\Phi^\beta} & \cdots & a_1^\kappa (g^\kappa)^l e^{il\Phi^\kappa} \end{pmatrix} \begin{pmatrix} W^\alpha \\ W^\beta \\ \vdots \\ W^\kappa \end{pmatrix} \tag{2.1}$$

or more concisely

$$\boldsymbol{u}^n = \boldsymbol{A}\boldsymbol{w}, \tag{2.2}$$

where Greek letters denote waves characterised by unique characteristic parameter combinations. The parameter l is chosen suitably so as to guarantee that the matrix $\boldsymbol{A}$ is square, i.e. $l = \frac{k-2}{2}$. The unit consists of only one receiver if $k = 2$ and the equations reduce to the original ones given by Cho and Spencer (1992). The parameters g^j and Φ^j represent changes in amplitude and phase differences, respectively, relative to the neighbouring receiver. With Δ representing the distance between the receivers, the phase difference is given by:

$$\Phi^j = \frac{p^j}{2\pi f \Delta}. \tag{2.3}$$

The spectra at the adjacent unit (receivers $n+1$ through $n+1+l$) can be written as the time-shifted and scaled versions of the spectra at the first unit:

$$\boldsymbol{u}^{n+1} = \boldsymbol{A}\boldsymbol{\Lambda}\boldsymbol{w}. \tag{2.4}$$

The matrix $\boldsymbol{\Lambda}$ is diagonal with elements $g^j e^{i\Phi^j}$. In order to eliminate the unknown waves W^j from the computation, Eq. 2.4 can be rewritten using Eq. 2.2:

$$\boldsymbol{u}^{n+1} = \boldsymbol{A}\boldsymbol{\Lambda}\boldsymbol{A}^{-1}\boldsymbol{u}^n = \boldsymbol{Y}\boldsymbol{u}^n. \tag{2.5}$$

The transfer matrix $\boldsymbol{Y}$ is a square $k \times k$ matrix, where k is the maximum number of waves expected in the data. For two-component data k must be chosen even for symmetry reasons.

The matrix $\boldsymbol{Y}$ contains the information about the characteristic parameters of the different plane waves. Its estimation can only be accomplished by including more receivers. It is assumed that the characteristic parameters do not change inside the analysis window containing $(m+1)$ receivers, i.e. all receiver units of length $\frac{k}{2}$ inside this window are connected by the same transfer matrix (plane-wave assumption). Then all receiver units

can be used and Eq. 2.5 can be rewritten in the following (general) form:

$$\begin{pmatrix} U_3^{n+1} & U_3^{n+2} & \dots & U_3^{n+m-l} \\ U_1^{n+1} & U_1^{n+2} & \dots & U_1^{n+m-l} \\ \vdots & \vdots & \vdots & \vdots \\ U_3^{n+1+l} & U_3^{n+2+l} & \dots & U_3^{n+m} \\ U_1^{n+1+l} & U_1^{n+2+l} & \dots & U_1^{n+m} \end{pmatrix} = \boldsymbol{Y} \begin{pmatrix} U_3^{n} & U_3^{n+1} & \dots & U_3^{n+m-1-l} \\ U_1^{n} & U_1^{n+1} & \dots & U_1^{n+m-1-l} \\ \vdots & \vdots & \vdots & \vdots \\ U_3^{n+l} & U_3^{n+1+l} & \dots & U_3^{n+m-1} \\ U_1^{n+l} & U_1^{n+1+l} & \dots & U_1^{n+m-1} \end{pmatrix}$$

or more concisely

$$\boldsymbol{V}^{n+1} = \boldsymbol{Y}\boldsymbol{V}^{n}. \tag{2.6}$$

Both matrices $\boldsymbol{V}^n$ and $\boldsymbol{V}^{n+1}$ are of size $2(l+1) \times 2(l+1)$, which is identical to $k \times k$. The minimum number of receivers in the analysis window is determined by the number of receivers to fill matrix $\boldsymbol{V}^n$, which is $2(l+1)$, and an additional adjacent unit of length $l+1$. This can also be written as:

$$m + 1 = k + \frac{k}{2}. \tag{2.7}$$

Note that for $k = 2$ there are only 2 rows in both matrices. If more receivers are used than minimally required (e.g. in the presence of noise) then $\boldsymbol{V}^n$ is not square and a least squares solution of Eq. 2.6 can be used to obtain the transfer matrix:

$$\boldsymbol{Y} = \boldsymbol{V}^{n+1}\boldsymbol{V}^{n\dagger}\left[\boldsymbol{V}^{n}\boldsymbol{V}^{n\dagger}\right]^{-1}, \tag{2.8}$$

where † denotes complex conjugate transpose.

2.2.2 Eigenanalysis of the transfer matrix

The transfer matrix $\boldsymbol{Y}$ holds all the information about the different plane waves: slowness, polarisation state and amplitude change factor. These parameters can be retrieved if an eigenanalysis is performed on this matrix: the polarisation state of a plane wave is considered constant over the analysis window but there is a constant phase shift and a possible scaling factor involved. Using Eq. 2.5 one can then write: $\boldsymbol{Y}\boldsymbol{A} = \boldsymbol{A}\boldsymbol{\Lambda}$. $\boldsymbol{\Lambda}$ contains the complex eigenvalues $g^\alpha e^{i\Phi^\alpha}$ which shift and scale the plane waves. Per frequency, the horizontal slowness can be computed from the phase of the eigenvalues (see Eq. 2.3); as the eigenproblem is solved for each frequency, dispersive waves can be handled. The columns of matrix $\boldsymbol{A}$ represent the complex eigenvectors (see Eq. 2.1). They have k elements, but only the first two unscaled ones are needed for two-component data. They are identical to the complex polarisation vector $\boldsymbol{a}^j$. The vector can be rotated (normalised) such that its inline-component lies on the real axis (see Fig. 2.2):

$$\boldsymbol{a}^j = \begin{pmatrix} \sin\theta^j e^{i\xi^j} \\ \cos\theta^j \end{pmatrix}. \tag{2.9}$$

This polarisation vector describes the polarisation state of a wave: its magnitudes represent the maximum amplitudes measured on the vertical and inline-horizontal receiver components. The phase difference ξ between the components of the polarisation vector gives information about the ellipticity of the wave. For a coordinate system with positive z- and x-axis pointing down and away from the source, respectively, a phase difference of 180° describes a P-wave motion and one of 0° an SV-wave motion for waves with a positive slowness (see Fig. 2.1). The ratio of the magnitudes (giving the polarisation angle θ) can then be directly related to the tilt angle of the particle motion ellipse measured from the positive x-axis (e.g. Born and Wolf (1964)).

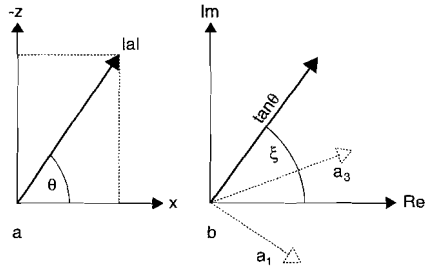

Figure 2.2: *Graphical representations of the complex polarisation vector. a: The magnitude of the vector projected onto the xz-plane. θ is the polarisation angle and should not be confused with the tilt angle of the particle motion ellipse (angle between the horizontal axis and the major axis of the ellipse). Their magnitude is the same only for linearly polarised waves. b: Dotted arrows indicate the original complex vector components. They are rotated such that the inline-horizontal component becomes parallel to the real axis. The magnitude of the complex-plane polarisation representation (solid arrow) is given by the ratio between the magnitudes of the vector components. The phase difference between the receiver components is denoted by ξ.*

2.2.3 Wavefield separation

Once the characteristic parameters of the waves have been determined, they can be used for wavefield separation (Cho, 1991). This is achieved by rewriting Eq. 2.2:

$$\tilde{\boldsymbol{u}} = \boldsymbol{P}\boldsymbol{w}, \tag{2.10}$$

where the spectra of all $(m + 1)$ traces which have been used to estimate the characteristic parameters are now included in the vector $\tilde{\boldsymbol{u}}$. According to the model of Eq. 2.10 a

matrix ($\boldsymbol{P}$) has to be constructed that uses the estimated parameters to describe the mapping of the waves collected in $\boldsymbol{w}$ at the different receiver positions and components of $\tilde{\boldsymbol{u}}$. The mapping is accomplished by projecting the waves onto the components using the polarisation vectors and propagating them along the receivers using the phase differences. This propagation is done relative to a reference receiver, for symmetry reasons preferably situated in the centre of the analysis window (an odd number of traces is then required):

$$\boldsymbol{P} = \begin{pmatrix} a_3^\alpha e^{-i\tilde{m}\Phi_\alpha} & a_3^\beta e^{-i\tilde{m}\Phi_\beta} & \cdots & a_3^\kappa e^{-i\tilde{m}\Phi_\kappa} \\ a_1^\alpha e^{-i\tilde{m}\Phi_\alpha} & a_1^\beta e^{-i\tilde{m}\Phi_\beta} & \cdots & a_1^\kappa e^{-i\tilde{m}\Phi_\kappa} \\ \vdots & \vdots & \vdots & \vdots \\ a_3^\alpha & a_3^\beta & \cdots & a_3^\kappa \\ a_1^\alpha & a_1^\beta & \cdots & a_1^\kappa \\ \vdots & \vdots & \vdots & \vdots \\ a_3^\alpha e^{i\tilde{m}\Phi_\alpha} & a_3^\beta e^{i\tilde{m}\Phi_\beta} & \cdots & a_3^\kappa e^{i\tilde{m}\Phi_\kappa} \\ a_1^\alpha e^{i\tilde{m}\Phi_\alpha} & a_1^\beta e^{i\tilde{m}\Phi_\beta} & \cdots & a_1^\kappa e^{i\tilde{m}\Phi_\kappa} \end{pmatrix},$$

where $\tilde{m} = \frac{m}{2}$. The scaling factors are omitted at this step to enable the reconstruction of each individual wave with its offset-dependent amplitudes. From Eq. 2.10 the recorded spectra are decomposed into the different waves as (least squares solution):

$$\boldsymbol{w} = \left[\boldsymbol{P}^\dagger \boldsymbol{P}\right]^{-1} \boldsymbol{P}^\dagger \tilde{\boldsymbol{u}}. \tag{2.11}$$

One output spectrum is computed for each wave. The original arrival times are reconstructed automatically at the reference receiver because only a projection and no phase shift is applied to the data at this location.

2.3 Extension to three-component data

Two-component data represent only a part of the full wavefield that can propagate through a complex sub-surface, so that ultimately three-component receivers should be used. The recordings are still done in two dimensions and therefore no discrimination can be made between positive and negative azimuths of arriving waves. Such out-of-plane arrivals have to comply with the plane-wave assumption of course.

The recorded wavefield can be decomposed using the theory presented in Section 2.2 extended for the recordings from the crossline-horizontal receiver component which is

identified by the subscript $i = 2$. Eq. 2.1, for example, is then rewritten as:

$$\begin{pmatrix} U_3^n \\ U_2^n \\ U_1^n \\ \vdots \\ U_3^{n+l} \\ U_2^{n+l} \\ U_1^{n+l} \end{pmatrix} = \begin{pmatrix} a_3^\alpha & a_3^\beta & \cdots & a_3^\kappa \\ a_2^\alpha & a_2^\beta & \cdots & a_2^\kappa \\ a_1^\alpha & a_1^\beta & \cdots & a_1^\kappa \\ \vdots & \vdots & \vdots & \vdots \\ a_3^\alpha (g^\alpha)^l e^{il\Phi^\alpha} & a_3^\beta (g^\beta)^l e^{il\Phi^\beta} & \cdots & a_3^\kappa (g^\kappa)^l e^{il\Phi^\kappa} \\ a_2^\alpha (g^\alpha)^l e^{il\Phi^\alpha} & a_2^\beta (g^\beta)^l e^{il\Phi^\beta} & \cdots & a_2^\kappa (g^\kappa)^l e^{il\Phi^\kappa} \\ a_1^\alpha (g^\alpha)^l e^{il\Phi^\alpha} & a_1^\beta (g^\beta)^l e^{il\Phi^\beta} & \cdots & a_1^\kappa (g^\kappa)^l e^{il\Phi^\kappa} \end{pmatrix} \begin{pmatrix} W^\alpha \\ W^\beta \\ \vdots \\ W^\kappa \end{pmatrix}.$$

Eq. 2.7, which determines the minimum number of receivers needed to separate k wavefields from each other, now reads:

$$m + 1 = k + \frac{k}{3}.$$

The rotated polarisation vector (see Eq. 2.9 and Fig. 2.3) is now represented by:

$$\boldsymbol{a}^j = \begin{pmatrix} \sin\theta^j e^{i\xi^j} \\ \cos\theta^j \sin\psi^j e^{i\zeta^j} \\ \cos\theta^j \cos\psi^j \end{pmatrix},$$

with ψ describing the amplitude ratio between the sagittal plane, defined by the vertical and inline horizontal direction, and the crossline-horizontal direction. The phase difference between the two horizontal components is described by ζ. If ζ is either 0.° or 180.° then the directional angle ψ can directly be related to the azimuth.
Wavefield separation is achieved using Eq. 2.11, where $\boldsymbol{P}$ is now:

$$\boldsymbol{P} = \begin{pmatrix} a_3^\alpha e^{-i\tilde{m}\Phi_\alpha} & a_3^\beta e^{-i\tilde{m}\Phi_\beta} & \cdots & a_3^\kappa e^{-i\tilde{m}\Phi_\kappa} \\ a_2^\alpha e^{-i\tilde{m}\Phi_\alpha} & a_2^\beta e^{-i\tilde{m}\Phi_\beta} & \cdots & a_2^\kappa e^{-i\tilde{m}\Phi_\kappa} \\ a_1^\alpha e^{-i\tilde{m}\Phi_\alpha} & a_1^\beta e^{-i\tilde{m}\Phi_\beta} & \cdots & a_1^\kappa e^{-i\tilde{m}\Phi_\kappa} \\ \vdots & \vdots & \vdots & \vdots \\ a_3^\alpha & a_3^\beta & \cdots & a_3^\kappa \\ a_2^\alpha & a_2^\beta & \cdots & a_2^\kappa \\ a_1^\alpha & a_1^\beta & \cdots & a_1^\kappa \\ \vdots & \vdots & \vdots & \vdots \\ a_3^\alpha e^{i\tilde{m}\Phi_\alpha} & a_3^\beta e^{i\tilde{m}\Phi_\beta} & \cdots & a_3^\kappa e^{i\tilde{m}\Phi_\kappa} \\ a_2^\alpha e^{i\tilde{m}\Phi_\alpha} & a_2^\beta e^{i\tilde{m}\Phi_\beta} & \cdots & a_2^\kappa e^{i\tilde{m}\Phi_\kappa} \\ a_1^\alpha e^{i\tilde{m}\Phi_\alpha} & a_1^\beta e^{i\tilde{m}\Phi_\beta} & \cdots & a_1^\kappa e^{i\tilde{m}\Phi_\kappa} \end{pmatrix}.$$

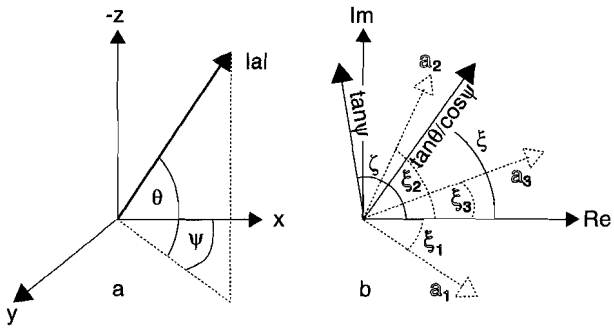

Figure 2.3: *Graphical representations of the complex polarisation vector. a: The magnitude of the vector projected onto the xyz-plane. θ is the polarisation angle and ψ the directional angle. b: Dotted arrows indicate the original complex vector components. They are rotated such that the inline-horizontal component becomes parallel to the real axis. Each magnitude of the complex-plane polarisation representation (solid arrow) is given by the ratio between the magnitudes of the respective vector components. ξ gives the phase difference between the vertical and inline-horizontal receiver components, ζ between the two horizontal components.*

2.4 Noise

Seismic energy other than primary reflections is often considered as **noise**. This term refers to the unwanted signals also recorded by the geophones, which will be attenuated or removed from the seismic data by appropriate processing. Noise can have different sources and is therefore characterised more precisely by the following terms: **coherent noise** includes all non-reflection coherent events triggered by the source; **random noise** describes the non-coherent energy which can be attenuated by adding records of independent measurements (vertical stacking); **ambient noise** refers to background noise, including seismic energy coming from other sources.
Coherent noise is characterised by a certain apparent slowness and polarisation state and can be treated as an extra wavefield. In the following the focus will be on random noise having zero mean.

2.4.1 Two-component formulation

Noise is introduced into the plane-wave model by adding a vector containing the noise spectra N_i for each frequency component to the right-hand side of Eq. 2.2:

$$\boldsymbol{u}^n = \boldsymbol{A}\boldsymbol{w} + \boldsymbol{n}^n,$$

with

$$\boldsymbol{n}^n = \begin{pmatrix} N_3^n & N_1^n & \cdots & N_3^{n+l} & N_1^{n+l} \end{pmatrix}^T.$$

Eq. 2.4 then reads:

$$\boldsymbol{u}^{n+1} = \boldsymbol{A}\boldsymbol{\Lambda}\boldsymbol{w} + \boldsymbol{n}^{n+1} = \boldsymbol{A}\boldsymbol{\Lambda}\boldsymbol{A}^{-1}(\boldsymbol{u}^{n} - \boldsymbol{n}^{n}) + \boldsymbol{n}^{n+1}$$

and Eq. 2.5:

$$(\boldsymbol{u}^{n+1} - \boldsymbol{n}^{n+1}) = \boldsymbol{A}\boldsymbol{\Lambda}\boldsymbol{A}^{-1}(\boldsymbol{u}^{n} - \boldsymbol{n}^{n}) = \boldsymbol{Y}(\boldsymbol{u}^{n} - \boldsymbol{n}^{n}).$$

The random noise recorded on the different traces is spatially uncorrelated so that in principle only the auto-spectra belonging to the two components are present in the least squares solution (Eq. 2.8) which can be rewritten as:

$$\boldsymbol{Y} = \boldsymbol{V}^{n+1}\boldsymbol{V}^{n\dagger}\left[\boldsymbol{V}^{n}\boldsymbol{V}^{n\dagger} + \boldsymbol{D}\right]^{-1}, \tag{2.12}$$

where $\boldsymbol{D}$ is a square $k \times k$ diagonal matrix having non-zero values only on the main diagonal, namely the sum of the auto-spectra (noise energy) for the respective sub-windows:

$$\boldsymbol{D} = \begin{pmatrix} \delta_3^n & 0 & \cdots & 0 & 0 \\ 0 & \delta_1^n & \cdots & 0 & 0 \\ \vdots & \vdots & \vdots & \vdots & \vdots \\ 0 & 0 & \vdots & \delta_3^{n+l} & 0 \\ 0 & 0 & \cdots & 0 & \delta_1^{n+l} \end{pmatrix}. \tag{2.13}$$

Cross-spectra off the diagonal resulting from the correlation between the two receiver components at the same location might differ from zero. They are however expected to be less significant than the main diagonal elements, since the cross-spectra themselves are spatially uncorrelated.

Outside the signal bandwidth $\boldsymbol{V}^{n}\boldsymbol{V}^{n\dagger}$ as well as $\boldsymbol{V}^{n+1}\boldsymbol{V}^{n\dagger}$ contain zeroes and the transfer matrix will be the inverse of matrix $\boldsymbol{D}$. Provided the signal-to-noise (S/N) ratio is sufficient, $\boldsymbol{D}$ will add only little energy to the main diagonal of $\boldsymbol{V}^{n}\boldsymbol{V}^{n\dagger}$ inside the signal bandwidth. Since only the parameters estimated at these frequencies have meaningful values it is desirable to discriminate between frequencies outside and inside the signal bandwidth. The least squares solution in Eq. 2.12 can be rewritten as a damped least squares solution if a matrix $\tilde{\boldsymbol{D}}$ is added. This matrix is also square and diagonal and its elements on the main diagonal are damping factors which have to be chosen such that the eigenvalues inside the signal bandwidth are modified only slightly while outside they are affected such that their value decreases rapidly. Cho and Spencer (1992) proposed to compute the diagonal elements of $\tilde{\boldsymbol{D}}$ from an estimate of the average S/N ratio on receiver

component j for an analysis window in which the first receiver is denoted by n:

$$(r_i^n)^2 = \frac{\int_{f_L}^{f_H} \langle \boldsymbol{U}_i^n, \boldsymbol{U}_i^n \rangle \, df - \int_{f_L}^{f_H} \langle \boldsymbol{N}_i^n, \boldsymbol{N}_i^n \rangle \, df}{\int_{f_L}^{f_H} \langle \boldsymbol{N}_i^n, \boldsymbol{N}_i^n \rangle \, df} \tag{2.14}$$

$$= \frac{\overbrace{E_i^n}^{\text{total energy}} - \overbrace{\delta_i^n (f_H - f_L)}^{\text{noise energy}}}{\delta_i^n (f_H - f_L)}, \tag{2.15}$$

where $\langle \quad \rangle$ stands for the sum of all auto-spectra (power spectra) inside the analysis window starting at receiver n. The lower and upper frequencies of the observed signal are denoted by f_L and f_H, respectively. An estimate of the i-directional S/N ratio can therefore be transferred into a frequency independent noise energy, provided the noise is uniformly distributed over the frequency band. The damping factors $\tilde{\delta}_i$ are computed from the estimated S/N ratio:

$$\tilde{\delta}_i^n = \frac{E_i^n}{(f_H - f_L)((r_i^n)^2 + 1)}. \tag{2.16}$$

We also call the estimated S/N ratio r_i **assumed S/N ratio** because we do not explicitly compute this parameter from the data, but assign a value after visual inspection.

2.4.2 Three-component formulation

The damping for three-component data is achieved by introducing δ_2 into Eq. 2.13:

$$\boldsymbol{D} = \begin{pmatrix} \delta_3^n & 0 & 0 & \cdots & 0 & 0 & 0 \\ 0 & \delta_2^n & 0 & \cdots & 0 & 0 & 0 \\ 0 & 0 & \delta_1^n & \cdots & 0 & 0 & 0 \\ \vdots & \vdots & \vdots & \cdots & \vdots & \vdots & \vdots \\ 0 & 0 & 0 & \cdots & \delta_3^{n+l} & 0 & 0 \\ 0 & 0 & 0 & \cdots & 0 & \delta_2^{n+l} & 0 \\ 0 & 0 & 0 & \cdots & 0 & 0 & \delta_1^{n+l} \end{pmatrix}.$$

The crossline-horizontal damping factor $\tilde{\delta}_2$ can be computed by Eq. 2.16 from the estimated S/N ratio on that receiver component.

Chapter 3

TWO-COMPONENT WAVEFIELD SEPARATION: PRACTICAL ASPECTS

3.1 Introduction

Although the approach appears straightforward, using the wavefield separation method reviewed in Chapter 2 in realistic situations involves a number of practical issues. In this chapter we will discuss the method and its practical aspects using synthetic data containing pure plane waves. We start with a demonstration of applying the method to a synthetic plane-wave data set. Then we discuss a number of practical issues related to using the method in realistic situations. (i) We illustrate and discuss the problems that are encountered while tracking the eigenvalues of a wave over its entire signal bandwidth. (ii) We show how a statistical analysis of the characteristic parameter estimates can solve the problem of eigenvalue tracking thereby achieving a robust estimate even in the presence of noise. We also point out how this statistical analysis can be modified to account for spatial aliasing. (iii) We present a new approach which applies the method iteratively to data containing waves differing significantly in amplitude. (iv) We discuss and illustrate the possibilities to increase the robustness of the method if noise is present. (v) We show that the method is not sensitive to the overlap in time between events nor the similarity in frequency content. (vi) Finally, we demonstrate the possibility of estimating a frequency dependent slowness curve for the separation of dispersive waves. Some of the issues are mainly related to methodological problems (i and partly ii) the others are mainly data dependent.

3.2 Example application to synthetic data

The synthetic data set shown in Fig. 3.1 contains four plane waves, one P-, two S- and one Rayleigh wave, recorded by two-component receivers (for modelling parameters see Table 3.1). All waves have the same amplitude prior to projection onto the receiver components. The S/N (signal to noise) ratio on each trace is 10 and is defined as the peak amplitude of the signal divided by 1.4 times the root-mean-square (rms) amplitude of the noise. The bandwidth of the noise is the same as that of the total signal. Trace separation is 5 m and a sliding analysis window of 7 traces was used in the analysis. In Fig. 3.2 separated and original waves (prior to projection onto the receiver components) are plotted in the same frame for comparison. In general, all waves were recovered quite well. There are a number of traces where poor estimation for one parameter of one of the waves leads to leakage of energy onto the other waves, e.g. trace 11 in Fig. 3.2, where a completely

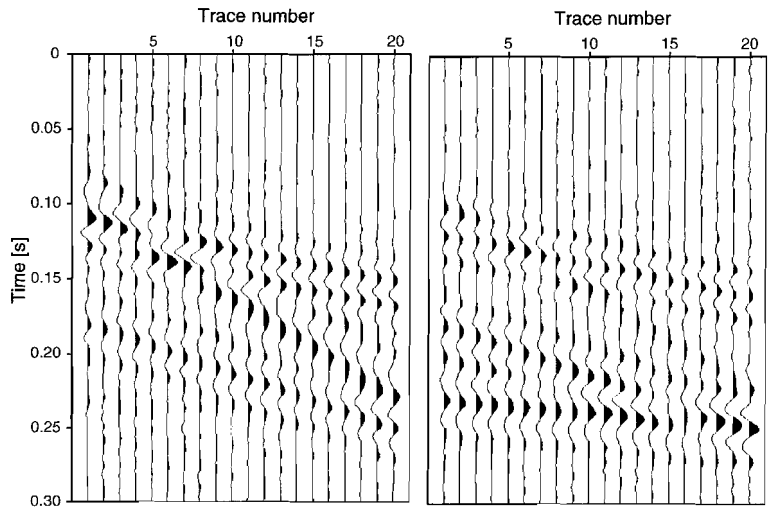

Figure 3.1: *Vertical (left) and inline-horizontal (right) component of the example synthetic data. The characteristic parameters can be found in Table 3.1. Note: All panels in Figs. 3.1 and 3.2 have a common amplitude scaling.*

wave type	f_c [Hz]	T_{start} [ms]	p [s/km]	θ [°]	Amp
P-wave	60	120	0.43	50	1
S-wave	50	180	0.74	40	1
S-wave	40	230	0.20	10	1
Rayleigh wave	35	100	1.28	66	1

Table 3.1: *Modelling parameters for synthetic data of Fig. 3.1. f_c denotes the central frequency of the wavelet (bandwidth is 50 Hz), T_{start} shows where the main peak of the wavelet is placed in time on the first trace, p is the horizontal slowness, θ the polarisation angle, and Amp relates to the multiplication factor that was used prior to projection of the wave onto the receiver components.*

incorrect slowness and polarisation angle estimate for the Rayleigh wave causes the leakage. Lateral filtering (smoothing) of the estimates, which are obtained independently for each analysis window, would improve these results, but is not used here yet. The results shown later in Chapters 5 and 6 were obtained by applying smoothing and interpolation to the estimates. Visually remarkable is the improvement in the S/N ratio due to averaging the spectra of 7 two-component traces in the separation procedure (see Eq. 2.11).

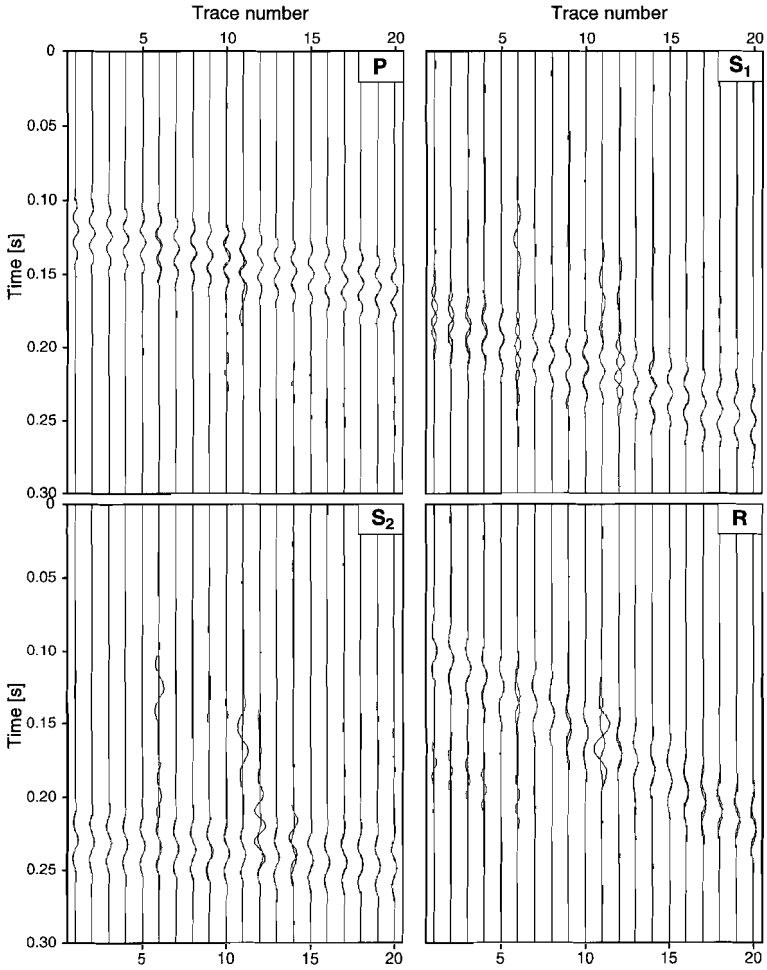

Figure 3.2: *Separated and original waves (prior to projection onto the receiver components) are plotted in the same frame for comparison: P-, first S-, Rayleigh and second S-wave (clockwise from the upper left). Note: All panels in Figs. 3.1 and 3.2 have a common amplitude scaling.*

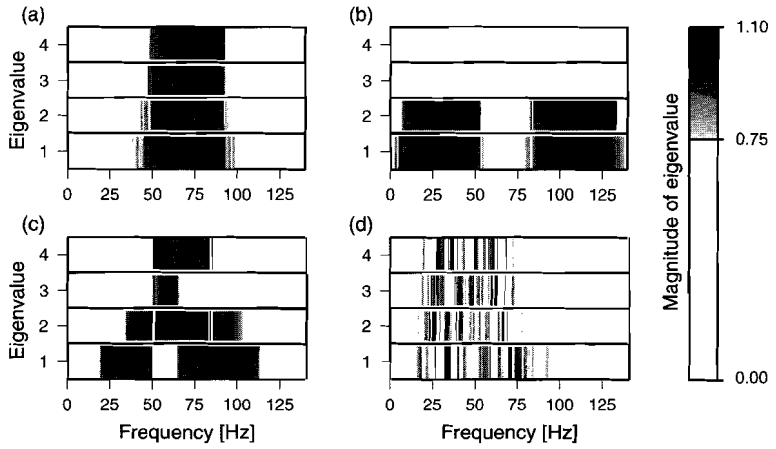

Figure 3.3: *Number of significant eigenvalues for synthetic data (a through c without noise): Those frequencies where the magnitudes of the eigenvalues exceed 0.75 are shown using a linear grey-scale. The data sets always contain four interfering wavefields with varying central frequencies but equal bandwidth. a: central frequencies of 70, 70, 70, 70 Hz; b: 30, 30, 110, 110 Hz; c: 45, 60, 75, 90 Hz; d: typical example taken from the synthetic data shown in Fig. 3.1 with central frequencies of 35, 40, 50, 60 Hz.*

3.3 Eigenvalue sharing and switching

The number of significant eigenvalues at each frequency depends on the number of waves present at this frequency. These eigenvalues have magnitudes close to one in case of plane waves travelling in an elastic medium (see Chapter 2). This situation is illustrated in Fig. 3.3. Magnitudes are plotted using a linear grey-scale if they exceed the value of 0.75. In the case of Fig. 3.3a four plane waves are present in the data. They all have the same central frequency of 70 Hz and a bandwidth of 50 Hz. Therefore, all four magnitudes show significant values over this bandwidth. We then analyse two sets of two plane waves, one set having a central frequency of 30 Hz, the other of 110 Hz (bandwidth is again 50 Hz). Both sets are well separated in the frequency domain. Fig. 3.3b shows that only two out of four magnitudes have significant values, because at every frequency point there are only two waves present. We refer to this behaviour as **eigenvalue sharing**, since one eigenvalue contains information for more than one wave over the entire frequency range. These figures do not show that the direct connection between a wave and a certain eigenvalue over the entire bandwidth of the wave is missing. This **eigenvalue switching** can happen because we compute the eigenvalues at each frequency independently (using a routine from the NAPACK software package). The eigenvalue switching is illustrated in Fig. 3.3c. The central frequencies of the plane waves are 45, 60, 75 and 90 Hz and the bandwidth is again 50 Hz, which means that the waves are overlapping in the frequency domain. The overlap is such that coming from low (or high) frequencies there is first only

one wave present. From 35 Hz (100 Hz) on two waves are present, from 50 Hz (85 Hz) three and between 65 and 70 Hz four waves. Since we need as many eigenvalues as waves, we expect a sort of pyramidal structure in Fig. 3.3c. We see however that eigenvalues #3 and #4 are interchanged and that eigenvalue #3 shows significant values from 50 Hz onwards already, values that are missed in eigenvalue #1.
These examples show that the number of significant eigenvalues depends indeed on the number of waves present at each frequency (eigenvalue sharing). They also show that one wave can be represented by different eigenvalues for its different frequency components (eigenvalue switching). Cho (personal communication) has overcome this problem by ordering the eigenvalues in the complex plane. We have found that this is only possible if the S/N ratio is high or many traces are used in the analysis (effectively increasing the S/N ratio) so that sudden changes in the fairly smooth magnitude curve can be detected well. In Fig. 3.3d the central frequencies are 35, 40, 50 and 60 Hz (bandwidth is 50 Hz). This example is taken from the data shown in Fig. 3.1. Note that now noise is present in the data leading to magnitude curves that are not smooth any more. It is not possible to deduce the bandwidth of the waves from this graph and it now becomes clear that we have to change the approach from using the frequency dependent curves to a statistical one.

3.4 Statistical analysis of the characteristic parameter estimates

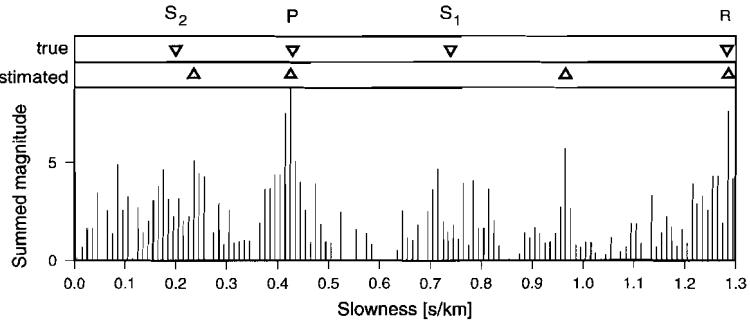

Figure 3.4: *Slowness histogram of synthetic data shown in Fig. 3.1. Traces 2 to 8 have been used in the analysis producing the output trace 5 in Fig. 3.2. The symbols in the upper part of the figure mark the estimated (triangles) and true values (inverted triangles).*

A statistical analysis of the characteristic parameter estimates can be used to overcome the problem of eigenvalue sharing and switching and to increase the robustness of the method in the presence of random noise. The estimates are collected into bins with a certain bin size and for all frequencies for which an estimate fits into the bin the magnitudes of the corresponding eigenvalues are summed. The possible dependence on frequency is hereby not preserved. The resulting data are plotted as a histogram and from its maxima the

characteristic parameters are derived. For low S/N ratios there might be no sharp peaks in the histogram but rather broad ones, which can lead to twice picking a similar value. Therefore, we define a so-called **exclusion distance** that prescribes a certain distance between successive maxima.
In Fig. 3.4 an example of a histogram is shown. Traces 2 to 8 of the synthetic data shown in Fig. 3.1 were used to finally produce the output trace 5 in Fig. 3.2. The slownesses were estimated well except for the S-wave denoted by S_1. If we look at Fig. 3.2, however, the separation on trace 5 is acceptable. Only a small part of the energy of the first S-wave S_1 leaks to the separated P-wave panel P as seen in the upper left part of the figure. Approximately the same amount of leakage is seen in the separated Rayleigh-wave panel R in the lower right part of the figure. Note that without the definition of an exclusion area we would have picked another velocity close to that of the P-wave. In contrast to its neighbour, trace 6 suffers severe leakage of energy (e.g. Rayleigh-wave energy on all panels). In order to explain this we looked at the corresponding histogram and found that apart from an overall increase in error the estimation for the Rayleigh wave is completely incorrect (0.13 s/km instead of 1.28 s/km).
The statistically estimated parameters are collected into groups of three (apparent slowness, polarisation angle and phase difference), each group representing one possible wave. A consistency check has to be performed to make sure that the correct grouping has been carried out. The number of possible combinations increases rapidly with the number of waves: $(k!)^2$. To avoid this we use only those frequencies for determination of the parameters, which build up a maximum for one of the characteristic parameters, preferably the slowness which is the single most differentiating one. We call this procedure **back-tracing**. However, this procedure can only be successful if the slowness is determined well. A totally incorrect estimate of the slowness will of course lead to incorrect estimates of both the polarisation angle and the phase difference. This is the reason for the poor separation of the waves as seen on trace 6 in Fig. 3.2.
The chosen bin-size determines the maximum accuracy with which the characteristic parameters can be estimated. In general, the bin-size should be chosen according to the expected standard deviation of the characteristic parameter estimates. Alternatively, we can decrease the bin-size until well-defined maxima in the histogram start to split up into neighbouring bins. It is also possible to shift the bins by a fraction of the bin-size to increase the resolution. The choice of the optimum exclusion distance depends on the data quality and a priori knowledge and might be adjusted after inspection of the histograms. Plotting the histograms for all analysis windows side by side provides an effective way to check the results of each analysis. Based on those plots for each parameter, missing or incorrectly estimated parameters can be interpolated from neighbouring analysis windows.
If a wave is spatially aliased, then Eq. 2.3 is only valid for frequencies below the first phase wrap. This low-frequency part of the phase curve may not contain enough points for a stable estimate. If there is no eigenvalue switching or sharing, one can simply unwrap the phase curve and proceed with the above mentioned method. Under normal circumstances, eigenvalue switching and sharing occurs and a modification of the statistical analysis is necessary (see Fig. 3.5). Given a slowness range we compute a number of theoretical (wrapped) phase curves sampled at equidistant slopes. The binning around these curves

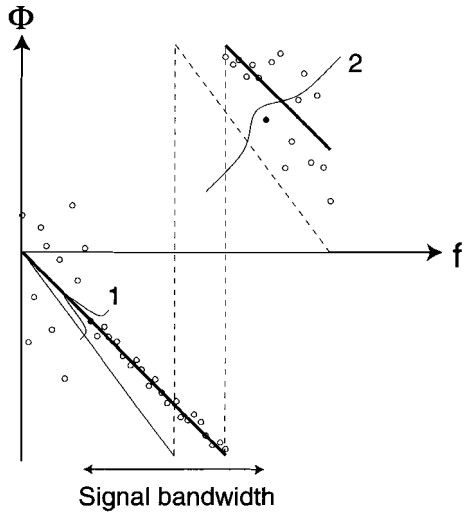

Figure 3.5: *Sketch of the statistical analysis for spatially aliased waves. The open circles represent the phase values estimated at each frequency. The signal bandwidth is indicated at the bottom of the figure. Two theoretical phase curves are shown. For the filled circles the standard deviation is indicated by the Gaussian curves. Situation 1: This phase value contributes mainly to one phase curve. Situation 2: This phase value lies outside the signal bandwidth and contributes little to both phase curves.*

can be done in many ways. We assign to each phase value a standard deviation derived from the magnitude of the corresponding eigenvalue. Then we assume a Gaussian error distribution and compute the probability for each phase value to contribute to a theoretical phase curve. Phase values outside the signal bandwidth have small corresponding magnitude values and therefore also large standard deviations. They will contribute little to many different theoretical phase curves (situation 2 in Fig. 3.5). Phase values inside the signal bandwidth, however, will dominate a few theoretical phase curves around the correct ones (situation 1 in Fig. 3.5). The summed probabilities for each curve then give a probability-density function from which we can pick the maxima as in the case of the slowness histograms. This leads to a stable estimate of the apparent slowness even if the phase curve is wrapped several times.

3.5 Iterative approach

The method described in this thesis requires an estimate of the number of waves present in the chosen analysis window. Normally, overestimation of this number has no influence on the separation of the waves actually present and the surplus output panels will contain noise or no energy at all in the noise-free case. Such an overestimation, however, requires

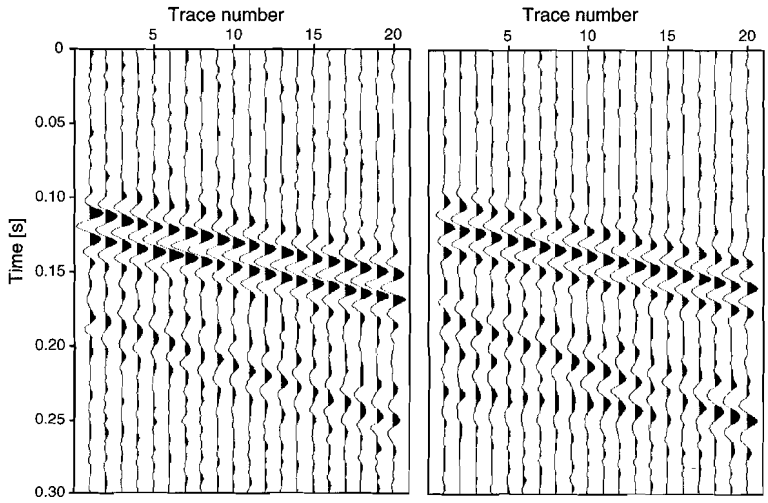

Figure 3.6: *Vertical (left) and inline-horizontal (right) component of the synthetic data used to illustrate the iterative approach. The four plane waves have significantly different amplitudes (see text). The characteristic parameters can be found in Table 3.1. Note: All panels in Figs. 3.6 and 3.7 have a common amplitude scaling.*

a large aperture and this is not feasible for the analysis of real data. In addition to parameter variations with offset for non-linear events the medium itself can also vary spatially. Large analysis windows will then yield averaged parameter estimates which is not desired. The number of traces can only be chosen small however if the number of waves present in the data is small (see Eq. 2.7). An iterative approach can provide a solution, if the data set contains waves that differ significantly in amplitude. First, the characteristic parameters of the dominant wave are estimated. Separation is then carried out using these estimates. Thereby it is attempted to maximise the energy of the dominant wave on its output panel while minimising the residual energy from the weaker arrivals. Next, the dominant wave is projected back onto the receiver components. Lastly, this energy is subtracted from the data. The procedure is then repeated with the residual data set until the original wavefield is totally decomposed. At a certain point it may be possible to decompose the residual data set in one step, if the remaining waves are of comparable amplitude.

The synthetic data set in Fig. 3.6 contains the same four plane waves as shown in Fig. 3.1 but their relative amplitudes were altered. The first S-wave has only half the amplitude of the P-wave, the second S-wave a quarter and the Rayleigh wave an eighth part. These amplitude ratios are chosen to illustrate the iterative approach rather than to represent values from a real earth model. The S/N (signal to noise) ratio on each trace is 10 and the trace separation is 5 m.

Applying the standard approach to this data it was only possible to extract the P-wave successfully. The two S-waves were recovered on some traces, but they were always

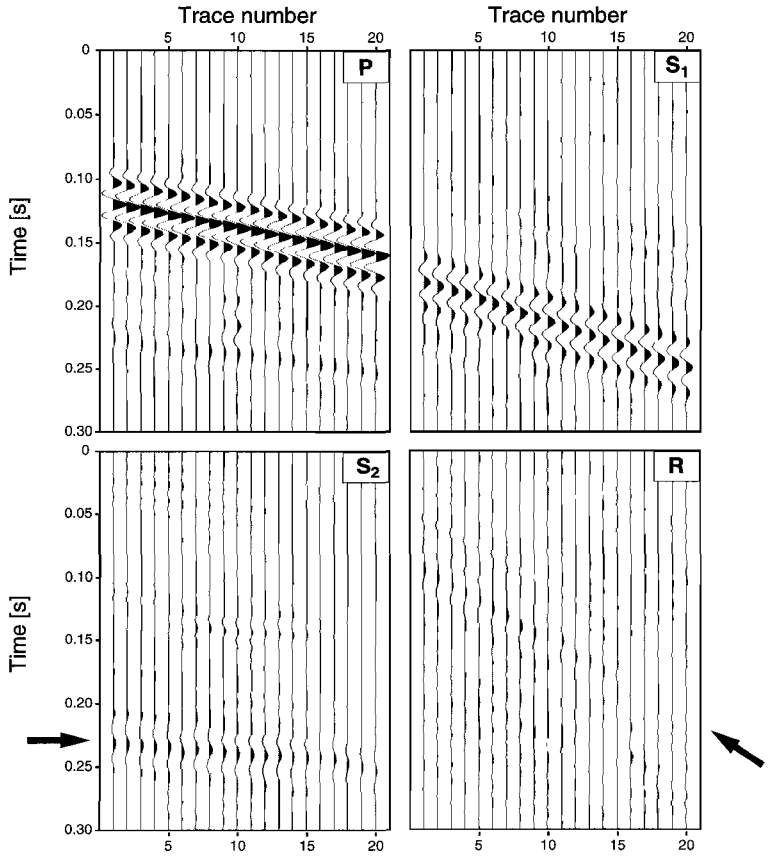

Figure 3.7: *Separated waves of Fig. 3.6 using the iterative approach: P-, first S-, Rayleigh and second S-wave (clockwise from the upper left). The arrows indicate the arrival time of the two weakest waves. Note: All panels in Figs. 3.6 and 3.7 have a common amplitude scaling.*

contaminated with additional energy from other waves. The Rayleigh-wave energy could not be identified.

Using the method in an iterative way improved the results dramatically, specifically for the waves with low amplitudes. In each iteration it was assumed, that there are only two waves present.

In the first iteration the P-wave was estimated (upper left plot in Fig. 3.7) and removed from the data. In the second iteration the first S-wave (upper right plot) was also estimated and removed. Finally, from the residual data both remaining waves, the second S-wave and the Rayleigh wave, were separated from each other, the Rayleigh wave suffering most from incorrect parameter estimation on the right side of the panel.

3.6 Noise

The method gives an accurate estimate of the characteristic parameters if no noise is present in the data. Cho and Spencer (1992) describe several methods to stabilise the estimation against random noise such as (1) adding a damping factor in the least squares solution (see Eq. 2.8) to suppress the noise outside the signal bandwidth, (2) averaging the transfer matrix over a certain frequency range or (3) using more traces in the analysis than formally required (see Eq. 2.7). Our experiences can be summarised as follows (using the same numbers as above):

(1) Damping factors for each receiver component are computed from an estimate of the average S/N ratio in the data window. Under the assumption that random noise on the two receiver components is uncorrelated and off-diagonal elements of the matrix $\boldsymbol{V}^n\boldsymbol{V}^{n\dagger}$ as well as all elements of the matrix $\boldsymbol{V}^{n+1}\boldsymbol{V}^{n\dagger}$ will contain zeroes outside the signal bandwidth, then the (small) diagonal values will completely dominate the least squares solution. Adding the damping factors to the diagonal elements of the matrix $\boldsymbol{V}^n\boldsymbol{V}^{n\dagger}$ leads to a decrease in the magnitudes of the eigenvalues and therefore restricts the frequency range for binning. Adding the same damping factors at frequencies inside the signal bandwidth has no effect on the parameter estimates.

(2) Since eigenvalue switching happens suddenly, explicit frequency averaging should be avoided unless there is no switching or it can be corrected for. We almost always use the statistical approach which effectively averages information for different frequencies depending on the bin size and the smoothness of the parameter curves.

(3) Increasing the length of the analysis window can stabilise the results significantly. If more than the minimally required number of receivers is used, the analysis window can be divided into sub-windows. The transfer matrix can be computed for each sub-window and finally all transfer matrices inside the analysis window are averaged. The smallest sub-window then contains the minimally required number of receivers. The maximum number of traces that can be used, depends of course on the scale of variation of the characteristic parameters.

Note, that coherent noise can be treated as an extra wave present in the data, because it can also be characterised by a certain apparent slowness and polarisation.

wave type	f_c [Hz]	T_{start} [ms]	p [s/km]	θ [°]	Amp
P-wave	50	100	0.214	50	1
S-wave	30	200	0.333	30	1

Table 3.2: *Modelling parameters for the data used in Figs 3.8, 3.9, 3.10, and 3.11. Trace separation was 10 m. For an explanation of the parameters see Table 3.1.*

We will illustrate approaches (1) and (3) in the following two sections by means of synthetic data. The model shown in Table 3.2 is used for all tests regarding noise and it should be noted that the noise is not scaled individually for each trace but for each component. The consequence is that traces with low signal energy have now also a lower S/N ratio compared to traces with high signal energy. Scaling the noise relative to the highest peak amplitude found for both components implies that the component with less signal energy has a higher noise-level too. This is equivalent to a component specific background-noise and is not used in this thesis. The relative error for each model is plotted in Figs. 3.8, 3.9, and 3.11 using a linear grey scale that is common for all three characteristic parameters of the S- as well as the P-wave. This global scaling stresses the difference in sensitivity of the different parameters to noise. Note, that the phase difference is allowed to be at most 360.° off, the polarisation angle at most 90.°, but the slowness at most 0.6 s/km.

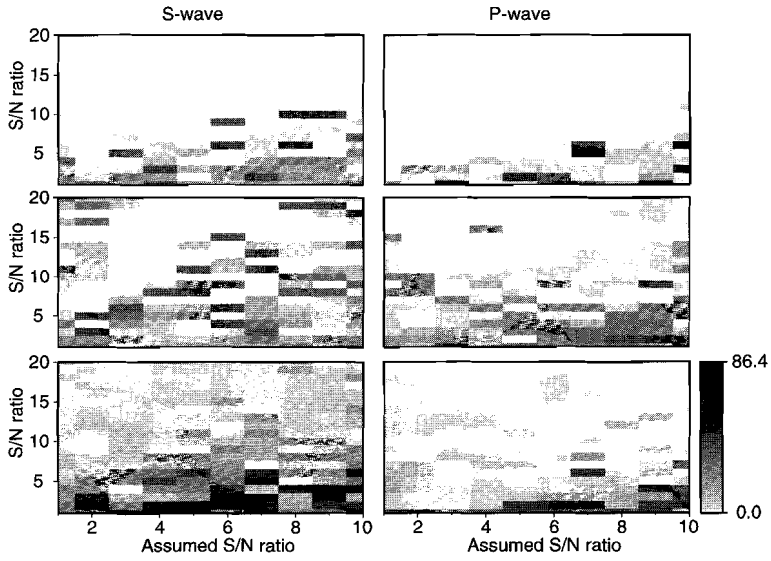

Figure 3.8: *Relative error in percentage for the parameter estimation from 3 data traces having varying S/N ratios. The data were analysed using assumed S/N ratios ranging from 1 to 10. Results for the phase difference (top), polarisation angle (middle), and slowness (bottom).*

3.6.1 Damping factor

The influence of damping on the parameter estimates is illustrated in Figs. 3.8, 3.9 and 3.10. Three data traces were computed using the modelling parameters listed in Table 3.2 and different amounts of noise were added. This resulted in 20 data sets having S/N ratios ranging from 1 to 20. The assumed S/N ratio for both components (see Eq. 2.16) is varied from 1 to 10 with increment 1 (Fig. 3.8) and from 10 to 100 with increment 10 (Fig. 3.9). The assumed S/N ratios have the same value for vertical and inline-horizontal component because noise was added to the synthetic data with the same S/N ratio for both components.
Parameter estimations for S/N ratios higher than 10 are all determined quite well independent of the assumed S/N ratio. For true S/N ratios smaller than 10 there is a slight trend to bigger errors, if the assumed S/N ratio increases. This trend is more obvious in the Fig. 3.9. The estimated parameters are generally more stable, if the assumed S/N ratio is kept small.

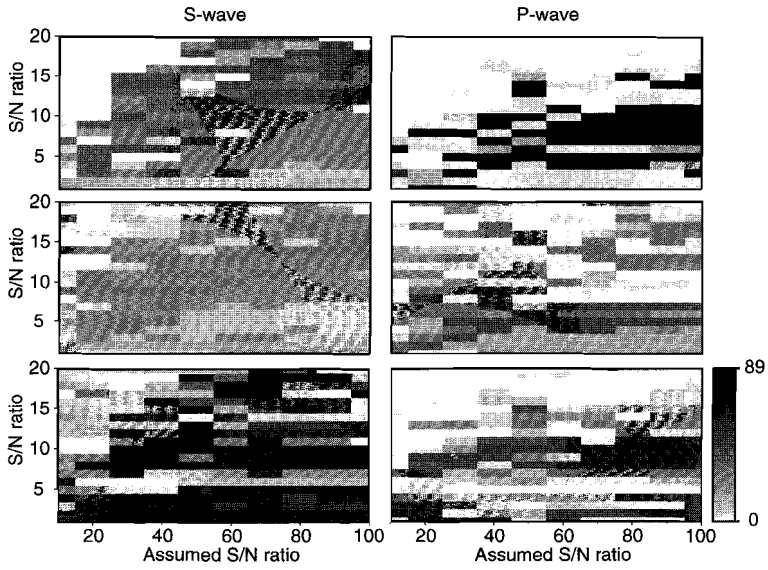

Figure 3.9: *Same analysis as shown in Fig. 3.8 but the assumed S/N ratio is varied from 10 to 100 this time. Results for the phase difference (top), polarisation angle (middle), and slowness (bottom).*

Surprisingly, there are sometimes excellent estimates at low S/N ratios and high assumed S/N ratios. In Fig. 3.9 at a S/N of 6, for example, there are good estimates for all assumed S/N ratios from 20 to 100 for the slowness of both waves. In order to examine this in more detail a data set consisting of 14 traces was analysed by a moving window of length 3 traces. This resulted in 12 individual parameter estimations from which the mean and standard deviation were computed. The S/N ratio was varied from 1 to 20 and

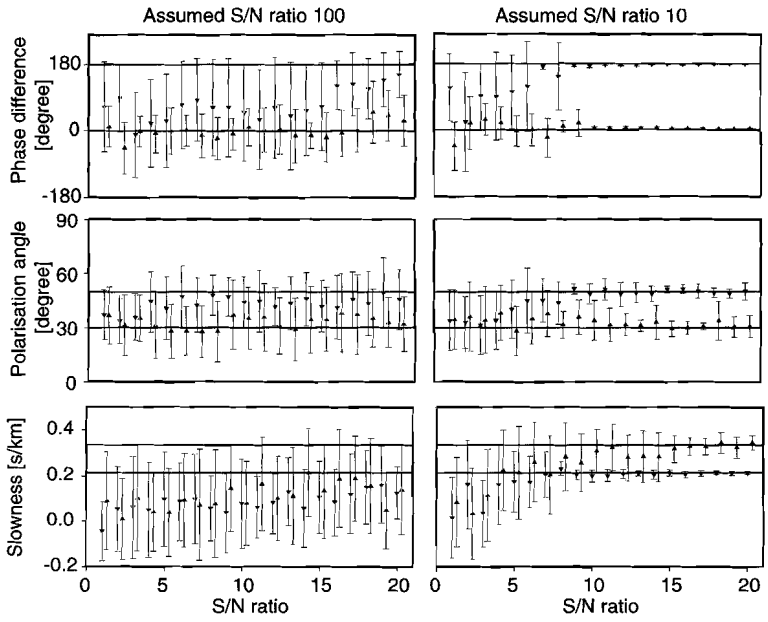

Figure 3.10: *Based on the analysis of 12 moving windows the mean and standard deviation for the characteristic parameters was computed for a varying S/N ratio. On the left-hand side the assumed S/N ratio was 100, on the right-hand side it was 10. Results for the phase difference (top), polarisation angle (middle), and slowness (bottom). The triangle represent the mean estimates for the S-wave and the inverted triangles for the P-wave. The true values are indicated by the solid lines. One standard deviation is indicated by the bar.*

the assumed S/N ratio for both components was first set to 100 (results are shown on the left-hand side of Fig. 3.10). The analysis was repeated using an assumed S/N ratio of 10 (results are shown on the right-hand side of Fig. 3.10). The standard deviation decreases rapidly for increasing S/N ratio if the assumed S/N ratio is 10, but there is hardly any decrease in the left-hand plots of Fig. 3.10. The mean values for both realizations tend to the true values for higher S/N ratios. The slowness is underestimated on average for less damping. The bias toward smaller values results from the search direction during picking of the maxima from the histograms: the parameter space is searched from low to high values. The length of the bars (one standard deviation) indicates quite clearly how broad the range of estimated parameters can be for low S/N ratios and little damping which now explains why there can be (by chance) quite a good estimate for low S/N ratios in Fig. 3.9.

3.6.2 Number of receivers

Subsequently, the influence of the number of receivers on the parameter estimation was tested. The assumed S/N ratio was kept at the high value of 100. The results are displayed in Fig. 3.11. They show that for small S/N ratios (smaller than 5) there is hardly any increase in the robustness of the estimate if the number of traces is increased. For S/N ratios bigger than 5 the number of receivers show a clear influence on the parameter estimates. The maximum number of traces that can be used, however, depends also on the scale of variation of the characteristic parameters. Using more traces will lead to an averaged estimate decreasing the lateral resolution.

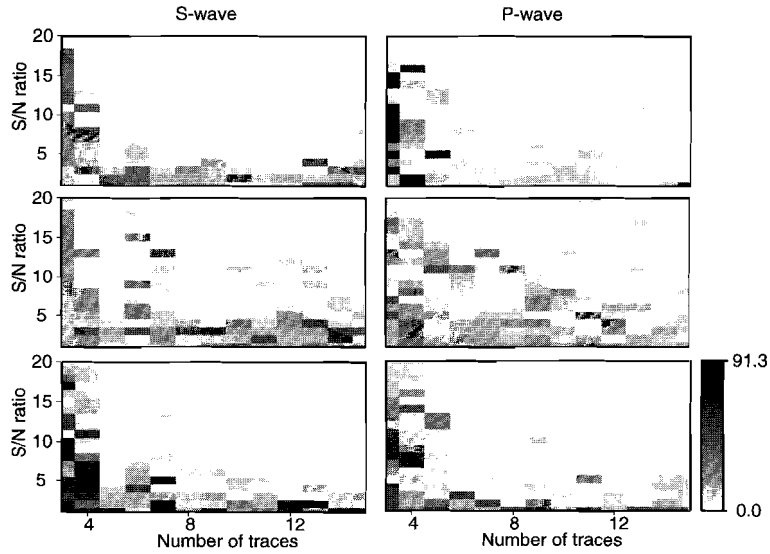

Figure 3.11: *Effect of the increase in the number of traces inside the analysis window on the quality of the parameter estimates. The assumed S/N ratio was kept at 100. Upper figure: Phase difference. Middle figure: Polarisation angle. Lower figure: Slowness.*

3.7 Sensitivity

A variety of noise-free data sets were created to test the sensitivity of the method to time- and frequency-overlap of the waves. The parameters for the starting data set are listed in Table 3.3. Successively, the starting time of the main peak of the P-wavelet was increased by 10 ms and its central frequency lowered by 5 Hz. Each time, the characteristic parameters were estimated and compared with the true ones. The analysis was based on 3 noise-free traces only, trace to trace distance was 10 m. The relative errors (in percentage) are plotted in Fig. 3.12 for the phase difference, polarisation angle and slowness (from top to bottom). A global grey scaling has been used for plotting. The accuracy in estimating

wave type	f_c [Hz]	T_{start} [ms]	p [s/km]	θ [°]	Amp
P-wave	85	100	0.214	50	1
S-wave	30	200	0.333	30	1

Table 3.3: *Modelling parameters for starting data set of time- and frequency-overlap sensitivity analysis. For an explanation of the parameters see Table 3.1.*

the parameters was 0.25° for the phase difference, 0.125° for the polarisation angle and 0.0005 s/km for the slowness, which explains, why the biggest relative error is found for the phase difference. There is no indication for a general trend that leads to an increase in error for increasing frequency- or time-overlap between the waves.

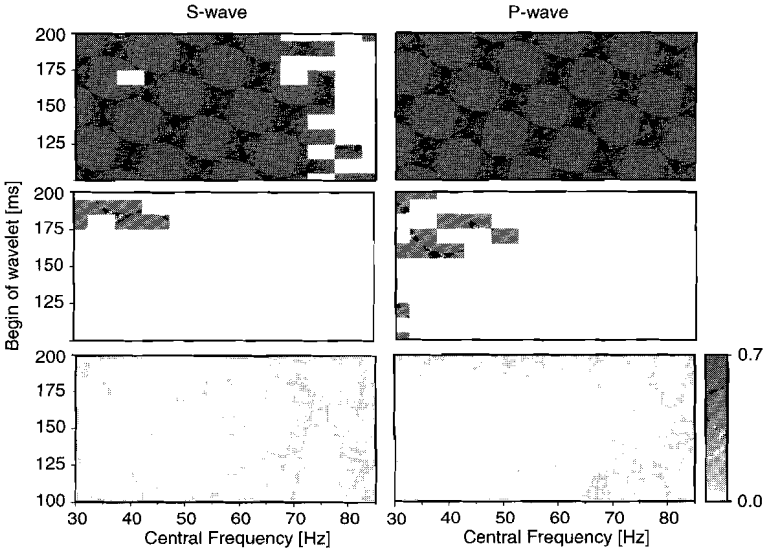

Figure 3.12: *While S-wave values were kept fixed, the start of the P-wave and its central frequency were varied. At 200 ms begin time and a central frequency of 30 Hz, there is complete overlap in time and frequency for the two waves. The percentage in error between true and estimated values is plotted. Results for the phase difference (top), polarisation angle (middle), and slowness (bottom).*

Another test was performed, this time the polarisation angle and amplitude of the P-wave were varied. The starting parameters are shown in Table 3.4. Both waves have the same central frequency. The amplitude was successively lowered by 0.1 while the polarisation angle was decreased by 5° for each new model. The estimates were based on the analysis of 3 neighbouring noise-free traces separated by 10 m. The relative errors are plotted in Fig. 3.13 using a global grey scaling. First, the analysis was carried out using the

wave type	f_c [Hz]	T_{start} [ms]	p [s/km]	θ [°]	Amp
P-wave	30	200	0.029	85	1
S-wave	30	200	0.333	30	1

Table 3.4: *Modelling parameters for starting data set of polarisation-overlap and amplitude ratio sensitivity analysis. For an explanation of the parameters see Table 3.1.*

estimated slowness values for tracing back the other two characteristic parameters. For decreasing polarisation angle of the P-wave, however, the slowness difference between the two waves also decreases. The choice for the minimum distance between successive peaks in the slowness histogram prescribes the final slowness resolution. Therefore, the exclusion distance should have been lowered in anticipation to the decreasing difference in slowness between the two waves. For this data a different approach was chosen. We use the phase difference for back-tracing. This parameter stays constant for all models and gives improved results compared to using the slowness: a drop in the maximum error of 50 % was achieved (the exclusion distance between successive peaks was set to 0.05 s/km).

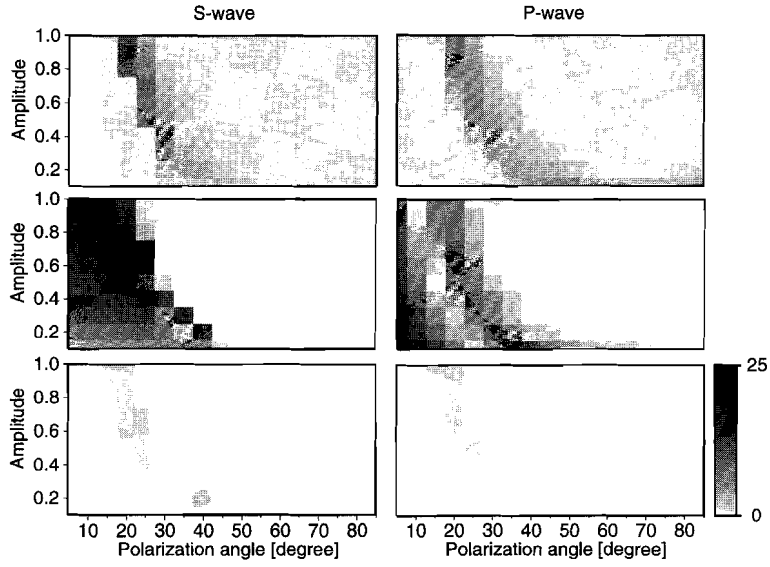

Figure 3.13: *While S-wave values were kept fixed, the polarisation angle for the P-wave and its amplitude were varied. Both waves have the same central frequency. The percentage in error between true and estimated values is plotted. Results for the phase difference (top), polarisation angle (middle), and slowness (bottom).*

Fig. 3.13 indicates that neither the amplitude ratio of S- and P-wave nor the change in

polarisation angle have an influence on the quality of the slowness estimates. The phase difference shows a maximum in error around equal polarisation angle for the two waves. The error in the polarisation angle generally increases for decreasing P-wave polarisation angle. The estimated values are closer to that of the S-wave, if the P-wave amplitude is small and closer to that of the P-wave, if its amplitude is comparable to that of the S-wave. The general misfit is due to an insufficient move-out difference between the two waves. The transfer matrix has in this case only one significant eigenvalue. Increasing the move-out difference can solve the problem. If, for example, two extra traces are added to the analysis of the model with P-wave polarisation angle of 20.° and P-wave amplitude of 0.4 the correct values for both polarisation angles are estimated, the estimates of the slowness are improved slightly (they were already quite good) and the estimates for the phase difference are improved, but not yet optimum. Adding two more traces improves also the latter ones. Similar results can be obtained by lowering the S-wave velocity or changing the central frequency of one wave. Fig. 3.14 shows the results that were obtained by changing the central frequency of the P-wave to 50 Hz.

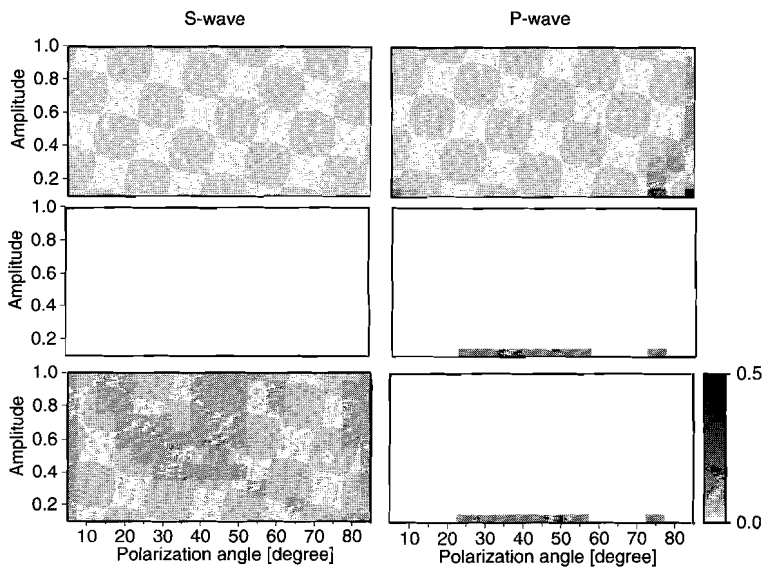

Figure 3.14: *While S-wave values were kept fixed, the polarisation angle for the P-wave and its amplitude were varied. The central frequency of the P-wave is changed to 50 Hz in comparison with Fig. 3.13. Results for the phase difference (top), polarisation angle (middle), and slowness (bottom).*

wave type	f_c [Hz]	T_{start} [ms]	Amp	p [s/km]	θ [°]
Rayleigh wave	40	50	2	0.5167 - 0.8628	66
P-wave	50	100	1	0.214	50

Table 3.5: *Modelling parameters for synthetic data of Fig. 3.15. For an explanation of the parameters see Table 3.1.*

3.8 Dispersive waves

As mentioned earlier, the method allows for the analysis of dispersive waves. The transfer matrix is estimated for each frequency and so is the horizontal slowness (horizontal phase velocity). The data set shown in Fig. 3.15 (for modelling parameters see Table 3.5) consists of two waves, a dispersive Rayleigh wave and a non-dispersive P-wave. The S/N ratio is 8 for both the vertical and the inline-horizontal component and the trace separation is 10 m. Additionally, the amplitude of the Rayleigh wave was set to twice the value of the P-wave prior to projection onto the receiver components. The dispersion function was chosen to be slightly exponential (see upper dotted line in Fig. 3.16).

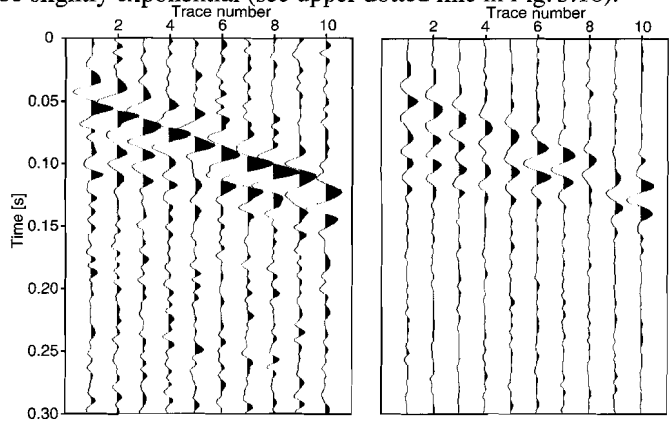

Figure 3.15: *Vertical (left) and inline-horizontal (right)component of the synthetic data set used to illustrate the analysis of dispersive waves. The S/N ratio on each panel is 8. Note: All panels in Figs. 3.15, 3.18 and 3.19 have a common amplitude scaling.*

Seven traces were used in the analysis and the slowness estimated from the first 7 traces of Fig. 3.15 is shown in Fig. 3.16. The estimated values (dots) show scattering due to the random noise added to the data. The estimated slowness values cannot be used directly for separation since they first have to be ordered into two groups according to the two waves present in the data. Due to noise, the slowness values estimated at frequencies away from the central frequency of the wavelet are not reliable. Therefore, the histogram analysis for frequency independent slowness curves was adapted. The data points were sorted into bins around straight lines with varying slopes. The result of the analysis is shown

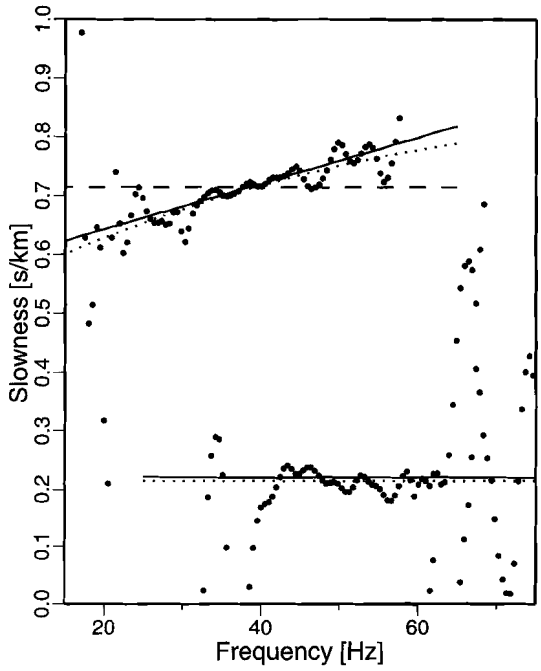

Figure 3.16: *Comparison between estimated (dots), fitted (solid lines) and true (dotted lines) slowness for the first 7 traces. The fitted line for the dispersive wave is 0.565 s/km + 0.0039 s/km/Hz and for the non-dispersive wave 0.22 s/km. Assuming no dispersion to be present the fitted slowness is indicated with the dashed line (0.715 s/km). For the P-wave this fit equals the one obtained under the assumption that dispersion is present.*

in Fig. 3.17. The wedge-shaped appearance comes from the bin width that allows points to be assigned to different fitting lines. The wedge belonging to the dispersive wave has curved boundaries because the dispersion function was slightly exponential (this is easier to see for data without noise). The second maximum in the figure which is not connected to the dispersive wave is roughly half in amplitude and it belongs to the non-dispersive P-wave. In order to find this maximum all slowness points in Fig. 3.16 falling inside the bin representing the first maximum were removed from the data set and the analysis repeated. Due to scatter of the data points the bin width had to be increased from 0.005 s/km (for the analysis assuming no dispersion) to 0.015 s/km. The lower the S/N ratio and the greater the deviation of the actual dispersion curve from a straight line, the coarser the bin width has to be chosen to locate other maxima. A different approach similar to the one for the histograms of non-dispersive data could also be adopted, hereby defining a minimum slowness as well as a minimum slope distance between accepted maxima.

Functions fitted for each moving window were used for separating the two waves, which were then subtracted from the original waves. The results are shown on the left-hand

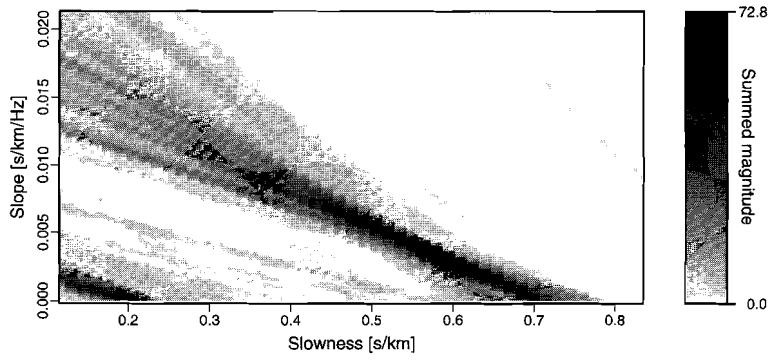

Figure 3.17: *Histogram computed from the data points shown in Fig. 3.16.*

sides of Figs. 3.18 (Rayleigh wave) and 3.19 (P-wave). The wavefield separation was then repeated with a frequency independent slowness function as estimated during normal histogram analysis. The results are shown on the right-hand sides of Figs. 3.18 (Rayleigh wave) and 3.19 (P-wave). There is hardly any difference between the left- and right-hand sides, but the mean energy of the latter is higher: 12 % for the Rayleigh wave and 9 % for the P-wave. Note that for the noise-free case the discrepancy between the original and separated data using the frequency-independent slowness curve is bigger compared to the dispersive approach. A perfect match, however, can only be achieved by using the correct exponential dispersion curve.

Depending on the dispersion curve and the S/N ratio it might not be necessary or even useful, respectively, to obtain a frequency dependent slowness curve for wavefield separation. The estimated dispersion relation, however, could be directly used for the inversion of the S-wave velocity structure in the sub-surface as shown for example by Gabriels et al. (1987).

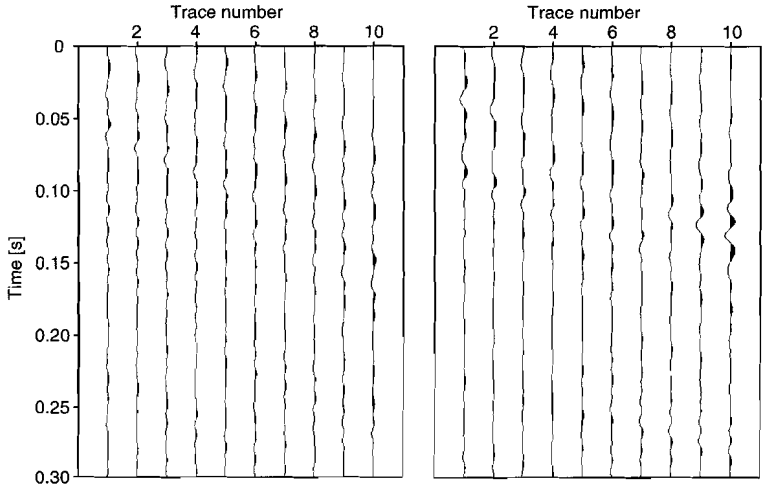

Figure 3.18: *Difference between original dispersive and separated Rayleigh wave. The results on the left-hand and right-hand side were achieved using a fit to the dispersion curve and a frequency independent slowness estimate, respectively. Note: All panels in Figs. 3.15, 3.18 and 3.19 have a common amplitude scaling.*

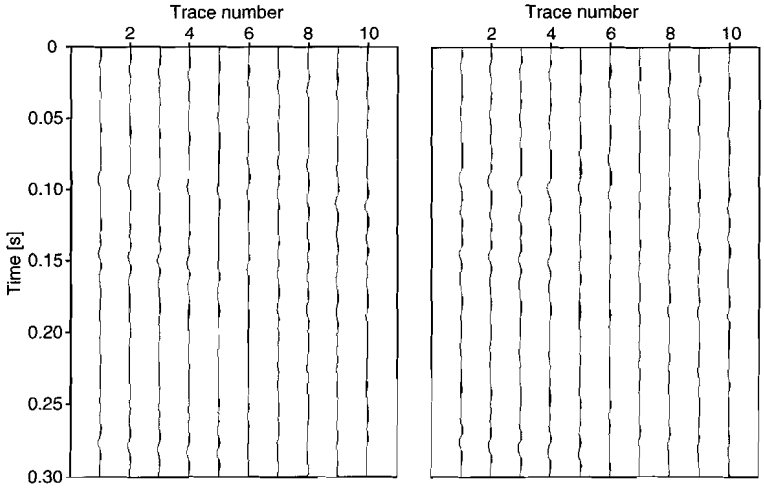

Figure 3.19: *Difference between original and separated P-wave. For a description of left-hand and right-hand side of figure, see Fig. 3.18. Note: All panels in Figs. 3.15, 3.18 and 3.19 have a common amplitude scaling.*

Chapter 4

IMPLICATIONS FOR SURFACE SEISMIC DATA

4.1 Introduction

It has been shown in Chapter 3 that application of the method to plane-wave data involves a number of practical issues. These stem from methodological as well as data dependent problems. The necessity to deal with random noise in the data, the switching and sharing of eigenvalues, aliased waves, dispersive waves, and waves which differ in amplitude has finally led to modifications and new analysis tools. The data used so far has still complied with the plane-wave assumption. Real data, however, contain reflections and diffractions having non-linear move-out, so they will satisfy this assumption only approximately. This influence of non-linear and non-continuous events on the parameter estimates will be illustrated in the following chapter using a noise-free data set modelled with an elastic 2D finite difference code. Application of the method to real data involves some more issues which will be discussed below.

Lateral variations in the thickness of the poorly compacted near-surface layer and changes in wave velocity lead to additional, often irregular, time shifts for one event on neighbouring receivers (statics). P-wave statics can be of the order of 50 ms e.g. for the western part of the Netherlands. S-waves are not affected by pore fluids and their velocity is therefore not influenced in a similar manner as P-waves in the near-surface, causing the S-wave statics to be 2 to 10 times bigger than the P-wave statics (Tatham and McCormack (1991)). We show that the estimate of the phase difference between the components is hardly affected by random static shifts applied to plane-wave synthetic data, while the quality of the slowness and polarisation angle estimates depend on the magnitude of the shift.

Another problem with real data is coupling. A trivial requirement is that all geophones should be planted levelled. For the vertical geophones the decrease in sensitivity is proportional to the cosine of the tilt angle and can in principle be neglected. For the horizontal geophone the ability to suppress other than horizontal motion deteriorates rapidly with increasing tilt angle (Brouwer and Helbig (1998)). The general effect of bad coupling on the vertical component is less than on the horizontal component, since the latter may show 'rocking' if the base of the geophones is not pressed firmly to the ground (Krohn (1984)). The overall effect is a decrease of the coupling resonant frequency, which is the natural frequency of the geophone-ground system. For frequencies much lower than this frequency, the geophone accurately follows the ground motion, but at higher frequencies the amplitude and phase are altered by the coupling. Trace balancing the data before analysis helps in stabilising the estimates as will be shown using synthetic data, provided each receiver component is affected by the coupling in the same way. We also conducted a field test with three-component orthogonal geophones to study the effect of

changes in coupling on the receiver components. For multi-component seismic profiling three-component geophones should be preferred to three single component geophones since the latter can be coupled differently. This will have an additional influence on the measurement of the polarisation state of the waves.
For land seismic surveys, receivers are planted at the free surface and the measured particle movement is influenced by this traction-free surface. This movement depends on the type of the up-going wave, its amplitude, angle of incidence, and the Poisson's ratio in the uppermost part of the wave's travel-path. The thickness of this uppermost zone influencing the recordings depends on the seismic wavelength. The wavefield separation method is only sensitive to the coupled system of up- and down-going waves and will therefore estimate apparent values not only for the horizontal slowness, but also for the polarisation angle. S-waves encounter an additional phase change for supercritical angles of incidence and therefore an apparent value for the phase difference is obtained too. If the parameters do not change rapidly, the method is able to separate coupled systems from each other. We illustrate the theoretical effect of the free surface on the recorded particle motion, show the estimated values from an analysis of synthetic noise free data, and indicate how we can invert for the parameters needed for the decomposition of the coupled wavefield into up- and down-going waves.

4.2 Statics

Lateral variations in the thickness of the uppermost layer together with velocity variations can lead to additional arrival time differences for a wave at adjacent receivers, called statics. The influence of statics on the apparent slowness is expected to be bigger than on the polarisation parameters. We therefore performed the following test. The difference in P- and S-wave statics was simulated by first adding the random static shifts to each wave separately (for modelling parameters see Table 4.1). For simplicity, the time shifts were for both waves in the same direction assuming that although the order of magnitude of the actual shift is different, both waves are either delayed or advanced by the lateral change in parameters. Then both waves were summed up and random noise (S/N ratio of 10) was added. This noise was computed only once for the original panel without statics (see Fig. 4.1). The statics for the P-wave were varied from 0 to +/-10 samples (the sampling rate was 1 ms), while for the S-wave they were varied from 0 to +/-20 samples. As an example, Fig. 4.2 shows the panel with the biggest statics, +/-10 samples for the P-wave and +/-20 samples for the S-wave. We varied the magnitude in steps of 2 samples and chose the S-wave statics to be at least twice as big as the P-wave statics. Including the data without statics, 36 different statics models were thus constructed. The labels on the vertical axis of Fig. 4.3 indicate the amount of P- wave statics, e.g. label 2 indicates 2 ms P-wave statics and 4 to 20 ms of S-wave statics. The relative shift between adjacent traces remained the same, while the magnitude of each individual shift was scaled according to the maximum shift allowed. It must be noted that since the shifts were randomly distributed for the 15 traces and since the minimum possible shift is one sample, some traces were not shifted at all if the maximum shift was small. The errors in the estimated

wave type	f_c [Hz]	$T_{start}[ms]$	p [s/km]	θ [°]	Amp
P-wave	50	150	0.214	50	1
S-wave	40	150	0.417	30	1

Table 4.1: *Modelling parameters for the original plane-wave data set prior to applying static shifts to the traces. Trace separation was 10 m. For an explanation of the parameters see Table 3.1.*

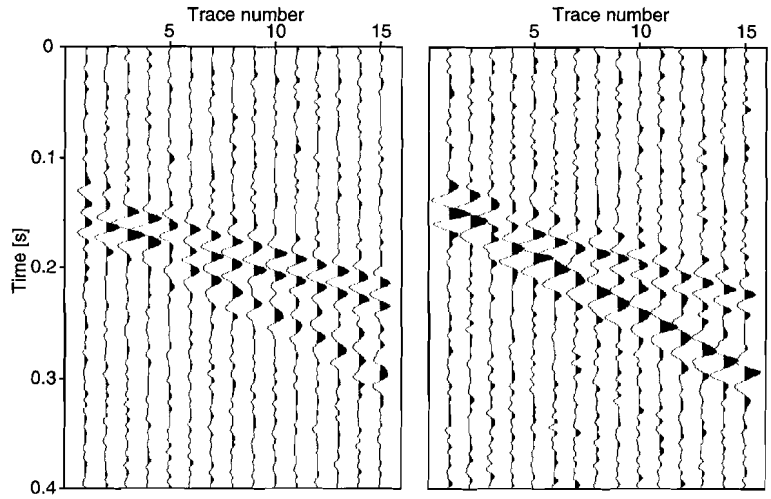

Figure 4.1: *Vertical (left) and inline-horizontal (right) component without statics. The S/N ratio is 10.*

parameters (from an analysis of 5 traces) are shown in Fig. 4.3.

The polarisation angle of the P-wave is generally well estimated (see middle right figure in Fig. 4.3), while the estimation of the S-wave is only successful up to +/-10 samples shift. Then the estimated angle is suddenly at least 30 degrees off. Is is shown in the upper figures of Fig. 4.3 that the phase difference is the most robust parameter as expected. The big error results from the incorrect determination of the sign of the phase difference. The error in slowness estimation is shown in the lower figure of Fig. 4.3. As with the polarisation angle, this parameter is more robust for the P-wave due to smaller statics and values are estimated well as long as the statics do not exceed +/-10 samples. Surprisingly, there are models where the S-wave slowness is still estimated well despite large statics, e.g. at trace 4 for the highest static shifts applied. These good estimates are obtained by chance as already demonstrated in Fig. 3.10.

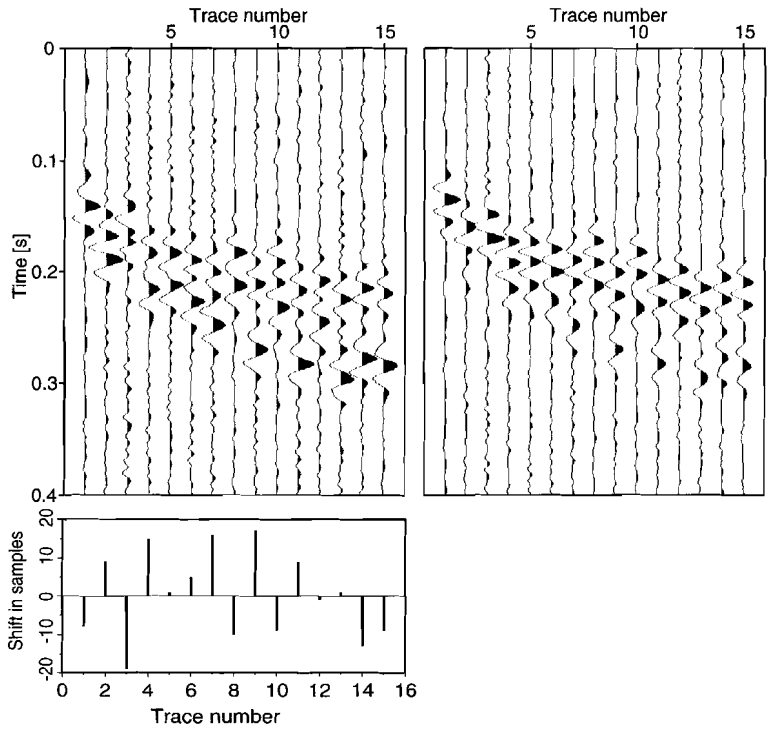

Figure 4.2: *Upper panels: Vertical (left) and inline-horizontal (right) component with statics: +/-10 samples for the P-wave and +/-20 samples for the S-wave. Lower panel: actual shift of samples for each individual trace for this model.*

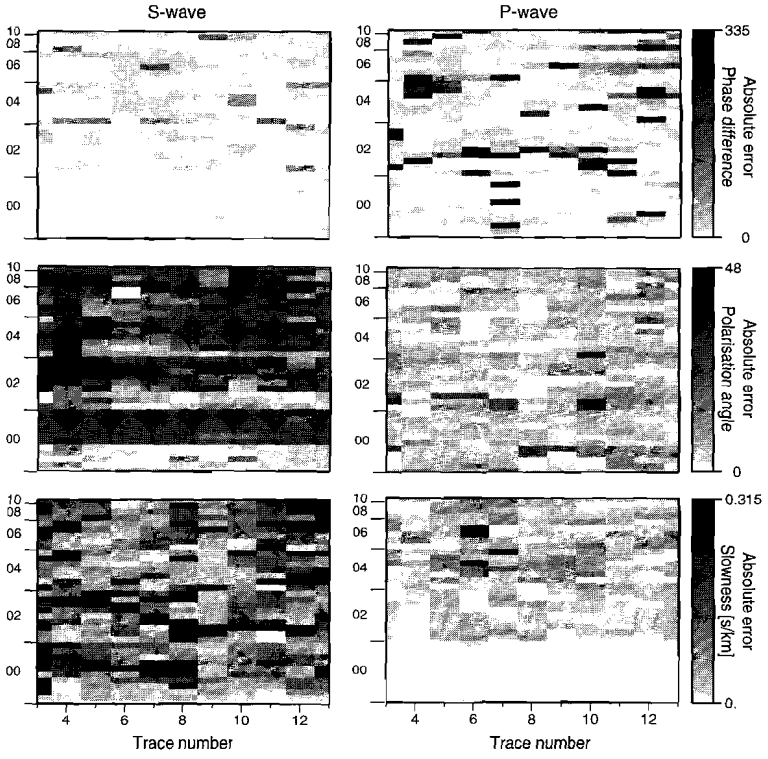

Figure 4.3: *Absolute error between estimated and true parameters for differing amounts of static shifts in the data shown in Fig. 4.3. The vertical axis is divided in blocks. Each block corresponds to a constant static shift for the P-wave (indicated by the label) and a variation in static shift for the S-wave from twice the P-wave statics to the maximum shift of 20 samples.*

4.3 Coupling effects

Recorded amplitudes change from one receiver to the next due to attenuation (geometrical spreading and absorption). The attenuation can be deduced from the magnitudes of the eigenvalues that give a direct indication for energy loss if their value falls below 1. The decrease in amplitude due to absorption is exponential with distance:

$$U_i^{n+1} = U_i^n e^{-\eta\Delta},$$

with η being the absorption coefficient. Cho and Spencer (1992) relate this coefficient directly to the magnitude of the eigenvalues $|\lambda|$:

$$\eta = -\frac{1}{\Delta}\ln(|\lambda|).$$

The magnitude of the eigenvalues then represents simply the amplitude ratio between adjacent receivers. The data comply with the plane-wave assumption if this ratio is constant and close to the value 1 inside the analysis window.
The ratio can change rapidly if the coupling of the receivers changes due to improper planting. First we illustrate how the parameter estimates are influenced by changes in coupling by means of synthetic data. Then we show results from a field coupling test.

4.3.1 The effect of coupling on the parameter estimation

The influence of coupling on parameter estimation was investigated by means of a scaled synthetic plane-wave data set. The parameters are listed in Table 4.2. Each trace was scaled by an arbitrarily chosen number between 0.1 and 2. The scaling factors applied to the vertical and inline-horizontal component were the same. The data are shown in Fig. 4.4 together with the actual scaling factors. Trace separation was 5 m and no noise was added to the data. The traces were then analysed using 3 traces in the moving window.

wave type	f_c [Hz]	T_{start} [ms]	p [s/km]	θ [°]
P-wave	40	200	0.51	40
S-wave	30	100	1.88	70

Table 4.2: *Modelling parameters for synthetic data of Fig. 4.4. For an explanation of the parameters see Table 3.1.*

Fig. 4.5 shows a comparison between the true (solid lines) and estimated parameters. First, estimation was carried out on the data shown in Fig. 4.4 without applying trace balancing prior to estimation. The results are based on the original estimated values (no back-tracing used). The parameter values (triangles) show scatter for most of the analysis windows, but especially for those where a low amplitude trace is located in the middle of the window (traces 4,7,9,12,16,18). The eigenanalysis of the transfer matrix then yields

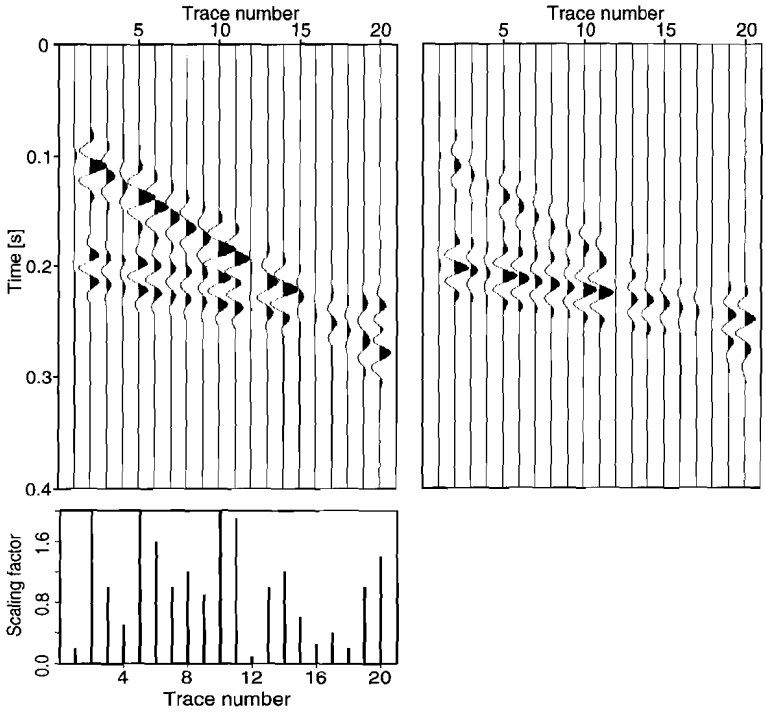

Figure 4.4: *Vertical (left-hand side) and inline-horizontal (right-hand side) component of scaled data. For model parameters see Table 4.2. The panels have a common amplitude scaling for plotting. The lower panel shows the scaling factors applied to each trace.*

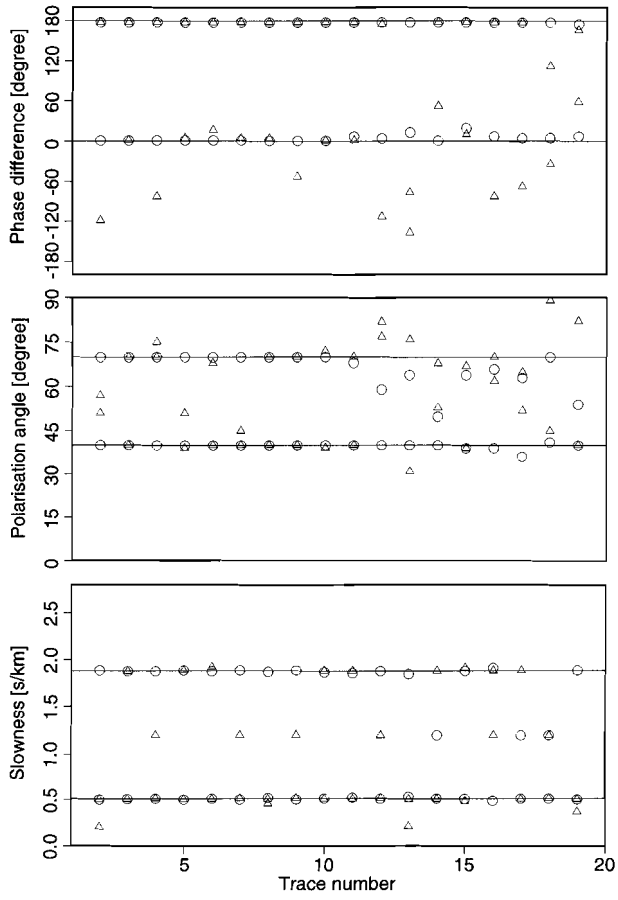

Figure 4.5: *Comparison between true parameter values (solid lines), estimated values using no trace balancing (triangles) and estimated values using trace balancing (circles). The data are shown in Fig. 4.4.*

only one significant eigenvalue for most or all of the frequencies which in this case belongs mainly to the P-wave. Generally, the slowness tends to a value which is the average between the two true values. If trace balancing is applied prior to estimation (circles in Fig. 4.5) better estimates are achieved for the phase difference. The polarisation angle shows better results for traces where there is not yet interference between the two waves. From trace 11 on, the scatter is as big as without trace balancing. The slowness is estimated better compared to the previous results, only traces 14, 17 and 19 give averaged results for the S-wave, probably due to the interference. In general, trace balancing helps in stabilising the results and should always be used.

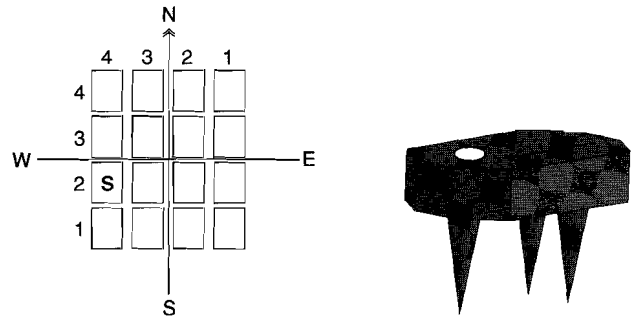

Figure 4.6: *Field lay-out (left-hand side) for the coupling test of the three-component orthogonal geophones (right-hand side). The geophone (denoted by 'S') in the 4th column, second row, was placed on a stone and was the worst coupled geophone in the whole lay-out. The spike length is ≈ 8 cm. Distance between the spikes along major axis: 7cm, along minor axis: 5 cm.*

4.3.2 The effect of coupling on field data

In order to test the effect of coupling on the different geophone components a field test was carried out. The survey area is located on the campus of Utrecht University. Due to building activities a fairly homogeneous sand layer is situated on top of the original ground and the area has a uniform surface without vegetation. 16 orthogonal 3C-geophones were laid out in the pattern shown in Fig. 4.6 (left-hand side).

column #1	pushed firmly into ground, base rests on surface
column #2	base ≈ 0.5 cm above the surface
column #3	tilted to the east (maximum angle of ≈ 10 °)
column #4	placed well above ground (≈ 4 cm above the surface)

Table 4.3: *The 4 different coupling scenarios were realised resulting in the described columns and each column had 4 geophones planted as similarly as possible.*

The 16 geophones were divided into groups of 4 which were then planted as listed in Table 4.3. The second column geophones were planted in a way that is possible during acquisition if the geophones are laid out in a hurry. In the field one would probably allow for a bigger distance between geophone base and ground rather than planting the geophone as lop-sided as in column # 3. The geophones also have a water-level on top of the casing which helps in planting the geophones levelled (see Fig. 4.6 for a sketch of the geophone). Note that all other geophones were planted horizontally. In the field there is normally a trade off between an absolutely horizontally planted geophone and one that has its base pushed firmly to the ground due to the surface being grown over. In the fourth column the geophones were pushed only as far into the ground that they

maintained a horizontal position. The geophone in the second row (denoted by 'S') was the worst coupled, because it rested on a stone.
The distance between successive columns was approximately 20 cm and between successive rows approximately 17 cm. The geophones were planted as closely as possible without touching each other or being touched by their cables. The source was a weight drop of 24 kg dropped from a small height by hand. Four shot positions were chosen at each side of the rectangle, each 5 m away from the centre of the side.
Figs. 4.7 and 4.8 show a comparison between the differently coupled geophones. The shot was located south of the geophone rectangle, so the geophones in the second row (Fig. 4.7) show slightly higher amplitudes due to less attenuation than the geophones in the third row. The eye-catching feature is the mono-frequent ringing of the crossline-horizontal component in the second row (thin solid line). The ringing starts right after the arrival of the first energy. This is the geophone which was planted right on the stone and therefore has the worst coupling of all. In general, both horizontal components show ringing which can be seen as resonance peaks in the spectra. The recordings on the vertical component are nearly the same for all geophones. The tilted geophone (dotted line) does not behave completely different when compared to the two better coupled geophones.
The particle motion recorded by the four differently coupled geophones is shown in Fig. 4.9. Only the data from the second row are shown. In general, particle motion is very similar for the geophones in the first three columns, while the worst coupled geophone in column #4 has a different pattern.
The shot position west of the array was analysed to investigate the effect of tilting on the recorded signal. This time, column #4 was omitted in the analysis. Fig. 4.10 shows traces (left-hand side) and spectra (right-hand side) for row #1. The two solid lines are very similar but for the a phase-lag due to a bigger shot-to-receiver distance for the geophone in the first column compared to that in the second column. The tilted geophone should have the highest amplitude because it is situated closest to the source. This is true for the vertical component, but the horizontal components, especially the crossline-horizontal component, which for this configuration is in fact the inline-horizontal one, the amplitude is lower.
From this field test it can be concluded that the three-component geophones we use do not have to be pushed completely into the ground to ensure proper recording of the wavefield. They should, however, be planted as up-right as possible to ensure proper recording of the polarisation state of the waves.

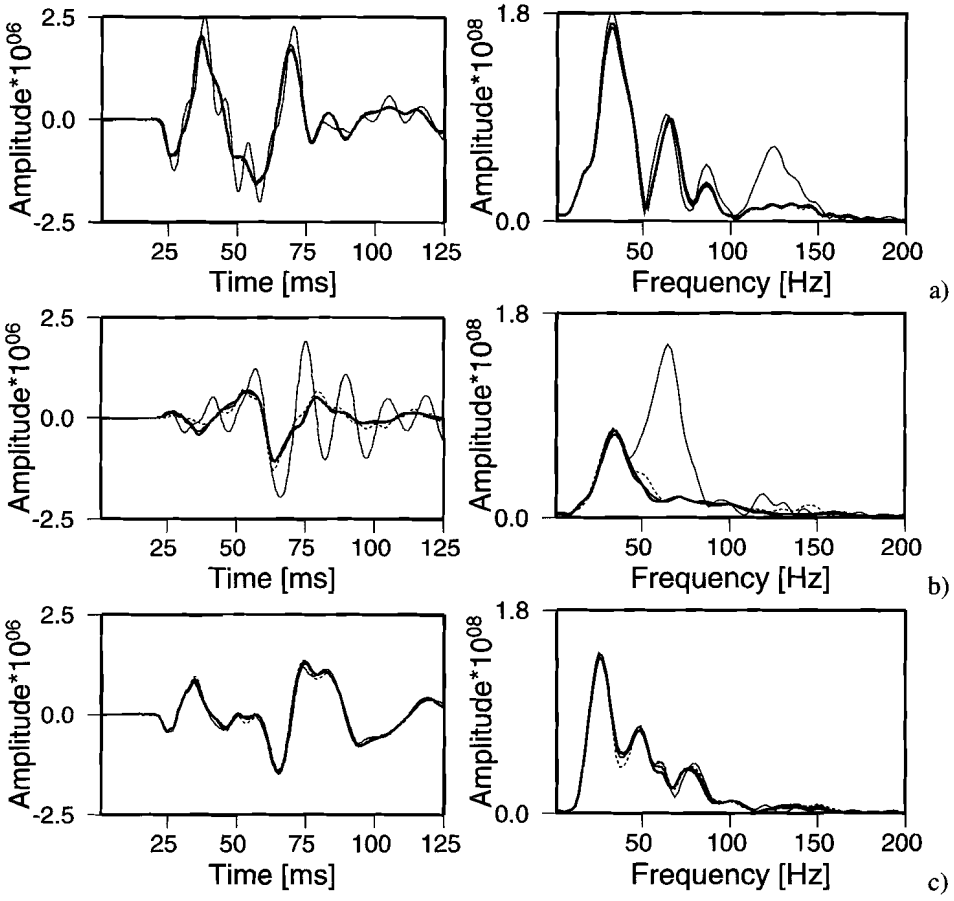

Figure 4.7: *Comparison of four differently coupled geophones in row #2, shot located south of geophone rectangle. Thick solid line: well-coupled geophone; middle solid line: geophone 0.5 cm above ground; thin solid line: geophone well above ground; dotted line: tilted geophone. The left column shows the traces, the right one the spectra. a): inline-horizontal component; b): cross-line horizontal component c): vertical component.*

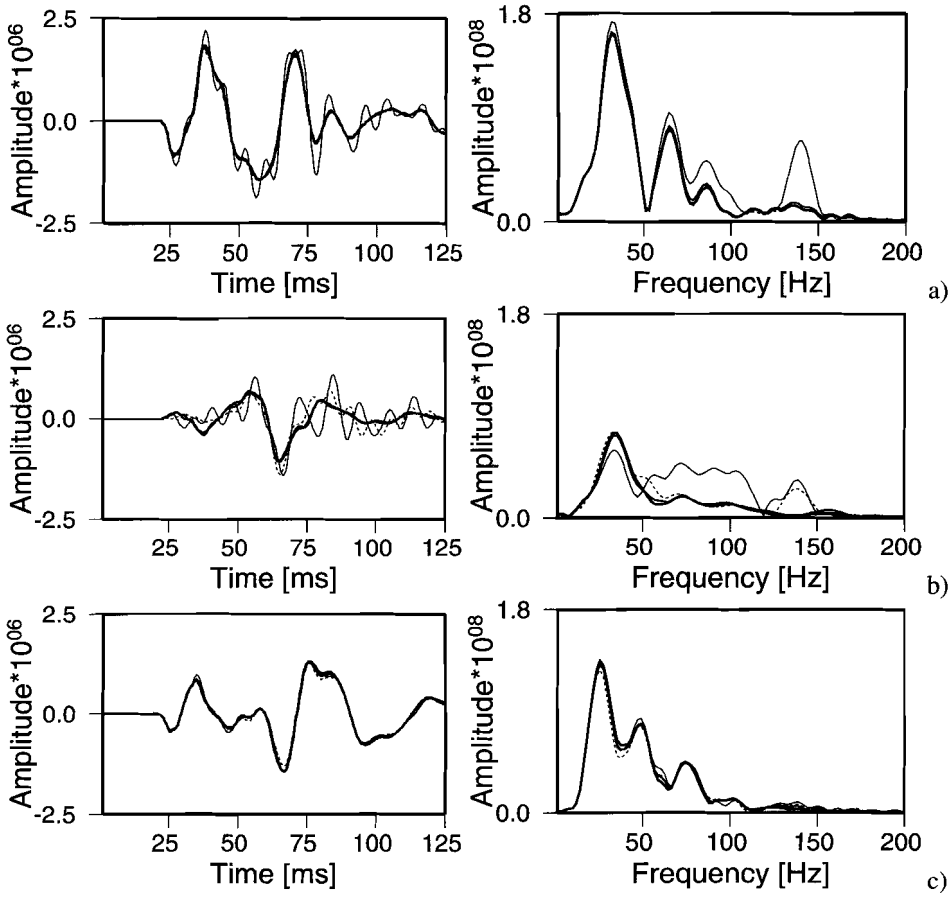

Figure 4.8: *Comparison of four differently coupled geophones in row #3, shot located south of geophone rectangle. Thick solid line: well-coupled geophone; middle solid line: geophone 0.5 cm above ground; thin solid line: geophone well above ground; dotted line: tilted geophone. The left column shows the traces, the right one the spectra. a): inline-horizontal component; b): cross-line horizontal component c): vertical component.*

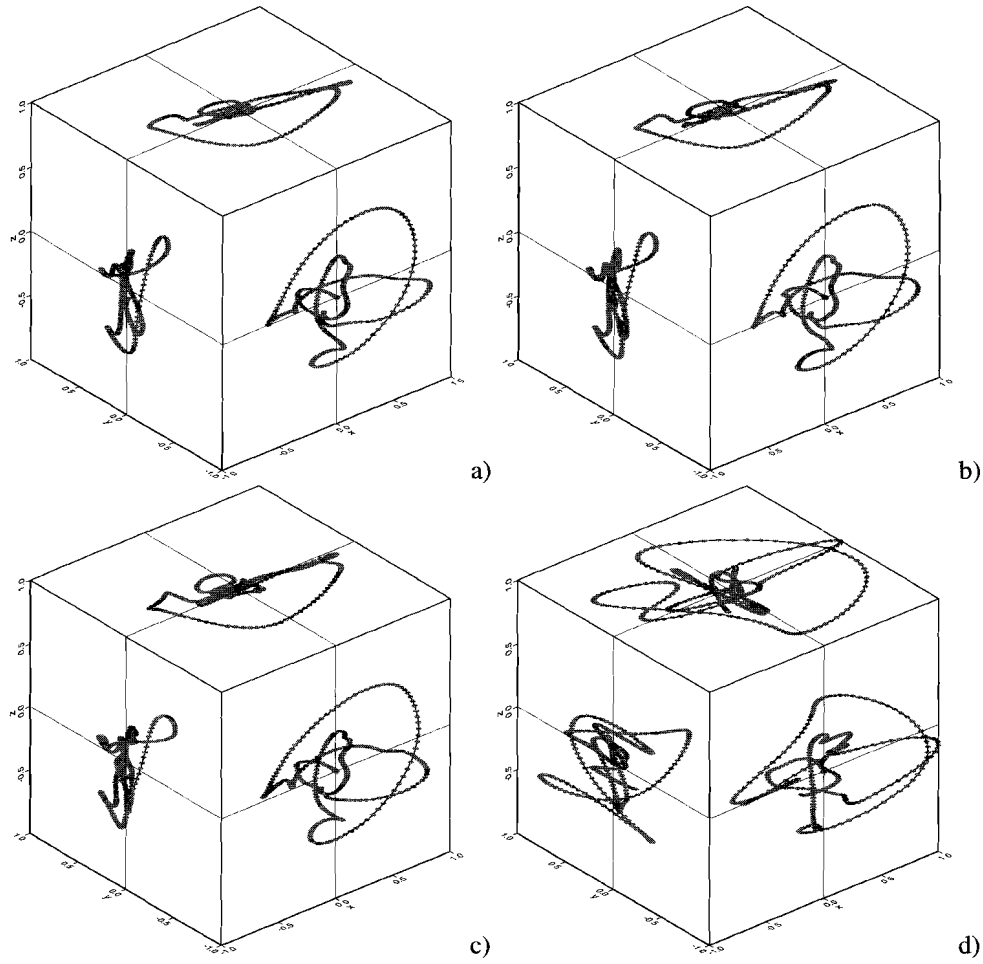

Figure 4.9: *Projection of the three-dimensional particle motion measured by the three-component geophone shown in the right-hand side of Fig. 4.6 onto the zx-, xy- and yz-plane. Shown is the data from the shot south of the array, row #2 a): Well-coupled geophone. b): Geophone 0.5 cm above ground. c): Tilted geophone d): Geophone well above the ground. All projected particle motion diagrams have a common scaling factor.*

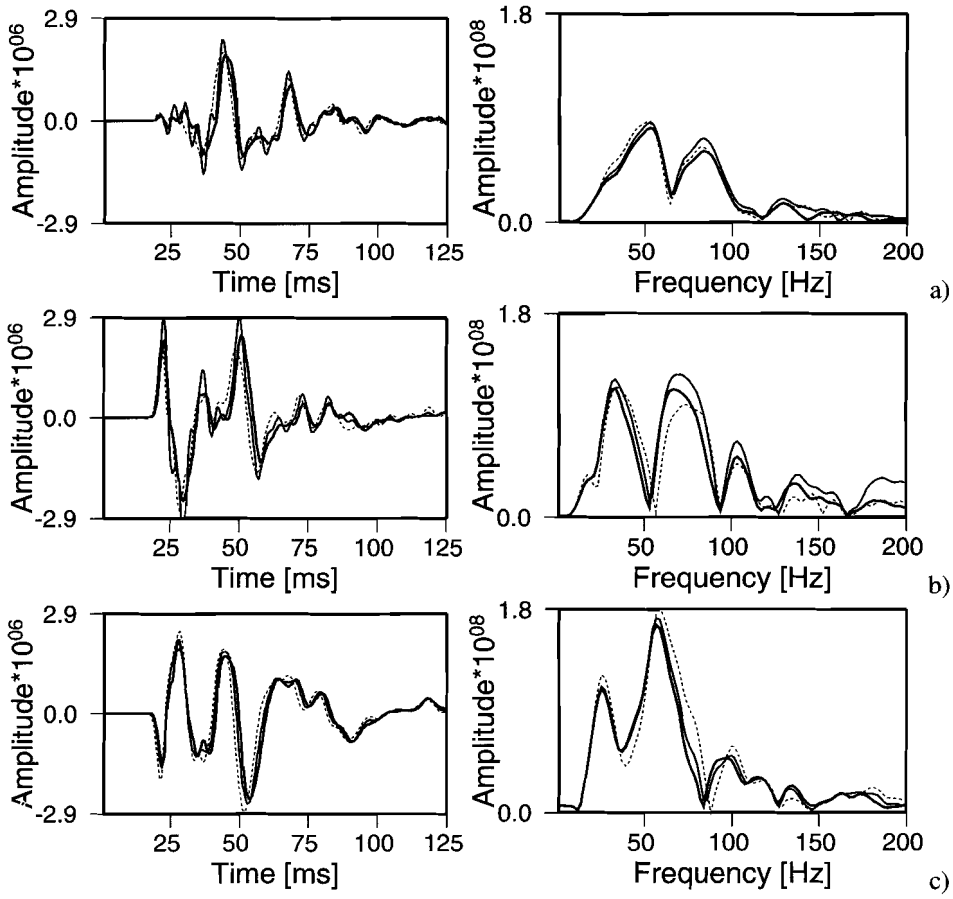

Figure 4.10: *Comparison of four differently coupled geophones in row #1, shot located west of geophone rectangle. Thick solid line: well-coupled geophone; middle solid line: geophone 0.5 cm above ground; dotted line: tilted geophone. The left column shows the traces, the right one the spectra. a): Inline-horizontal component; b): Cross-line horizontal component c): Vertical component.*

4.4 Free surface effects

4.4.1 Theory

Since receivers in a land survey are planted at the surface they do not record the true motion for the up-going waves but rather their interaction with the boundary. The surface can be regarded as a free surface and normal and tangential stress in the solid vanish at the surface. SH-waves incident on the free surface suffer no conversion and are recorded with twice their amplitude. P- and SV-waves, however, lead to a reflected and a mode-converted phase (see Fig. 4.11). The amplitude relations between the waves for such coupled systems have been derived by many authors each preferring his own notation (e.g. Meissner (1965), Aki and Richards (1980), Kähler and Meissner (1983), Evans (1984), Dankbaar (1985)). Following the notation given by Sheriff and Geldart (1995) and using the sign convention given by Aki and Richards (1980) the displacements at the vertical (u_3) and inline-horizontal (u_1) receivers for the plane-wave P-SV coupled system can be written as:

$$\begin{aligned} u_1(t) &= A_0 \sin\delta_p e^{i\omega(p(x-z\cot\delta_p)-t)} \\ &\quad + A \sin\delta_p e^{i\omega(p(x+z\cot\delta_p)-t)} \\ &\quad + B \cos\delta_s e^{i\omega(p(x+z\cot\delta_s)-t)} \qquad (4.1) \\ u_3(t) &= -A_0 \cos\delta_p e^{i\omega(p(x-z\cot\delta_p)-t)} \\ &\quad + A \cos\delta_p e^{i\omega(p(x+z\cot\delta_p)-t)} \\ &\quad - B \sin\delta_s e^{i\omega(p(x+z\cot\delta_s)-t)} \qquad (4.2) \end{aligned}$$

and for the SV-P coupled system as:

$$\begin{aligned} u_1(t) &= B_0 \cos\delta_s e^{i\omega(p(x-z\cot\delta_s)-t)} \\ &\quad + B \cos\delta_s e^{i\omega(p(x+z\cot\delta_s)-t)} \\ &\quad + A \sin\delta_p e^{i\omega(p(x+z\cot\delta_p)-t)} \qquad (4.3) \\ u_3(t) &= B_0 \sin\delta_s e^{i\omega(p(x-z\cot\delta_s)-t)} \\ &\quad - B \sin\delta_s e^{i\omega(p(x+z\cot\delta_s)-t)} \\ &\quad + A \cos\delta_p e^{i\omega(p(x+z\cot\delta_p)-t)}. \qquad (4.4) \end{aligned}$$

The displacement amplitudes of the up-going P- and SV-wave are denoted by A_0 and B_0, respectively, and those of the down-going P- and SV-waves are denoted by A and B. δ_p and δ_s are either angle of incidence or reflection for the P- and SV-waves, respectively, and p is the horizontal slowness. Using the boundary conditions, the displacement ratios of the down-going and up-going waves, better known as reflection coefficients, can be

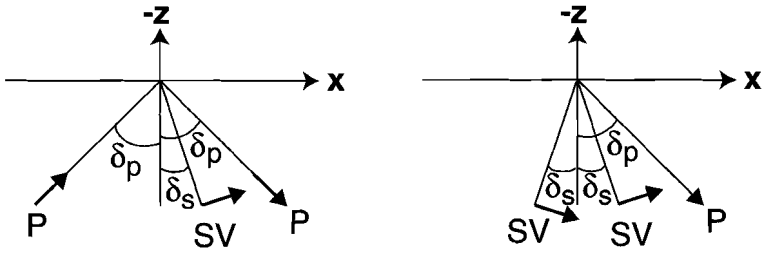

Figure 4.11: *Sign convention for coupled P-SV (left-hand side) and SV-P system (right-hand side): the displacement polarity of a wave for a certain receiver component is taken as positive if the component of the displacement vector, indicated by the arrow, is pointing in the direction of a positive axis. Note that the displacement vectors are chosen such that all horizontal displacements are positive. In many textbooks, the positive displacement vector for the SV-wave is chosen to be perpendicular to the direction of propagation and the positive y-axis (e.g., Sheriff and Geldart (1995)).*

expressed as:

$$\frac{A}{A_0} = \frac{\mu - \nu}{\mu + \nu} \tag{4.5}$$

$$\frac{B}{A_0} = \frac{2}{\mu + \nu} \tag{4.6}$$

$$\frac{A}{B_0} = \frac{2\mu\nu}{\mu + \nu} \tag{4.7}$$

$$\frac{B}{B_0} = \frac{\nu - \mu}{\mu + \nu} \tag{4.8}$$

$$\mu = \frac{v_s}{v_p}\tan(2\delta_s)$$

$$\nu = \frac{v_p}{v_s}\frac{\cos(2\delta_s)}{\sin(2\delta_p)}$$

Rewriting the normalised Eqs. 4.1 through 4.4 using Eqs. 4.5 through 4.8 gives:

$$\frac{u_1(t)}{A_0} = \frac{2}{\mu + \nu}(\mu \sin\delta_p + \cos\delta_s)e^{i\omega(px-t)} \tag{4.9}$$

$$\frac{u_3(t)}{A_0} = -\frac{2}{\mu + \nu}(\nu \cos\delta_p + \sin\delta_s)e^{i\omega(px-t)} \tag{4.10}$$

$$\frac{u_1(t)}{B_0} = \frac{2\nu}{\mu + \nu}(\mu \sin\delta_p + \cos\delta_s)e^{i\omega(px-t)} \tag{4.11}$$

$$\frac{u_3(t)}{B_0} = -\frac{2\mu}{\mu + \nu}(\nu \cos\delta_p + \sin\delta_s)e^{i\omega(px-t)} \tag{4.12}$$

The angle of incidence for the coupled P-SV system (apparent angle) deviates from that of the up-going P-wave. Fig. 4.12 shows the difference between the true and apparent angles. For small Poisson's ratios and angles of incidence the difference is negative. This means that energy is shifted towards the inline-horizontal component. Positive values indicate that the energy is shifted towards the vertical component.

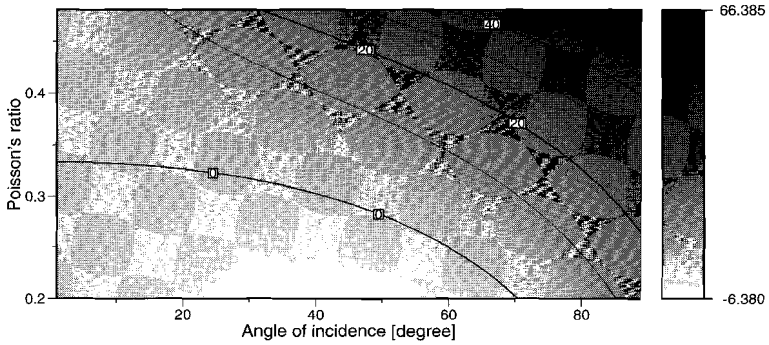

Figure 4.12: *Difference between apparent (measured) angle of incidence for coupled P-SV system and true angle of incidence of the up-going P-wave for various Poisson's ratios and angles of incidence.*

Coupled SV-P systems behave differently. At incidence angles smaller than critical angle there is not much difference between the true and the apparent angle of incidence (the tilt angle can be taken as the angle of incidence as long as the recorded SV-P coupled system is linearly polarised). The upper figure of 4.13 shows that this difference slightly increases with increasing angle of incidence and decreases with increasing Poisson's ratio. Since these angles of incidences are small, the SV-wave is recorded mainly on the horizontal component. The picture changes dramatically beyond this angle, since the angle of reflection for the converted waves becomes imaginary and the P-wave inhomogeneous with a decreasing amplitude away from the interface. There is a phase difference between the receiver components so that the reciprocal ellipticity increases toward the maximum value of 1, which represents circular motion (see lower figure of 4.13). The bigger the Poisson's ratio the slower is the change from linear to circular motion. The tilt angle (measured from the inline-horizontal axis) beyond the critical angle is 0 indicating that the axes of the particle motion ellipse are perpendicular and parallel to the surface. At 45° the motion becomes purely linear along the vertical axis and then the ellipticity increases slowly again. In conclusion this means that beyond the critical angle there is always a bigger amount of the SV-wave mapped onto the vertical than onto the horizontal component.

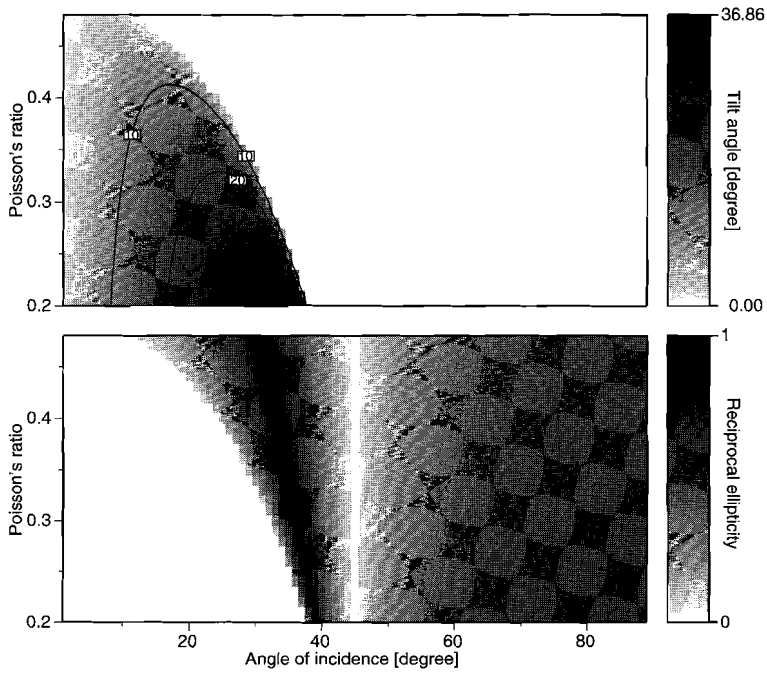

Figure 4.13: *Upper figure: Tilt angle of coupled SV-P system. Lower figure: Reciprocal ellipticity of coupled SV-P system*

4.4.2 Estimation results

Applying the wavefield separation method to such coupled systems leads to the estimation of apparent parameters not only for the slowness, but also for the polarisation angle and phase difference. The method is able to separate coupled wave systems from each other using the apparent values as long as the plane wave assumption is not violated inside the analysis window. Using Eqs. 4.9 through 4.12, noise-free synthetic data at the free surface were modelled using bandwidth-limited wavelets with 50 Hz and 30 Hz central frequency for the P- and S-wave, respectively, and width of 50 Hz (i.e., the same kind of wavelet that was used so far for modelling the synthetic plane wave data). Trace to trace distance was 0.5 m, near offset 15 m, far offset 100 m, which is equivalent to an angle of incidence of 45.°. The Poisson's ratio for the model was $\frac{1}{3}$.

Fig. 4.14 gives the histograms for all moving analysis windows, each containing three traces. The parameters for the coupled P-SV system are estimated correctly for all offsets. The phase difference is well estimated also for the coupled SV-P system. The polarisation angle deviates from the true value around the critical angle of incidence and continues to be too low. The difference diminishes for increasing offset, indicating that the parameter variation with offset decreases. The slowness shows a similar behaviour, but the estimated

values are too high.

4.4.3 Inversion

The final decomposition into up- and down-going wavefields can be done if the amplitude and the angle of incidence for the up-going wave are known. Otherwise, these parameters must be deduced from the data via an inversion scheme. We have chosen to use an extensive grid-search method with regular step-size. The upper and lower search boundaries for each parameter can of course be restricted if a priori information is available. We have three parameters that have to be matched, the displacements at the vertical and inline-horizontal receivers and the preservation of energy. At each point we compute the rms error between modelled and observed data and the parameter combination with the minimum error is given as output. Note, that the Poisson's ratio is also a free parameter. Figs. 4.15, 4.16 and 4.17 show the rms errors for a synthetic P-SV coupled system at an angle of incidence of 40 °. For other angles of incidence the figures are very similar to Figs. 4.15 and 4.16, but Fig. 4.17 can change considerably. The Poisson's ratio was $\frac{1}{3}$ and the amplitude of the up-going wave 1. For each figure one parameter was kept at its correct value: the angle of incidence (Fig. 4.15), the Poisson's ratio (Fig. 4.16) and the amplitude of the up-going wave (Fig. 4.17). The search boundaries are listed in Table 4.4. The least sensitive parameter is the Poisson's ratio. This becomes clear when we apply the inversion to the data that was used for producing Fig. 4.14.

parameter	lower value	upper value	step size
angle	1.	89.	1.
Poisson's ratio	0.25	0.45	0.01
amplitude	0.1	5.	0.1

Table 4.4: *Search limits for extensive grid-search.*

All 171 traces were analysed with the search parameters as listed in Table 4.4 (constraint #1). Each trace was Fourier-transformed and only the maximum amplitude was used in the inversion. This resulted in the dotted curves in Fig. 4.18. For most of the traces, the results deviate from the true values (dashed curves). This misfit always occurs if the sampling for the angle of incidence is too coarse. Refining the grid is a solution which results in better estimates, but there are still some traces were a misfit will occur. A better result can be obtained if the upper boundary of the Poisson's ratio is constrained to 0.35 (constraint #2, solid curve in Fig. 4.18). That means that a priori information on this parameter is necessary to obtain stable results for realistic data. Using the estimated values for wavefield decomposition resulted in a nearly perfect match between the original up- and down-going waves and the decomposed ones. We used the wavefield separation

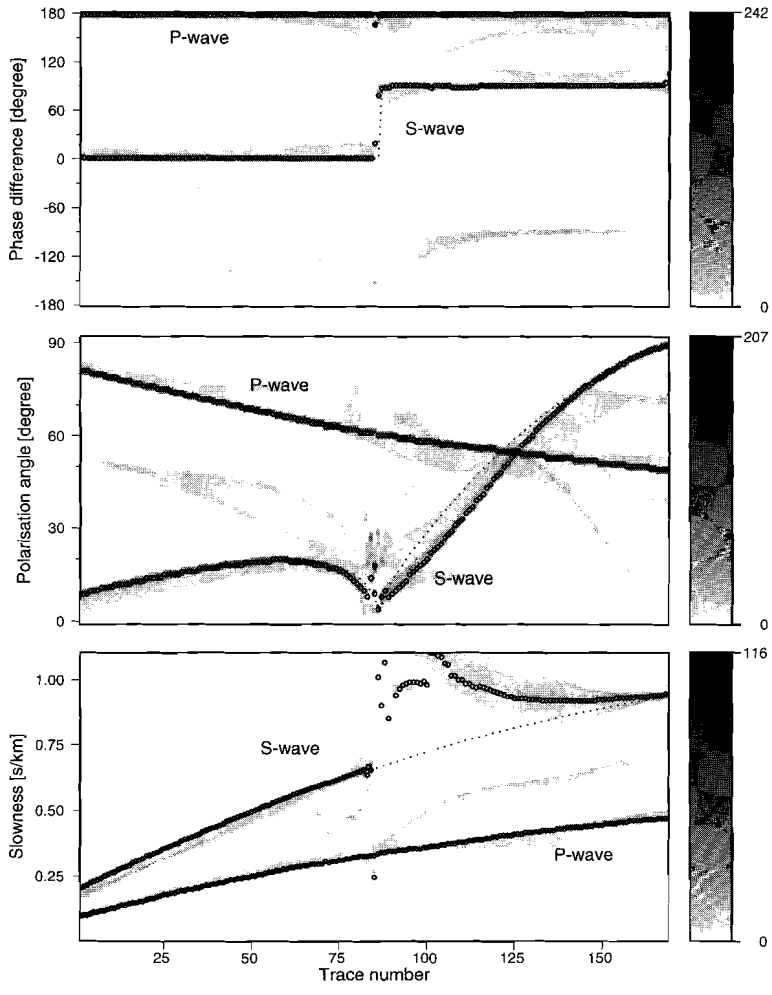

Figure 4.14: *Histograms for the synthetic free-surface data. The dotted and dashed curves represent the parameters of the coupled SV-P and P-SV systems, respectively. The latter curve is not visible because the P-wave parameters are well estimated and plotted on top of it. The circles represent the estimated values based on tracing back the phase difference values. The linear grey-scale next to each plot shows the value of the summed magnitude for each bin.*

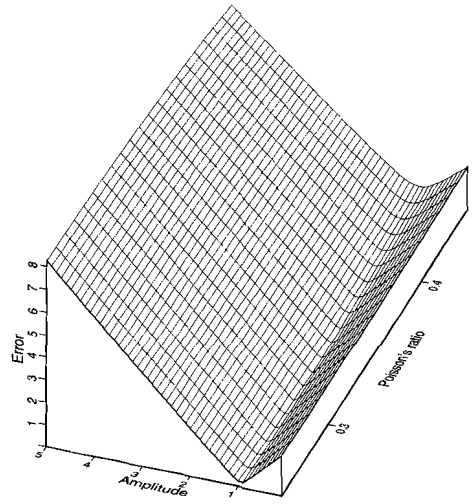

Figure 4.15: *The rms error for a coupled P-SV system. The angle of incidence was fixed at the correct value.*

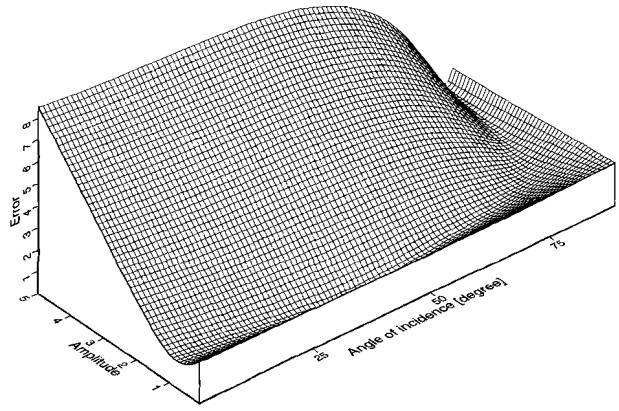

Figure 4.16: *The rms error for a coupled P-SV system. The Poisson's ratio was fixed at the correct value.*

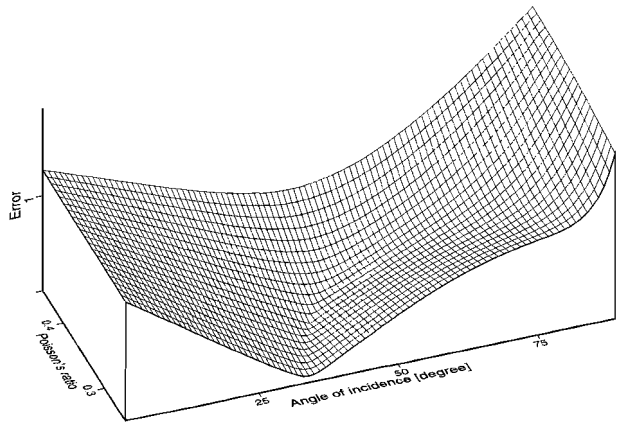

Figure 4.17: *The rms error for a coupled P-SV system. The amplitude was fixed at the correct value.*

as described in Section 2.2.3 and changed only Eq. 2.10 to:

$$\begin{pmatrix} U_3 \\ U_1 \\ 0 \end{pmatrix} = \begin{pmatrix} -\cos\delta_p & \cos\delta_p & -\sin\delta_s \\ \sin\delta_p & \sin\delta_p & \cos\delta_p \\ A_0 & -A & -B \end{pmatrix} \begin{pmatrix} W_p^{up} \\ W_p^{down} \\ W_s^{down} \end{pmatrix},$$

with parameters δ_p, δ_s, A_0, A, and B as described in the beginning of this section.
When the results obtained with constraint #1 were used in separation there was of course a mismatch between the original up- and down-going waves and the decomposed ones.

4.5 Conclusions

Large statics prevent a successful wavefield separation. There is also no possibility to correct for the time shifts if waves interfere with each other. The bigger the lateral variation of the weathering layer, the more densely the wavefield must be sampled to reduce the effect of static shifts. However, if there is not sufficient move-out difference between waves and if both waves have similar central frequencies, then the parameter estimation may still fail (see Figs. 3.13 and 3.14 for comparison).
Changes in coupling inside the analysis window will degrade the parameter estimation. Trace balancing the data prior to estimation improves the results for the phase difference estimates, but slowness and polarisation estimates can still be erroneous for traces with interfering waves. A field experiment conducted with three-component orthogonal geophones showed that the vertical geophone is virtually insensitive to changes in coupling and slightly sensitive to tilting. The horizontal geophone shows mono-frequent ringing if the coupling is greatly reduced and a decreased amplitude for tilting.
Analysis of data recorded on land yields the parameters for the coupled wave systems. Inversion for the angle of incidence and amplitude of the up-going wave and the Poisson's

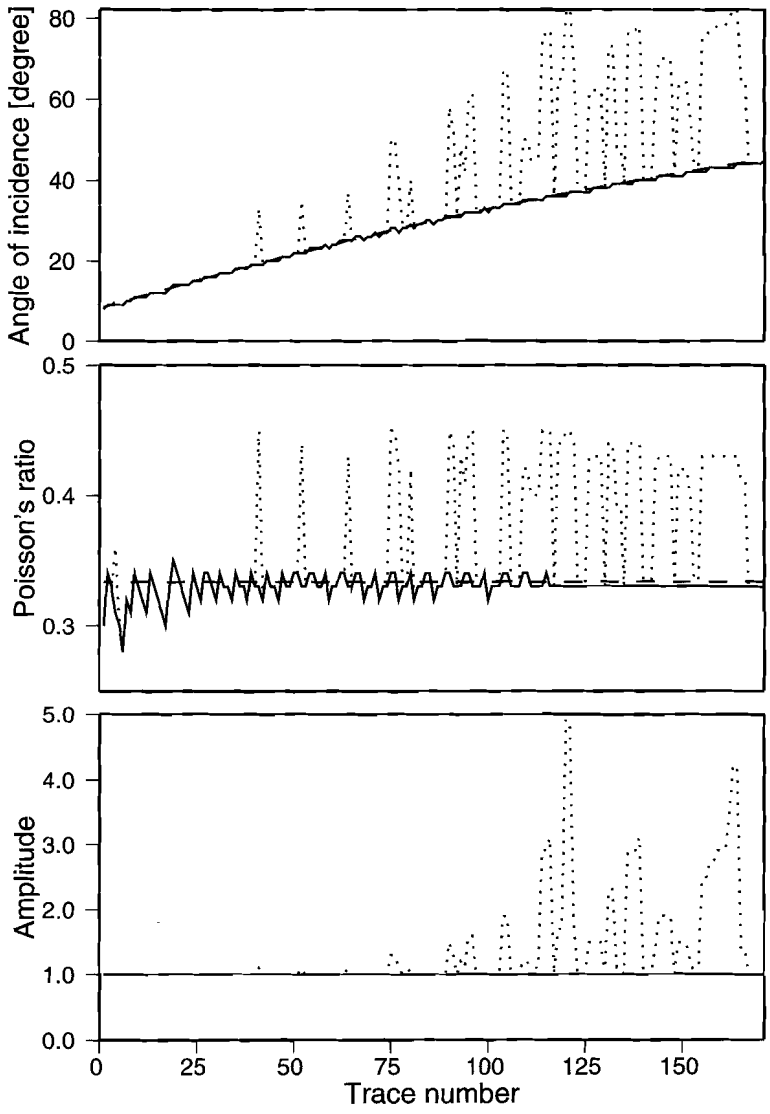

Figure 4.18: *Comparison of true values (dashed), inverted values with constraint #1 (dotted), and inverted values with constraint #2 (solid) for the synthetic coupled P-SV system.*

ratio of the near surface is possible. We used the extensive grid search method, which needs a dense sampling of the angle of incidence for correct results. Constraining the Poisson's ratio improved the results even if the sampling of the angle is coarse. The inversion results were used for decomposing a synthetic P-SV-system. Similar results are expected for the analysis of the SV-P-coupled system. Noise will certainly cause problems for the inversion. The robustness could be increased by including more frequencies in the analysis. Depending on the wavelet however, each frequency is associated with a different amplitude of the up-going wave. This could be compensated for by normalising the amplitudes. Inversion results could be interpolated and smoothed by comparing the results obtained from adjacent receivers.

Chapter 5

INDUSTRY DATA

5.1 Introduction

Real data consist of several wave types and reflections and diffractions having non-linear move-outs can be regarded only approximately as plane waves. Refractions have linear move-outs but they are recorded only from the critical distance on. They will therefore hamper the analysis in the time-offset window that includes this critical offset and therefore the onset of this wave. This influence of non-linear and non-continuous events on the parameter estimates will be illustrated using a noise-free data set created with an elastic 2D finite difference code.
The ability to successfully apply the method to industry data will depend greatly on the data quality. In addition to possible low S/N ratios, the presence of dispersive waves, spatial aliasing, and differences in amplitudes, statics, coupling differences and the free surface will play a role too. We have analysed two different shot gathers provided by the Shell Geophysical Department of SIEP-SEPTAR, and the NAM (Nederlandse Aardolie Maatschappij), respectively, and present the results below.

5.2 Separation of waves from an FD-data set

The synthetic data used until now lack an important feature of real seismic data, namely a change of the characteristic parameters with offset. Therefore, we applied the method to a shot gather without noise (see Fig. 5.1) created by an elastic 2-D finite-difference code to see how the method performs on such data. The trace spacing on the records was 25 m. The parameters of the 2-D model underneath the shot point location are given in Table 5.1. Generally, layers are gently dipping to the right and interfaces are smooth curves, and the elastic parameters are constant in each layer. The free-surface effect was included in the data. Estimated parameters therefore belong to coupled wave systems.
We chose three different windows (see Fig. 5.1) to perform the estimation and separation procedure, each window demonstrating a different aspect of using the method. The exact window parameters are listed in Table A.1.

5.2.1 Data window ①

This window lies inside the cone formed by the Rayleigh-wave arrival (see Fig. 5.1). Two dominant waves are visible in the window besides a few less pronounced arrivals. The estimation was carried out for four waves using 9 traces in the analysis window. The two dominant slownesses are plotted on the left-hand side in Fig. 5.2 as functions of the trace

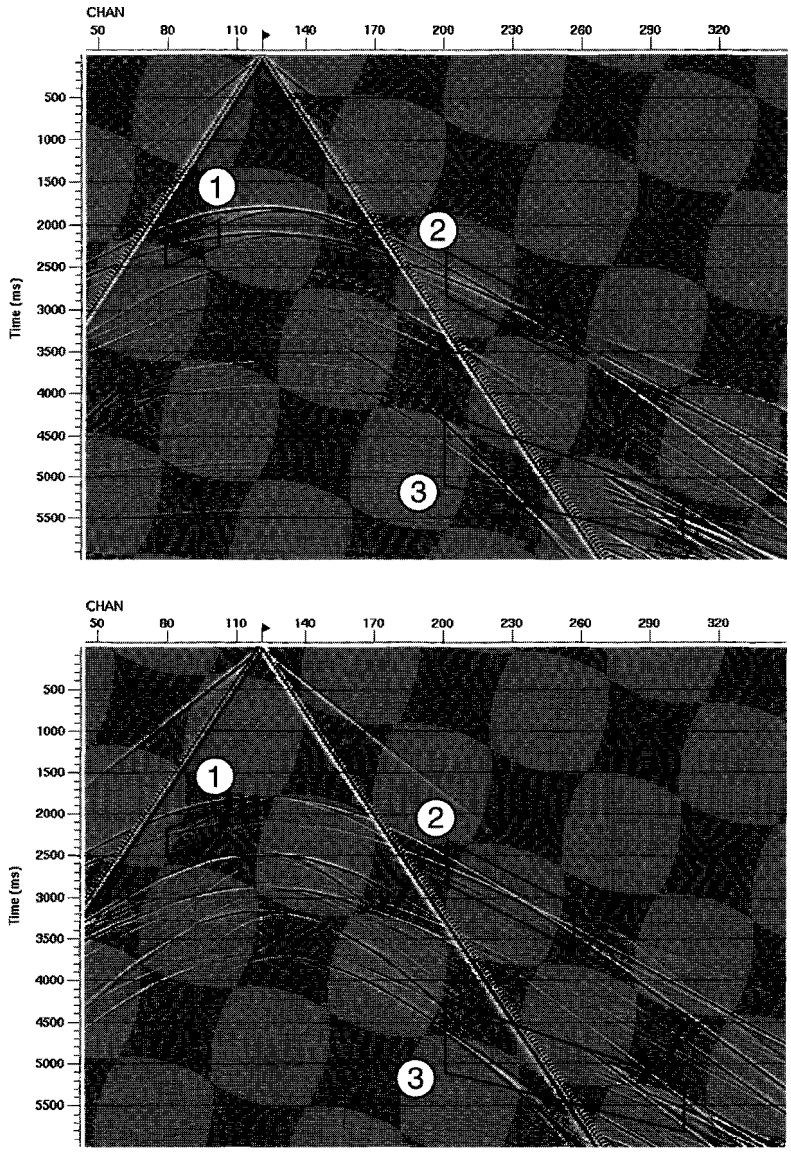

Figure 5.1: *Vertical (upper panel) and inline-horizontal component of the synthetic shot gather (for medium parameters see Table 5.1). The three windows indicate the areas used in the analysis. The data were provided by the Shell Geophysical Department of SIEP-SEPTAR. Note: No common amplitude scaling was used for these plots.*

thickness [m]	v_p [m/s]	v_s [m/s]	ρ [g/cm^3]
1035.	1147.150	655.514	2.20
244.	1669.790	954.166	2.45
1372.	2369.765	1354.151	2.30
1711.	2162.198	1235.542	2.35
764.	2640.550	1508.886	2.40
half-space	3000.000	1714.286	2.70

Table 5.1: *Model parameters underneath the shot location for synthetic data of Fig. 5.1. v_p and v_s denote P- and S-wave velocities, respectively, ρ is the density.*

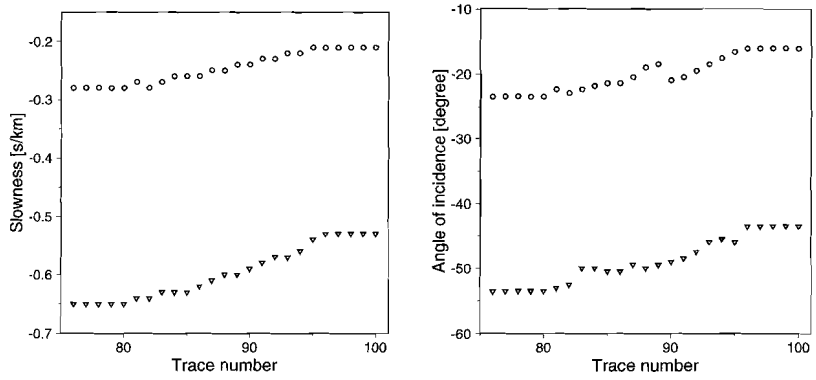

Figure 5.2: *Slowness and angle of incidence for data window ① in Fig. 5.1. Inverted triangles and circles represent values for the diffraction and reflection, respectively.*

number. Both curves show an increasingly negative slowness with offset (decreasing trace number). The polarisation angle and phase difference values were translated into angle of incidence values (two curves on the right-hand side in Fig. 5.2); these also show an increasingly negative angle for increasing offset. Both waves are P-waves, one is the reflected phase from the second interface, the second is a diffraction from a roughness in the first interface. This was concluded from a compilation of successive snap-shots which shows the propagation of the elastic wavefield in the model at discrete time steps. The characteristic parameters were used for the separation procedure and the two extracted dominant waves are shown in Fig. 5.3: in the left panel the reflected phase from the second interface is shown and in the right panel the diffraction. Both waves are separated well from each other but some energy of the weak arrivals, having characteristic parameters close to those of the dominant waves, were mapped too. Both waves were projected back onto the receiver components and subtracted from the data to check how much of the original energy in data window ① is still unexplained. The result shown in Fig. 5.4 depicts little coherent residual energy, indicating a successful extraction of the two waves. The vertical component of the residual data set has 26 % of the mean energy of the original

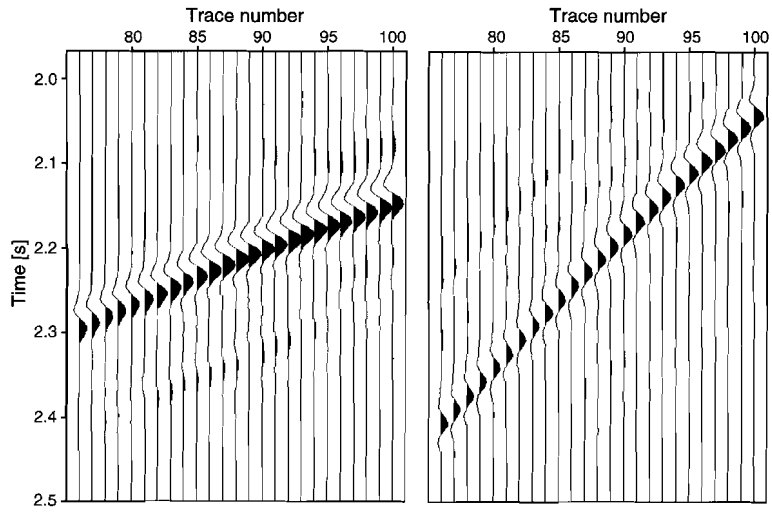

Figure 5.3: *The two dominant waves from data window ① (prior to projection onto the receiver components): Reflected P-wave from the second interface (left panel) and diffracted P-wave from a roughness in the first interface (right panel). Note: All panels in Figs. 5.3 and 5.4 have a common amplitude scaling.*

data, the inline-horizontal component 30 %.

5.2.2 Data window ②

The same analysis (again expecting four waves) was performed for data window ② outside the Rayleigh-wave cone where two dominant waves are visible. In Fig. 5.5 slowness and angle of incidence estimated from an analysis window 9 traces wide are shown as functions of trace number. All curves for the two dominant waves show increasing values for an increasing offset (increasing trace number). The two dominant waves present are again P-waves, this time reflected at the first and second interface, respectively. There are two more waves in window ②, a refraction (from the third layer as indicated by the apparent velocity) being faster than the reflected phase from the first layer around channel 230 and an arrival that might be explained by a wave that is reflected at the second interface but travels one way between first and second interface as an S-wave (concluded from the snap-shots). Both waves are much weaker in amplitude than the two dominant waves and therefore, their parameters are not estimated well.

The estimates show more scatter in the centre of data window ② (see Fig. 5.5). One explanation could be that the difference in apparent slowness between the refracted wave and the reflection from the second interface is too small and the estimate of the latter is therefore biased for some points to smaller slowness values. Another explanation could be that the refracted wave only exists from the critical distance on. Therefore, the assumption

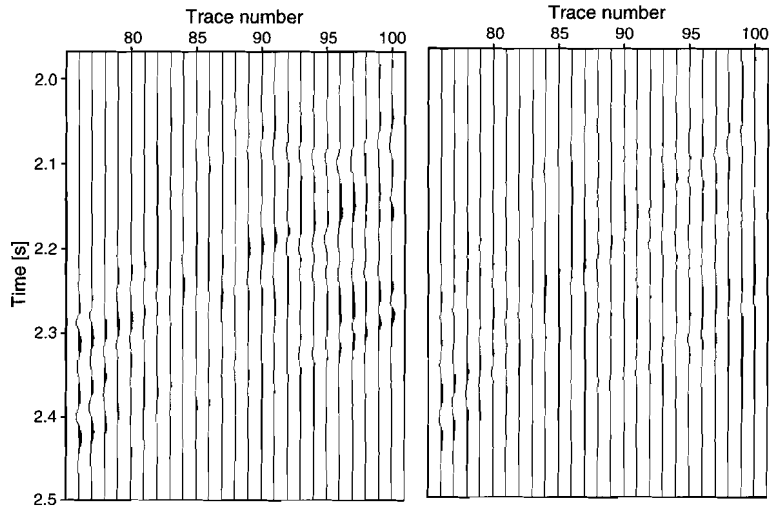

Figure 5.4: *Vertical (left) and inline-horizontal (right) component of the residual data after subtracting the two dominant waves from window ①. Note: All panels in Figs. 5.3 and 5.4 have a common amplitude scaling.*

that the transfer matrix between units is the same is not valid for some of the units in this data window. Assuming that the critical distance is reached around channel 230, we expect maximum scatter on channels 225 to 235. The scattering is indeed pronounced in this region (see Fig. 5.5). All estimates were used to separate the waves present in window ② and the result is shown in Fig. 5.6. The better estimated reflection from the first interface (inverted triangles in Fig. 5.5 and right panel of Fig. 5.6) also shows a more coherent waveform than the separated wave in the left panel (reflection from the second interface). Again, both waves were projected back onto the receiver components and subtracted from the data present in window ②. Most of the unexplained energy in the residual panels (not shown) is situated around those trace numbers which also show more scattering in Fig. 5.5. The drop in mean energy on the residual data is nevertheless bigger than for the results from data window ①: only 23 % of the mean energy of the original vertical and 17 % of the inline-horizontal component are still unexplained.

5.2.3 Data window ③

The analysis in data window ③ was done in order to extract the weak P-wave reflection from the 4th interface. This event enters data window ③ at 5000 ms and successively interferes with other arrivals, all of them exceeding it in amplitude. The spatially aliased high-amplitude Rayleigh wave cutting through the middle of the window requires special treatment. The data window was therefore split into three sub-windows. Otherwise, the analysis could have been carried out for the whole data window assuming 6 waves to be

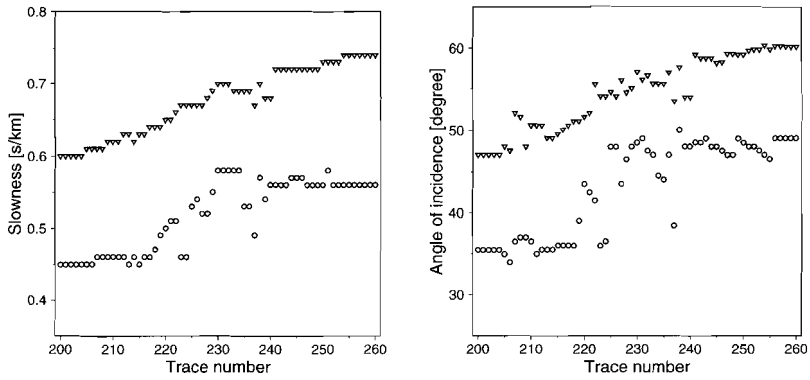

Figure 5.5: *Slowness (left-hand side) and angle of incidence (right-hand side) for window ② in Fig. 5.1. Inverted triangles and circles represent values for the reflection from the first and second interface, respectively.*

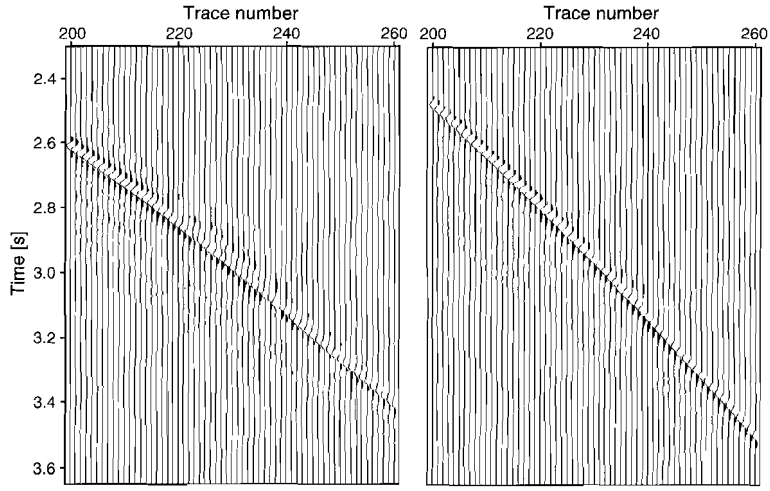

Figure 5.6: *The separated waves from window ②. In the left panel the reflection from the second interface is shown, in the right panel the reflection from the first interface. Note: The two panels have a common amplitude scaling.*

present. Problems, however, could then be expected for regions where events enter or leave the window (e.g. around trace 230; see also data window ② for comparison).

- The left sub-window **a** additionally contains two strong arrivals. The analysis was carried out for 4 waves using 7 traces in each analysis window. The wave having a higher apparent slowness was identified as a linearly polarised S-wave, but the other estimates indicated neither the slower wave clearly nor the P-wave. Finally, all estimated parameters were smoothed and separation for 4 waves was carried out. The S-wave was then projected back onto the receiver components and subtracted from the left sub-window. The analysis was repeated with the residual data, and parameter estimates characteristic of the P-wave reflection were now obtained in many of the analysis windows. Values for the missing estimates were interpolated and separation was carried out. The extracted P-wave, projected back onto the receiver components, is shown in Fig. 5.7**a**. There is still some energy left from the two dominant waves. The result may be improved further by smoothing the polarisation estimates of the slower wave more carefully than previously done, because this wave exhibits a change from elliptical to nearly linear polarisation shortly before interfering with the S-wave. Furthermore, there is evidence of a newly developing arrival just in the interference zone, which might have influenced the parameter estimation and led to the sub-optimal separation result.

- The middle sub-window **b** contains the dominant Rayleigh wave, which is spatially aliased. Therefore, we use the modified statistical analysis applied to the phase instead of the slowness estimates. The estimated parameters for the Rayleigh wave differed slightly for most of the analysis windows. Since its amplitude was approximately 35 times higher than that of the P-wave it was essential to match the waveform of the Rayleigh wave as well as possible in order to remove it from the record. Therefore, a single (best-matching) parameter set, found by visual inspection, was used over the whole window. Since the parameter estimation was not perfect it resulted in a residual, but low-amplitude, Rayleigh wave. Now it was possible to separate in the second iteration the P-wave from this residual Rayleigh-wave energy and the projected P-wave is shown in Fig. 5.7**b**. In contrast to the left sub-window, where the amplitude of the dominant waves was only approximately 6 times higher than that of the P-wave, there is no energy left from the strong Rayleigh wave. This is due to the fact that its parameters do not show a variation with offset.

- In the the right sub-window **c** a number of waves having comparable amplitudes are interfering with each other. After having estimated the parameters of 6 waves, the P-wave estimates were smoothed and separation for 6 waves was carried out. The P-wave was then projected back onto the components and is shown in Fig. 5.7**c**.

5.2.4 A remark on windowing

The question of how this method could be applied routinely in real data processing cannot be answered in a straightforward fashion. First of all, the data must be approximately

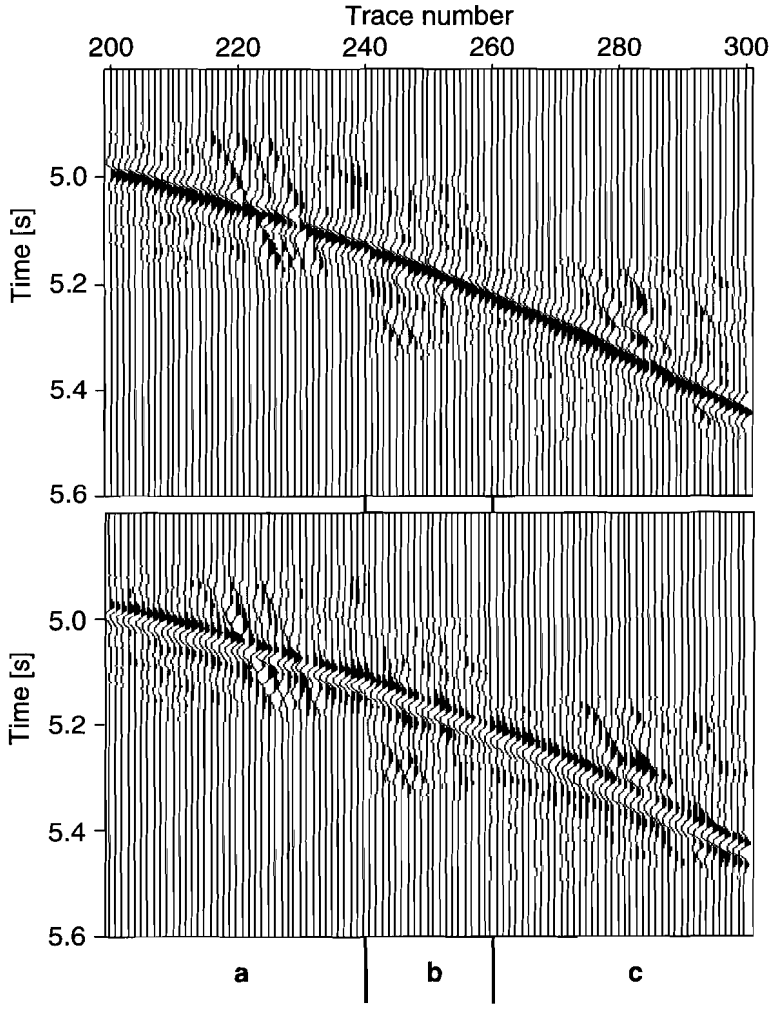

Figure 5.7: *Data window ③ in Fig. 5.1: Vertical (upper panel) and inline-horizontal (lower panel) component of the separated P-wave projected back onto the components. The letters and vertical bars indicate the three sub-windows. Note: No common amplitude scaling was used for these plots.*

planar. This also implies a sufficiently dense spatial sampling of the wavefield so that averaging effects are minimised. If a priori information is available this knowledge should be used to smooth and interpolate the estimated parameters in order to obtain a good separation. The critical question is, however, whether it would be possible to analyse whole shot gathers. The strength of the method is its lateral resolution which comes from the assumption that the wavefield can be regarded as being composed of a finite number of plane waves. In order to retain this lateral resolution the temporal window should be small to include only a few events, because each recorded event has its own unique parameter combination and must be considered in the analysis. One should first remove waves with a slowness completely different from the rest of the data because they further complicate the construction of data windows (see for example data window ③ in the previous section). The latter are chosen such as to accommodate the complexity of the data and the S/N ratio. The estimated values should then be first smoothed and corrected, perhaps interactively as in velocity analysis. After separation, the waves should be sorted into P-, SV- and converted wave (C-wave) shot panels for further processing. Interactive visualisation techniques can further aid a successful application of this method.

5.3 Land data set #1

The Shell Geophysical Department of SIEP-SEPTAR provided us with a typical shot gather from a nine-component land survey. Some acquisition parameters are listed in Table 5.2. We selected a subset of traces 220 to 380 for further analysis and Figs. 5.8 and 5.9 show the Zz- and Zx-component, respectively. Note: the upper and lower case letters indicate source and receiver directions, respectively. The shingling of the first arrivals (also called repeated initials) indicates the presence of a wave guide. There are numerous events present in the time window between the first arrivals and the Rayleigh wave having similar move-out. Without detailed knowledge about the geology it is difficult to interpret these arrivals. Similar patterns can also be found for shallow high-resolution reflection data, when energy is trapped between the surface and the water table (van der Hoff et al. (1996)). The occurrence of the dispersive guided waves not only narrows the so-called 'optimum reflection window' (the time-offset window between the first arrivals and the ground rolls where reflections are best observed), but these waves might also be misinterpreted as reflections (Robertsson et al. (1996)).
A first analysis of the data was done using complex trace analysis as proposed by René et al. (1986). At each sample the geometric mean of the envelopes (a measure for the energy of a certain event), the phase difference between the receiver components, the reciprocal ellipticity, and the tilt angle of the particle motion ellipse are computed. We use colour coding to display these parameters. The identification of the wave type is naturally only successful for non-interfering events. Analysis of the Zz- and Zx-components indicated that the first arrivals have retrograde elliptical motion with the major axis parallel to the vertical axis. The bundle of arrivals following the first breaks could not be identified due to interference.
The dominant wave in Figs. 5.8 and 5.9 is the Rayleigh wave. It interferes with the bun-

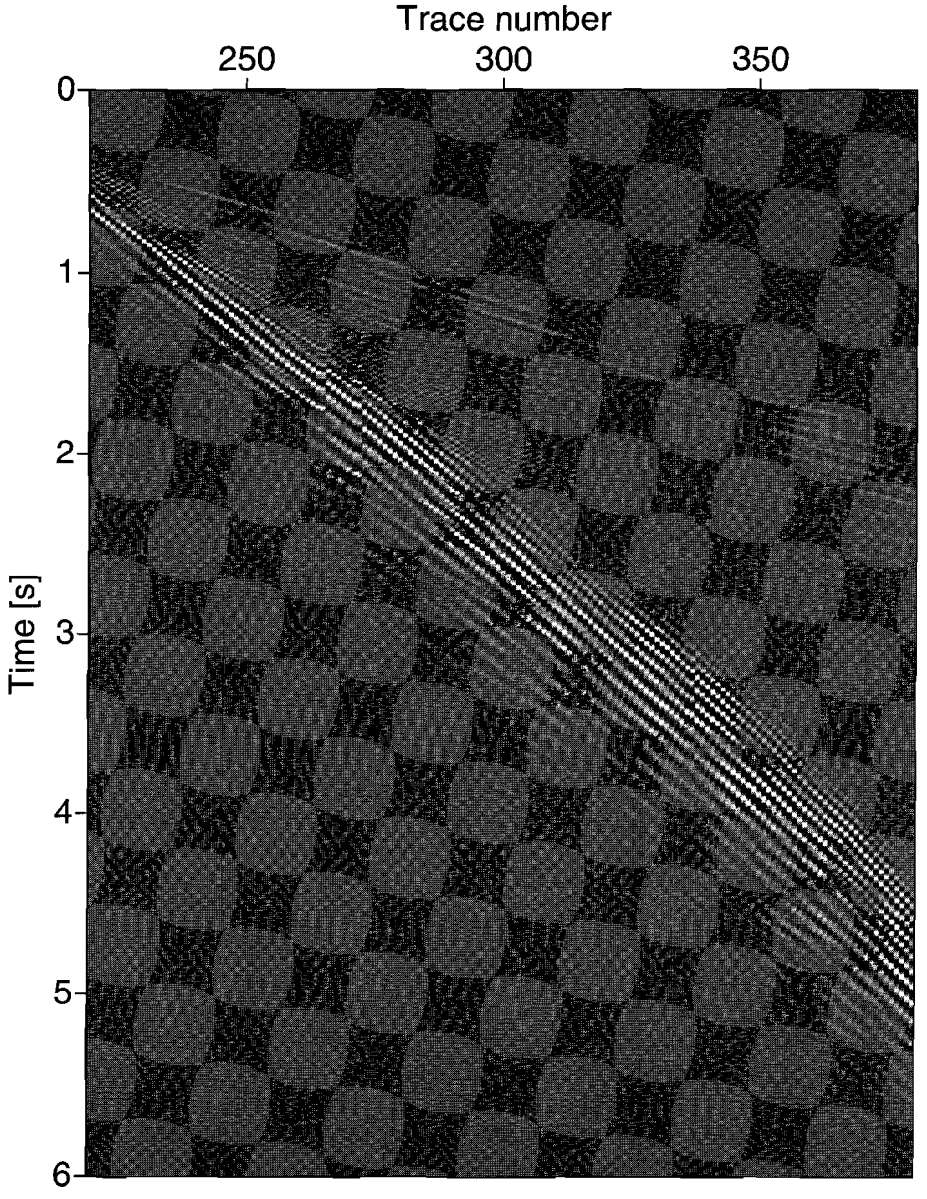

Figure 5.8: *Z_Z-component of data set #1. Note the shingling in the first arrivals. Each trace is scaled individually.*

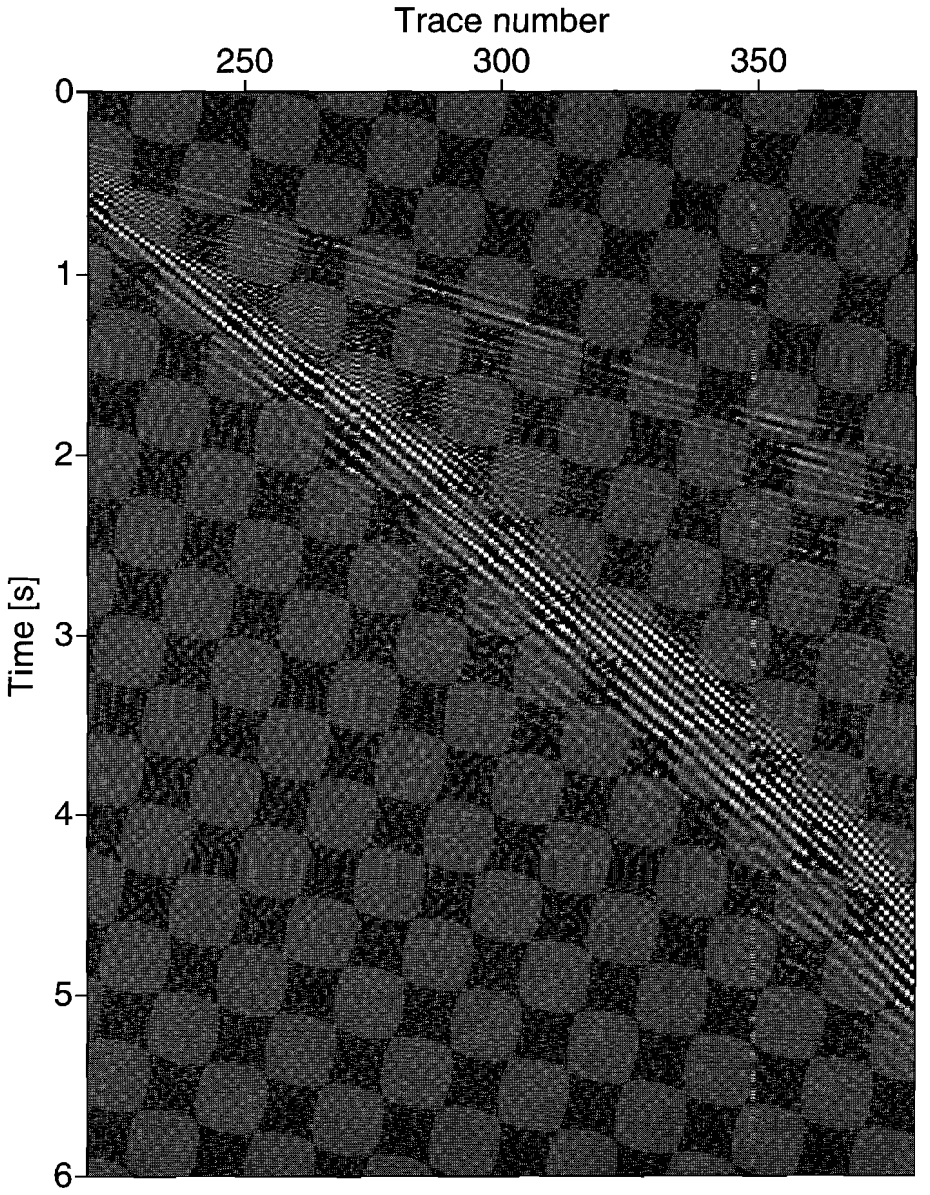

Figure 5.9: *Zx-component of data set #1. Each trace is scaled individually.*

source	P- and S-wave vibrators
sweep range	≈8-60 Hz
spread	split-spread
number of geophones	397
geophone type	3C (orthogonal)
receiver station interval	25 m
number of geophones in array	12

Table 5.2: *Acquisition parameters for data set #1*

dle of events at shorter offsets and thus we first attempted to remove this wave from the data in order to identify possible reflections inside the Rayleigh-wave cone. The chosen data window for iteration #1 corresponds to the total window shown in Figs. 5.8 and 5.9. Seven traces were used in the analysis (assuming two waves) yielding consistent parameters for the Rayleigh wave for all analysis windows. The second wave had consistently lower apparent slowness, a badly defined polarisation angle and a phase difference that alternated between P- and S-wave type for different analysis windows. No smoothing of the estimated parameters was applied prior to separation, but the data window was restricted to the area around the Rayleigh wave to prevent Rayleigh-type first arrivals from being mapped onto the Rayleigh wave output panel. Separation parameters are listed in Table 5.3.

The residual data still contained Rayleigh-wave energy. This energy had a higher apparent velocity and also higher frequency and arrived just before the lower frequency Rayleigh-wave energy we estimated in the first iteration step. In the second iteration step it was necessary to interpolate the estimated parameters for some of the analysis windows prior to separation. The second wave was again partly P-, partly S-type. During separation, the data window was again restricted to the ground roll region.

In the next step (iteration #3), parameters for a Rayleigh-type wave were estimated together with P- and S-type parameters. Separation with interpolated values yielded two similar output panels. The main difference is that the (Rayleigh-type) first arrivals were mapped only to the Rayleigh-type output panel and were not visible on the P-/S-wave panel. The former panel also contains fewer of the events following these first arrivals. The residual data are shown in Figs. 5.10 and 5.11. The mean energy for iterations #1 through #3 is shown in Fig. 5.12. There is a significant reduction of energy after the first iteration.

Having decreased the Rayleigh-type energy considerably it was finally attempted to separate the other events into P- and S-wave arrivals (iteration #4). The estimated parameters still indicate Rayleigh-type energy and are not conclusive about the correct parameters for the body waves. We attempted to force separation by using parameters obtained from analysis windows #1 and #8 for the P- and S-waves, respectively (see Table 5.3). This attempt failed; both output panels were quite similar and subtracting the P-wave from the data yielded an increase of the mean energy instead of a decrease. This shows that the

parameters were not chosen properly to explain the energy present on the residual panels after iteration #3.

Iteration	wave-type	ξ [°]	θ [°]	p [s/km]
#1	R	≈-90	≈65	≈1
	P/S	180/0	var (↓)	≈0.25
#2	R	≈-90	≈60	≈0.75
	P/S	180/0	var (↓)	≈0.25
#3	R	≈-90	≈55	var (↑)
	P/S	180/0	var (↓)	≈0.25-≈0.3
#4	P	163	30	0.27
	S	4	40	0.25

Table 5.3: *List of the parameters used in separating the Rayleigh wave present in Figs. 5.8 and 5.9. If two values are given separated by "/", then there were two distinct values for this parameter along the spread. If the actual values show some scatter, then a mean value is given indicated by "≈". "var" indicates that the actual values scattered widely. ↓ means that for this wave type values were generally lower than for the other wave type. ↑ is used in the opposite case.*

The reason why two iterations were necessary in order to remove most of the Rayleigh wave is due to the fact that it is dispersive. Fig. 5.13 shows the phase and slowness for the analysis window from trace 220 to 226. The Rayleigh wave covers frequencies from approximately 5 to 40 Hz. At around 25 Hz a phase wrap occurs, so the slowness computed directly from the phase values will not yield correct results. This is the reason why the slowness curve ends at 25 Hz. Arrows indicate the branches of the phase curve belonging to the Rayleigh wave. The removal of the Rayleigh wave was repeated using one fit to the dispersive slowness curve for all analysis windows. The residual data closely resemble that obtained after two iterations using a constant slowness each time.

Interestingly, the slowness decreases for higher frequencies indicating that there is a higher velocity near the surface than at depth. Together with the shingling we can interpret this result such that there is probably a low velocity near-surface layer of a certain thickness, underlain by a material with a high velocity. This combination produces the shingling. The depth to the base of the wave guide could be resolved from the mean phase and group velocities (Robertsson et al. (1996)). Underneath the high-velocity layer the velocity decreases as indicated by the dispersion curve. The abrupt ending of the smooth phase curve around 40 Hz (see Fig. 5.13) could also indicate that the higher frequency components of the Rayleigh-wave actually travel in the upper-most low-velocity layer.

The polarisation angle estimated for the Rayleigh wave is shown in Fig. 5.14. It shows a general decrease in value for increasing frequency which could indicate a decrease in Poisson's ratio for increasing frequency. This would mean that the velocity decrease with depth is larger for the S-wave than for the P-wave. For comparison, we computed the theoretical polarisation angle of a Rayleigh wave in a half-space for a variety of Poisson's

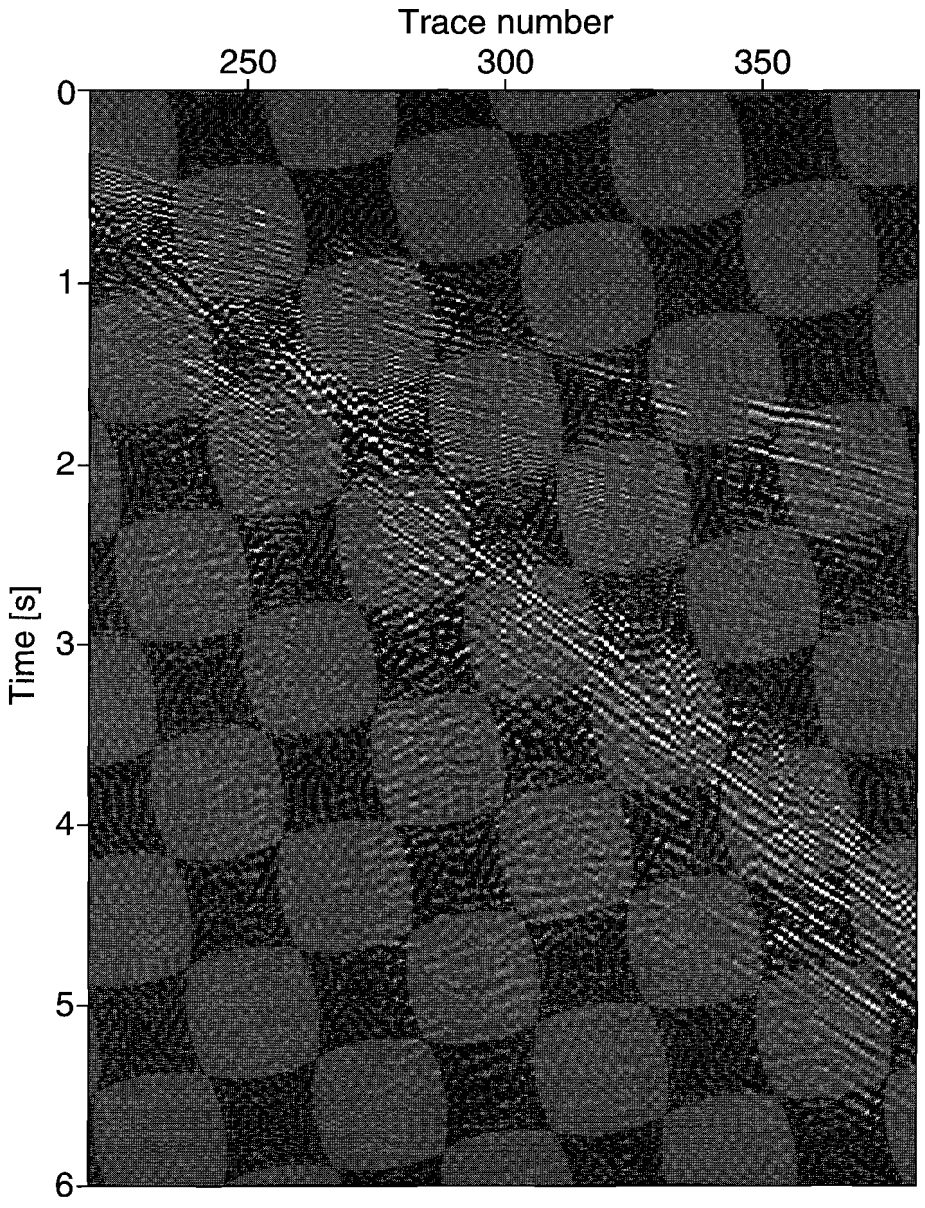

Figure 5.10: *Zz-component of the residual data set #1 after three iterations. Traces are scaled individually.*

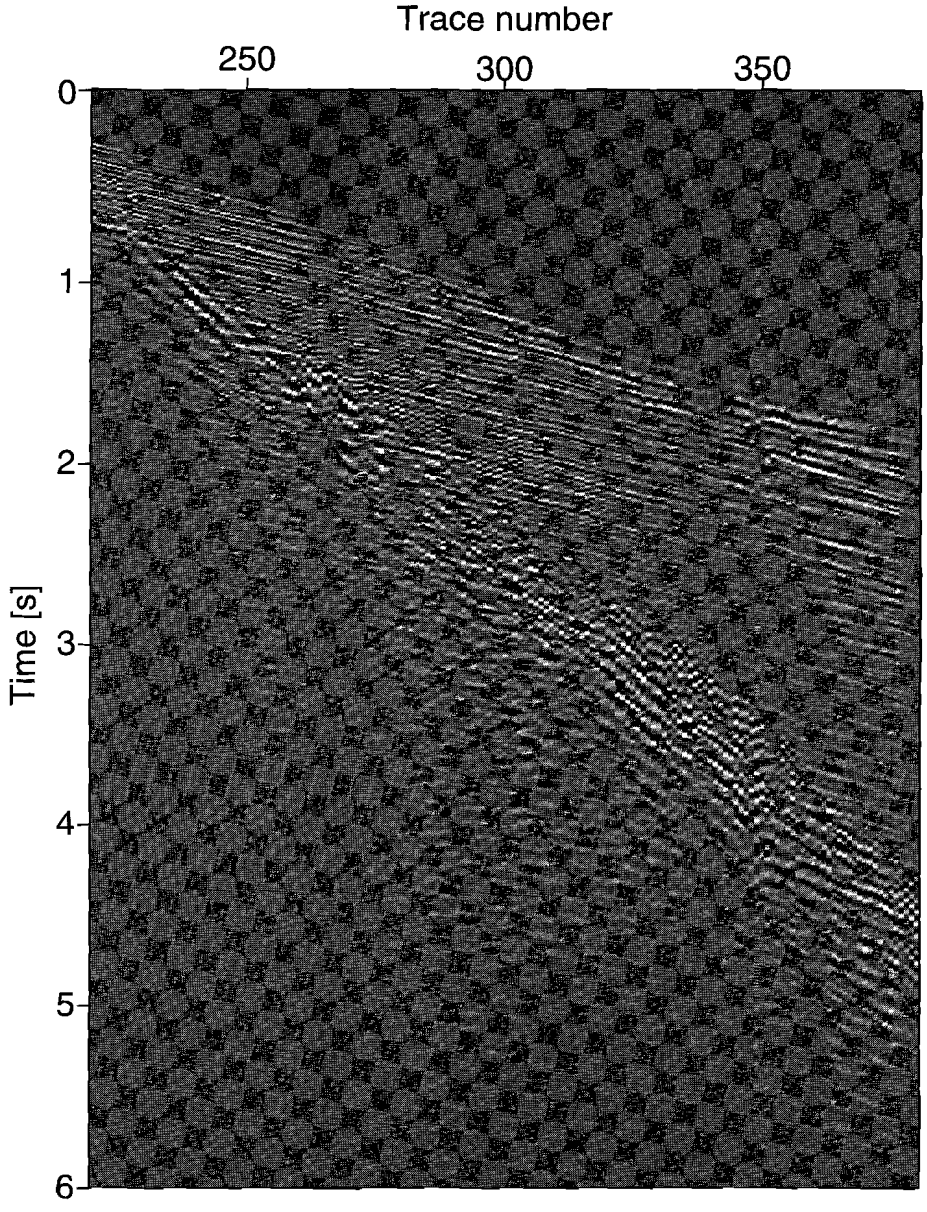

Figure 5.11: *Zx-component of the residual data set #1 after three iterations. Traces are scaled individually.*

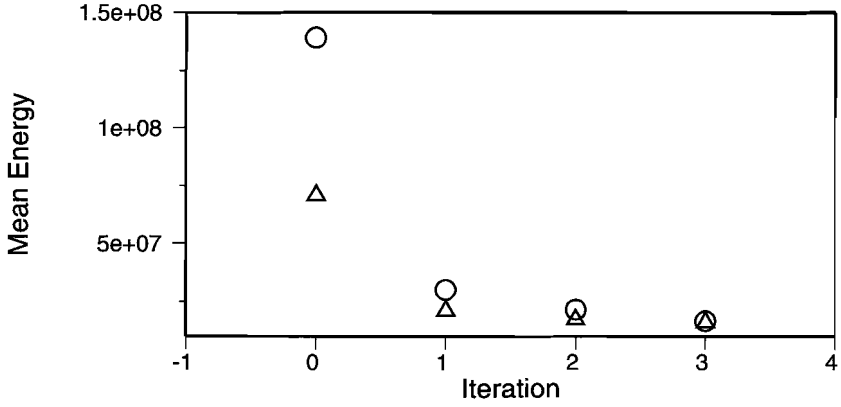

Figure 5.12: *Mean energy of Zz- (circles) and Zx-component of data set #1 for each iteration.*

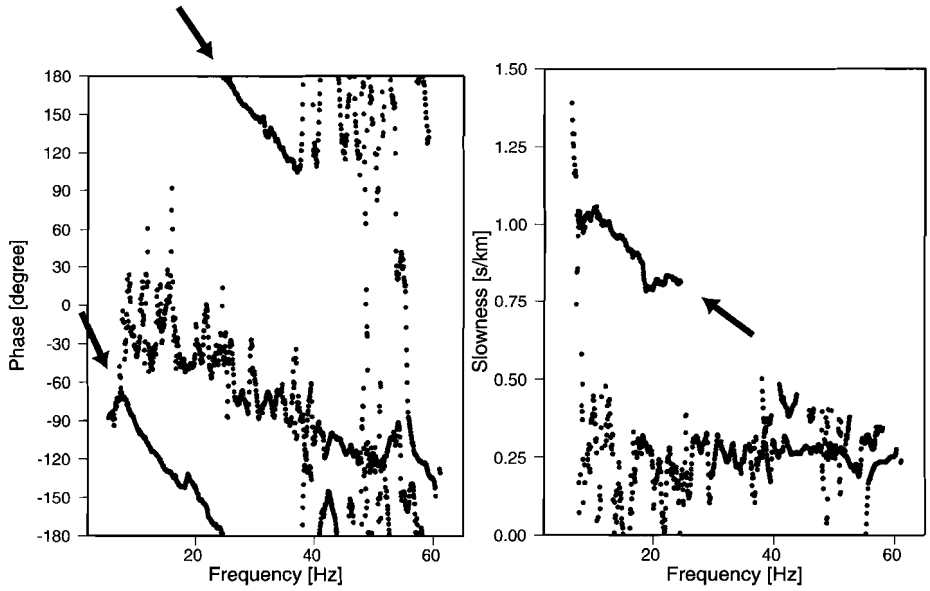

Figure 5.13: *Data set #1: Phase (left-hand side) and slowness (right-hand side) from the analysis of traces 220 to 226. The arrows indicate values belonging to the dispersive Rayleigh wave.*

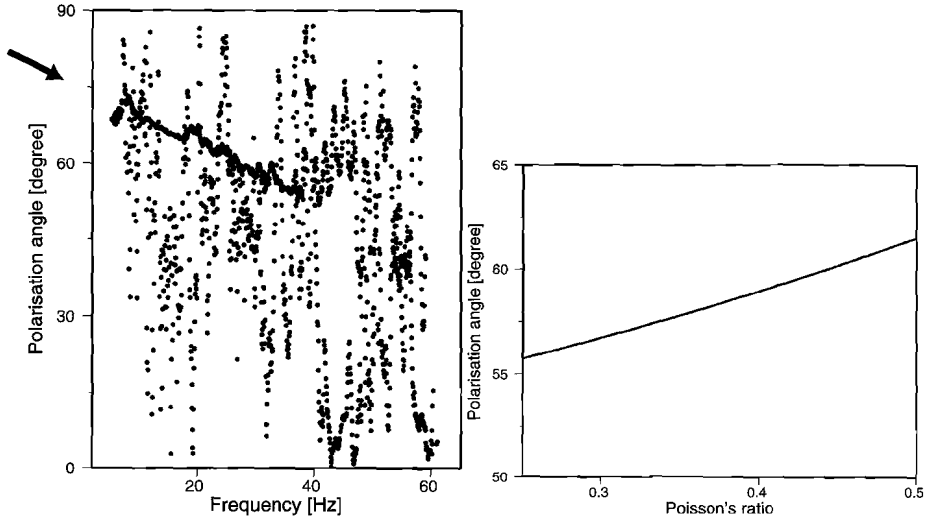

Figure 5.14: *Data set #1: Left-hand side: Frequency dependent polarisation angle from the analysis of traces 220 to 226. Right-hand side: Theoretical polarisation angle for Rayleigh wave in half-space for varying Poisson's ratios.*

ratios (see Appendix B). The result is shown in Fig. 5.14. We could theoretically obtain from the Rayleigh wave not only an S-wave velocity profile, but also a Poisson's ratio profile and, by combining the two parameters, the P-wave velocity profile.

5.4 Land dataset #2

The NAM provided us with a two-component shot gather recorded during a land seismic survey in the northern part of The Netherlands (near De Wijk). The vertical and inline-horizontal components are shown in Figs. 5.15 and 5.16, respectively. For some acquisition parameters see Table 5.4.

The most striking feature is the difference in events visible on the two components, e.g. the low-frequency event on the inline-horizontal component which arrives at around 3.75 s on trace 1 is completely absent on the vertical component (checked using AGC). The low-velocity ground roll is different too. The reflections on the inline-horizontal component are converted waves, while those on the vertical component are P-waves. In this area of The Netherlands, the poorly compacted low-velocity top-layer acts as a wavefield separator. It also is the reason for the statics, giving especially the converted waves an irregular appearance.

Although this data set is far from optimal for wavefield separation, the data window outlined in Figs. 5.15 and 5.16 was analysed. This window was chosen because the converted wave at the bottom of the window is also weakly visible on the vertical component. We

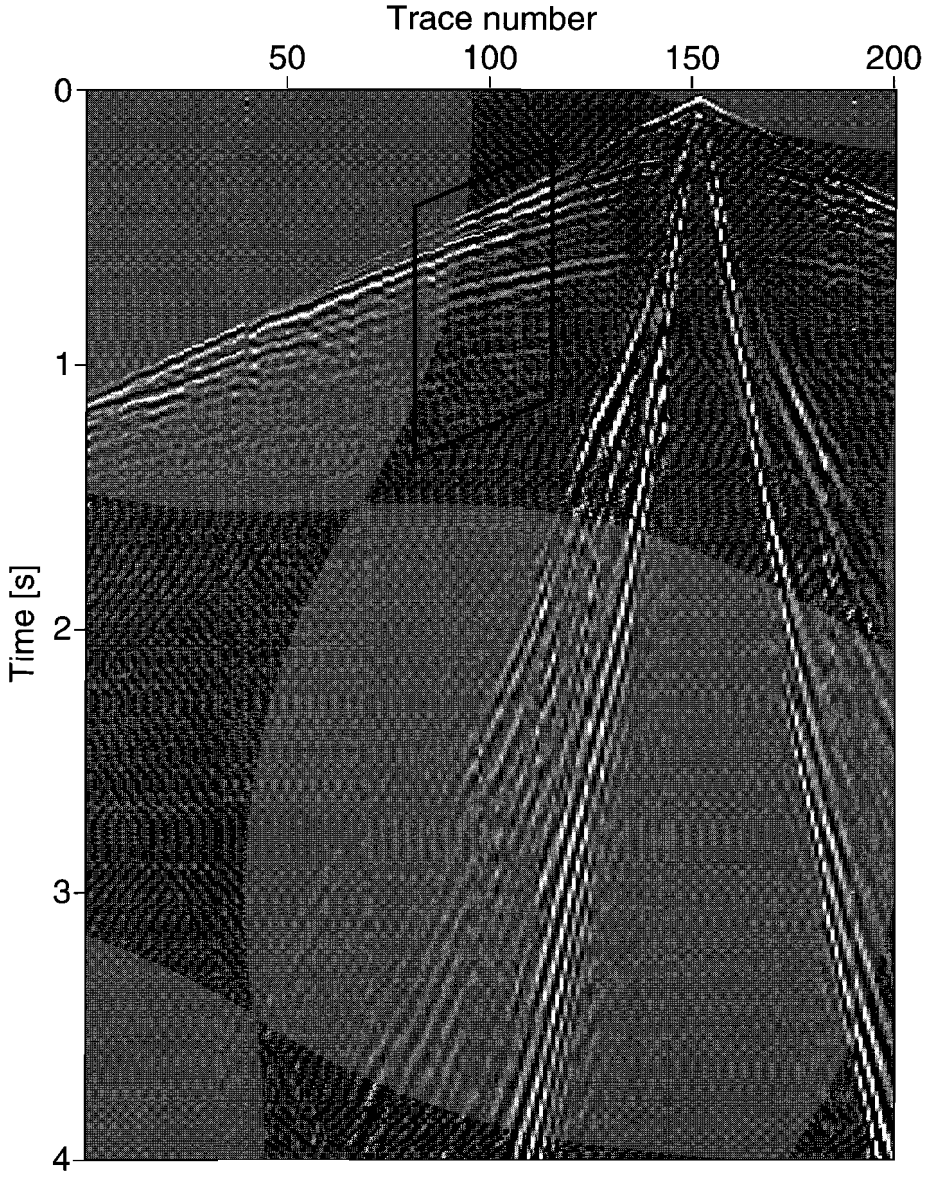

Figure 5.15: *Vertical component of data set #2. Traces are scaled individually.*

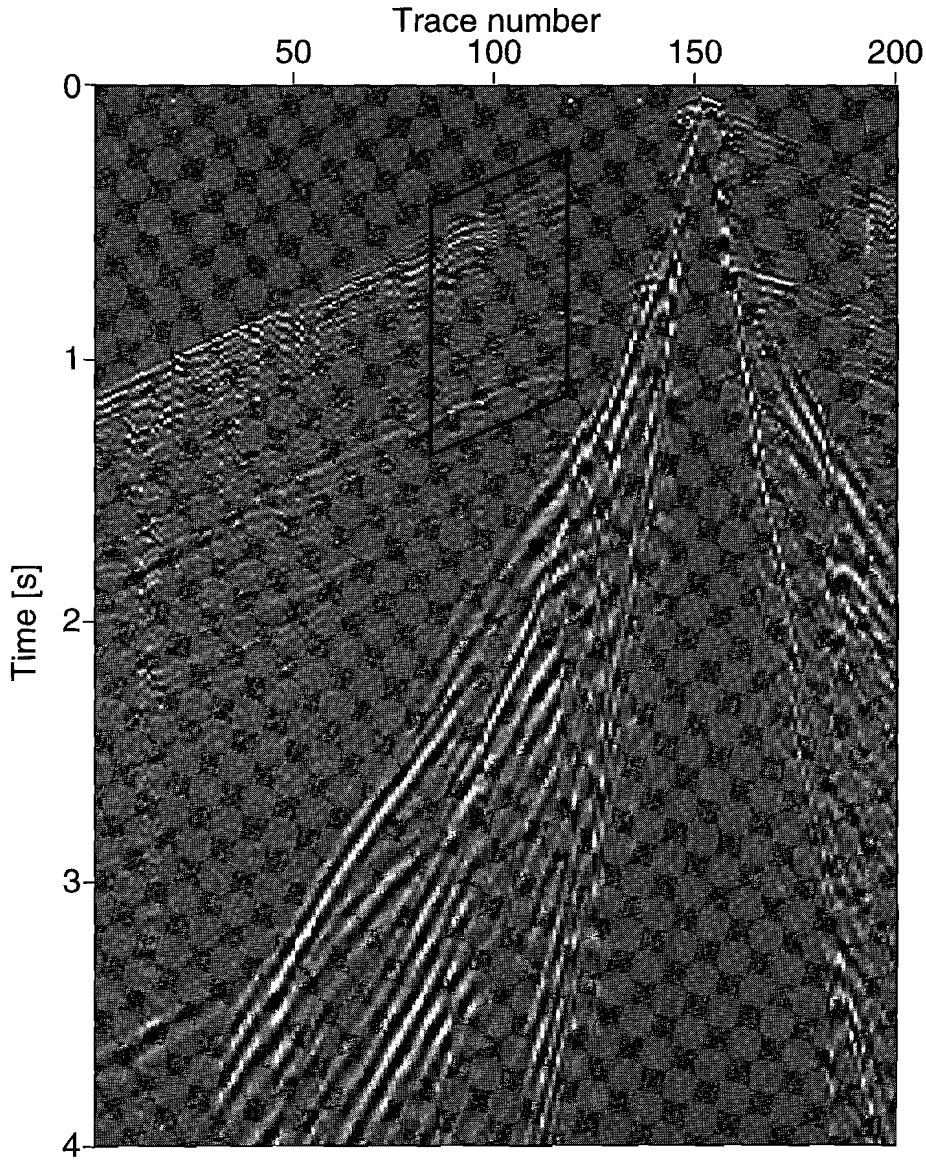

Figure 5.16: *Inline-horizontal component of data set #2. Traces are scaled individually.*

source	dynamite
source depth	5 m
source strength	500 g
shot interval	25 m
spread	split-spread
number of geophones	200
geophone type	single vertical and horizontal
receiver station interval	12.5 m
number of geophones in array	6

Table 5.4: *Acquisition parameters for the De Wijk data set*

attempted to estimate its parameters. Using 7 traces the analysis yielded the estimates shown in the left-hand side of Fig. 5.17. The phase difference (upper figure) indicates the presence of P- and S-wave energy having an apparent slowness of ≈ 0.5 s/km. The polarisation angle (middle figure) shows no clear preference.
The failure to estimate the characteristic parameters is most probably due to the statics, but coupling could have also played a role. For comparison, the right-hand side of Fig. 5.17 also shows the estimated values from one realisation of the synthetic test regarding statics in Section 4.2. P-wave statics were 2 ms, S-wave statics 20 ms, a ratio that resembles values for The Netherlands. The phase difference still shows some significant values that are coherent over a number of traces, but slowness and polarisation angle cannot be used for a reliable estimate.

5.5 Conclusions

By means of a realistic synthetic data set we were able to show that the method can be applied to data that contain reflections and diffractions which generally do not comply fully with the plane-wave assumption. Refractions, having linear move-outs, cause problems for the analysis of those traces that are recorded close to their onsets. The iterative approach proved useful for analysing data differing in amplitude.
Application of the method to industry data was only partly successful. It was possible to remove most of the Rayleigh wave present in data set #1. Further analysis of the frequency dependent slowness and polarisation curves has the possibility of retrieving not only S- but also P-wave velocity with depth from the Rayleigh wave. Lateral variations in the velocity profiles would be automatically mapped due to the moving analysis window approach.
Application of the wavefield separation method to data set #2 failed for several reasons. First of all there were considerable statics. Correcting these time shifts only makes sense if P- and S-waves, which are likely to have differing amounts of statics, do not overlap in time. The use of single component receivers instead of orthogonal three-component receivers carries the risk of further disturbing the polarisation information due to different

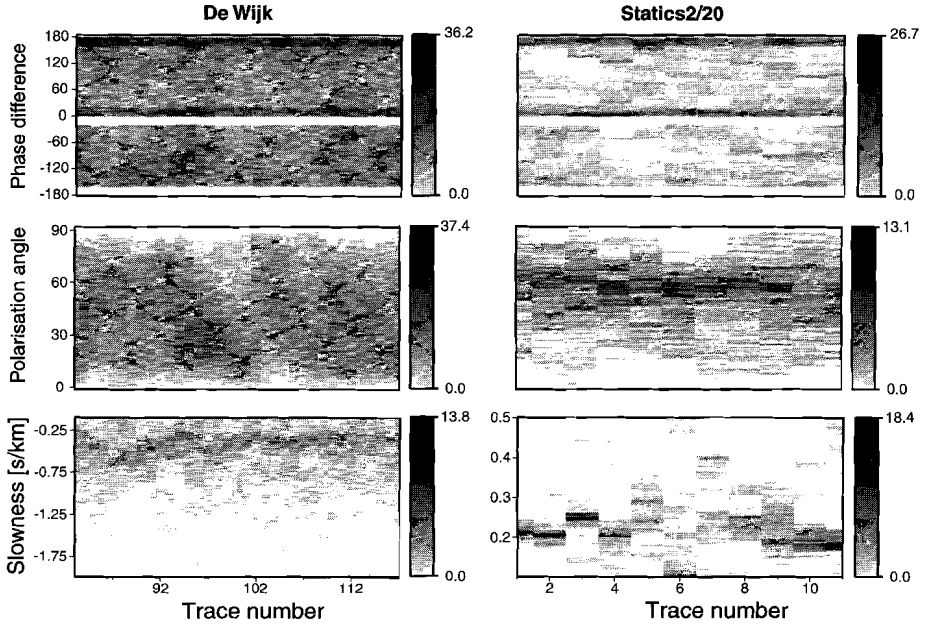

Figure 5.17: *Histograms for all analysis windows for the phase difference (upper figure), polarisation angle (middle figure) and slowness (lower figure) from the analysis of the data window outlined in Figs. 5.15 and 5.16 (left-hand side) and from the analysis of synthetic data used in Section 4.2 (right-hand side).*

coupling of the receiver components. Coupling differences between adjacent (orthogonal) receivers will hamper the analysis and can only be partly corrected for by trace balancing. There is also little difference in move-out between events which might have further complicated the analysis. Last but not least, P- and S-wave events were already well separated on the recorded data due to a low velocity layer at the surface. From the view point of applying this method, this is a slight disadvantage since the method in general works better if wave energy is mapped on both receiver components. Since the application of the method to this data is problematic anyway, this wave separation due to geology can be considered an advantage.

Chapter 6

MULTI-COMPONENT HIGH-RESOLUTION SEISMIC PROFILING

6.1 Introduction

The application of reflection seismics for characterising the shallow sub-surface has become an ever-increasing research area over the last decades. Steeples et al. (1997) give a summary of a research workshop analysing the potentials and limitations of near-surface seismic reflection methods. A more detailed characterisation of the near surface will e.g. help hydrologists in delineating migration pathways of contaminants at a polluted site; assist civil engineers in anticipating the response of the soil to building activities; assess earthquake hazards by identifying active faults; detect changes in ground properties or even voids and cavities during tunnel drilling (e.g. Kneib et al. (1999)). Environmental and geotechnical engineering rely more and more on seismic images of the sub-surface, but not all of the questions can be answered due to lack of seismic contrast, insufficient resolution, or the difficulty in translating dynamic parameters into static ones. Reflection seismics, despite its potential to continuously map an area, is also considered to be time consuming and expensive. Novel approaches to reduce time and costs have been reported (e.g. van der Veen et al. (1999)). A characterisation of the shallow sub-surface is also important for the oil- and gas-industry because all seismic energy has to travel through this poorly compacted region. Lateral variations in thickness and changes in wave velocity lead to variations in arrival time which have to be corrected.
The equipment has evolved from that used in routine seismic surveys: geophones have natural frequencies typically from 30 Hz upwards to attenuate low-frequency ground roll and to guarantee the recording of high-frequency reflections (up to 400 Hz at favourable sites); small sources like weight drops or shotguns are mainly used which are capable of emitting high-frequency signals (for a detailed comparison of shallow seismic sources see e.g. Miller et al. (1986)); recording systems have display option or even pre-processing software built in, but often the number of recording channels is small.
High-resolution seismics usually utilises only P-waves recorded by vertical receivers. Shear waves, however, have the potential to overcome some of the shortcomings of P-waves for shallow site investigations:

- If excited in the same frequency range by use of vibratory sources for example, S-waves exceed P-waves in resolution, because S-wave velocities are smaller than P-wave velocities and therefore S-wavelengths shorter than P-wavelengths. The higher attenuation of shear wave, as compared to that for P-waves, however limits the resolution of the shear waves as well as the depth from which S-wave informa-

tion can be retrieved.

- The matrix of uncompacted material often has a lower velocity than water. Since P-wave velocity depends not only on lithology, but, among others, also on porosity, fluid type and saturation, the presence of water will dominate the P-wave velocity. For the water-saturated material it is then difficult to obtain lithological information (from VSP measurements) and P-wave contrasts also might be limited. The S-wave velocity depends only on the rigidity and bulk density of the material and imaging of the water-saturated zone with S-waves therefore can yield a more detailed image of the sub-surface and lithological information.
- Since S-wave velocity and dynamic shear modulus are directly related, soil properties can be deduced from shear wave data. Still, the link between dynamic and static properties, which are more important for engineering purposes, is only established through empiric formulas.
- It can be of further importance to detect and quantify seismic anisotropy in the subsurface. Shear waves that have split upon entering an anisotropic medium are then analysed.

Research has concentrated on using SH-waves, which can easily be excited using horizontal impulse or vibratory sources. Similar to P-wave surveys only one receiver component is recorded (crossline-horizontal). This makes high-resolution SH-wave profiling as fast as P-wave profiling with the advantage of looking at material properties directly.
The need for an analysis of the shallow sub-surface using full-elastic wave propagation stems from the fact that all wavefield components contain parts of the jigsaw puzzle. All pieces will finally together form the image that can be derived from reflection seismics. This means that a combined or joint inversion of all possible wave types, P-waves, S-waves, converted waves, and surface waves, should be attempted. Multi-component (high-resolution) profiling comes along with an increase in necessary equipment (special sources and receivers, recording machines with more channels) as well as a decrease in acquisition speed, though.
In Chapters 3 and 4, the application of the wavefield separation method to various synthetic data sets were presented. In Chapter 5 it was shown that application of the method to industry data can be difficult due to geological implications or even impossible if the data do not comply with the plane wave assumption. In this chapter it is demonstrated that the method can be applied to shallow data successfully. First, we describe the equipment used, then we discuss the data obtained at three different sites in The Netherlands and apply the method to selected records. In summary, the application of the wavefield separation method on two-component data was generally successful. Besides separating the (dispersive) Rayleigh wave from the data, we were able to extract a number of coherent arrivals from one data set using the iterative approach extensively. Three-component wavefield separation was applied successfully only for extraction of the Rayleigh wave. Further analysis did not result in coherent parameter estimates. This can be attributed to the fact that events recorded on the vertical and inline-horizontal components were only weakly present on the crossline-horizontal component and vice versa.

6.2 Equipment

6.2.1 Sources

The radiation pattern of a seismic source depends on the force it applies to the sub-surface, its geometry, the Poisson's ratio of the surrounding material, inhomogeneities surrounding the source, which include the free surface, and attenuation. Source design aims at increasing the output of one wave-type and decreasing that of the others. Surface waves, for example, are attenuated as a consequence of source burial. Since a multi-component survey attempts to gather information about the sub-surface by using different wave-types a source should ideally radiate those wave-types with equal strength. A solution is the application of different sources each tailored to the emission of one wave-type, or, two or more sources of the same type operated in a special configuration. An example for this second option is e.g. Dankbaar (1983), who showed theoretically that by operating two P-wave vibrators in counterphase SV-wave energy emitted in the vertical direction is enhanced. This effect is, however, frequency dependent.
Several sources, both impulsive and vibratory, are available for shallow multi-component surveying. The sources used in the three case studies are shown in Fig. 6.1 and described below.

1. **P-wave vibrator** (see Fig. 6.1a): This electro-magnetic mini-vibrator was developed at Utrecht University (Nijhof (1989)). It has a reaction mass weight of 65 kg and a baseplate weight of 3.5 kg and exerts a vertical force on the ground. The duration, bandwidth and type of the sweep (up or down, linear or non-linear) can be tailored to the objectives of the survey. In principle, frequencies above 1 kHz can be emitted, but the upper frequency is typically chosen to be around 500 Hz because higher frequencies are attenuated too rapidly. The recorded seismogram (vibrogram) has to be converted into a record that resembles the data obtained from an impulsive source. Usually, the vibrogram is correlated with a reference signal that contains no information about the sub-surface. This signal should be the far-field velocity of the source, which is in the industry approximated by the pilot sweep. A better estimate is time-derivative of the ground force which in theory is proportional to the far-field velocity. Since it is not feasible to place load cells underneath the baseplate to directly measure the ground force, the weighted sum method (Sallas (1984)) is usually taken as approximation:

$$-F_G = m_B \frac{\partial^2 u_B}{\partial t^2} + m_R \frac{\partial^2 u_R}{\partial t^2}. \tag{6.1}$$

   Here F_G is the ground force, m_B and m_R are the masses of the baseplate and reaction mass, respectively, $\frac{\partial^2 u_B}{\partial t^2}$ and $\frac{\partial^2 u_R}{\partial t^2}$ are the accelerations measured by accelerometers at the baseplate and reaction mass, respectively.

2. **S-wave vibrator** (see Fig. 6.1b): This source was developed by OYO-CAG, Nieuwegein (Ghose et al. (1996)). It is basically a tilted version of the P-vibrator

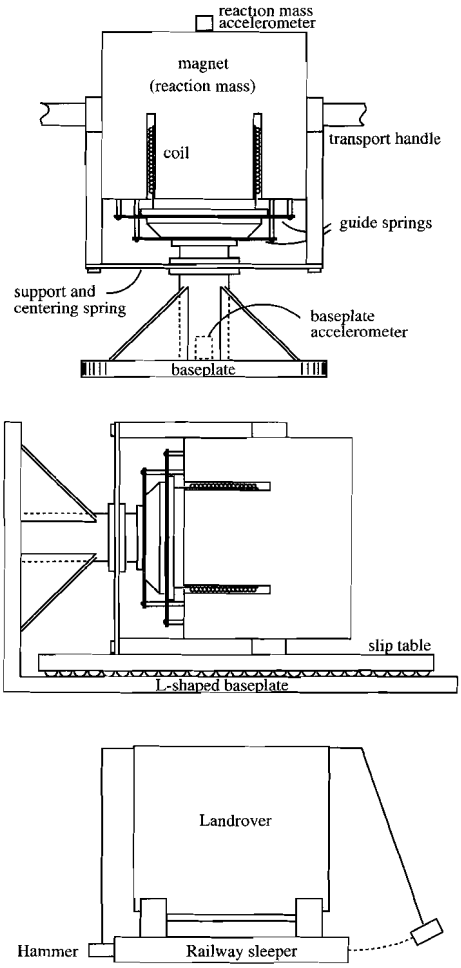

Figure 6.1: *a: Portable electro-magnetic P-vibrator. b: Schematic view of the S-wave vibrator, which is basically a tilted version of the P-wave vibrator. Note that some components have been altered to accommodate the new horizontal position (not indicated in the figure). c: Railway sleeper (wooden beam), anchored to the ground by a weight (usually the acquisition vehicle). The signal is produced by hitting a hammer onto the head sides.*

(see Fig. 6.1b). The reaction mass weight is now 72 kg and the baseplate weight 29 kg. This vibrator is able to send out frequencies between 5 and 500 Hz. Brouwer and Helbig (1998) indicate that the weighted sum method (Eq. 6.1) is valid for this vibrator only for such frequencies where the reaction mass and the baseplate behave rigidly. They show that the ground force can be well estimated up to 400 Hz by using more than the usual two accelerometers.

3. **Railway sleeper** (see Fig. 6.1c): This source consists of a wooden beam anchored to the ground by a weight to prevent slipping. The beam is hit on its head sides by metal hammers. The source is normally operated perpendicular to the receiver spread and radiates then mainly SH-type waves in the direction of the spread. P-wave energy is also radiated which can be attenuated on the recorded data by subtracting records coming from opposite strikes. SH-waves, having opposite polarity will add while P-wave having the same polarity on the two records will cancel. For perfect performance, both (opposite) strikes have to be of equal strength and the beam should be prevented from slipping.

6.2.2 Receivers

Orthogonal single three-component geophones with a natural frequency of 4.5 Hz (inside a casing) are used. The casing has three metal spikes and a water level on its top. The internal coordinate system was inferred by tapping the geophone and observing the sign of the resulting onset: the positive z-axis points down and the positive x-axis points in reverse direction to the arrow on the casing. Together with the y-axis this forms a left-handed coordinate system. To comply with the coordinate system used in this thesis (positive inline-horizontal direction away from the source, see for example Fig. 2.1), the geophones must be planted with the arrow pointing toward the source. A sketch of the geophone is given in Fig. 4.6.

6.2.3 Recording equipment

We use a modified BISON Spectra (called Spectraleo) seismograph with 48 recording and 4 auxiliary channels. A connection box was built to be used between the recording cable and the recording machine for grouping the receiver components together. This helps the quality control during field measurements.

6.3 Case studies

The purpose of collecting data was three-fold: to gain experience with and test the equipment, to find suitable locations for further research which will aim at actually characterising the shallow sub-surface by using the full elastic wavefield, and to obtain data that can be used in the present study of wavefield separation. In total, 3 surveys were conducted (see Fig. 6.2) and additional tests inside the institute and at a location nearby the

Figure 6.2: *Survey locations in the Netherlands.*

institute were carried out. The latter helped to define the internal coordinate system of the geophones, find a descaling factor missing in the trace headers of the files stored by the Spectraleo, and test the response of the geophones to tilting and changes in coupling (see Chapter 4). The descaling factor is needed to reconstruct the original voltage recorded by each geophone from the stored (integer) amplitude values.

6.3.1 Nieuwegein: 9-component CMP-survey

1. **Settings and targets:** This survey, carried out in January 1997 on a grassland in the industrial area of Nieuwegein, was conducted to record a 9-component data set using both P- and S-vibrators. Various measurements had already been carried out on this site resulting in a fairly good knowledge of the sub-surface including the lithology which was interpreted from Cone Penetration Test (CPT) measurements (see Fig. 6.5b). The lithology is typical for this area of The Netherlands dominated by fluvial deposits. The peat layer, together with a shallow ground water table, is the main reason why P-wave surveying in this area is not successful. A shear wave VSP recorded at the location (see Fig. 6.5a) shows clear variations in velocity due to for example the peat layer and the Holocene/Pleistocene sand interface. An SH-wave reflection survey shot earlier at this location shows signals mainly from the peat layer and the Holocene/Pleistocene sand interface (see Brouwer et al. (1996) and Brouwer et al. (1997)). They observed additional intrabed reflections resulting from sand lenses of varying rigidity.

   It was planned to confirm and complement the information gained from the previously recorded Yy-section by means of a 9-component CMP survey. The new spread was measured perpendicular to the old survey shot parallel to the company

building of OYO-CAG. In total, 11 shots were recorded, the last two with static spread and only the sources moving (due to lack of appropriate extension cables). For acquisition parameters see Table 6.1. To have enough offset for recording the interface between Holocene and Pleistocene sand properly with a geophone interval of 0.5 m the number of recording channels was doubled by using the DAS-1 from OYO-CAG alongside the Spectraleo.

source	P- and S-vibrator
number of shots	11
sweep type	linear up-sweep
sweep frequencies	20 - 500 Hz
sweep length	7500 ms
vertical stacks	8
shot distance	0.5 m
number of geophones	32
inline offset (shot #1 to #9)	3 m
geophone distance	0.5 m
nominal fold	11

Table 6.1: *Acquisition parameters for the Nieuwegein survey.*

2. **Results:**

Fig. 6.3 displays the high-cut filtered data in matrix form for shot #11. The mean amplitude differs greatly between the components and is not symmetric if source and receiver components are interchanged. While for example the Zx-component has 46 % of the mean amplitude of the Zz-component, the Xz-component has 72 %. This asymmetry is caused by the strong Rayleigh-wave energy triggered by the source, which results in higher amplitudes on the z- compared to the x-component. The Xx-component has as much energy compared to the Xz-component as the Zx-component compared to the Zz-component: 46 %. This correspondence is found however for only 4 out of the 11 shots indicating a fundamental difference between P- and S-wave vibrator. The difference becomes clearer when we compare the mean amplitude recorded at the same receiver component for the three source directions (see Table 6.3). The coupling for the P-wave vibrator and therefore the energy it transmits into the sub-surface is approximately the same for shots #4 through #9 (concluded from the mean amplitudes). Therefore, we scale the energy of the S-wave vibrator according to the Zz-component recordings. There is substantial scatter in the values for the 6 shot locations for both, the Xz- as well as the Yz-component. This difference in consistency between shot locations for the P- and S-wave vibrator could be contributed to the difference in baseplate size. The baseplate of the S-wave vibrator is much larger than that of the P-wave vibrator. The coupling will therefore also depend on whether the whole baseplate is in contact with ground or only a part. The variation between Xz- and Yz-components could

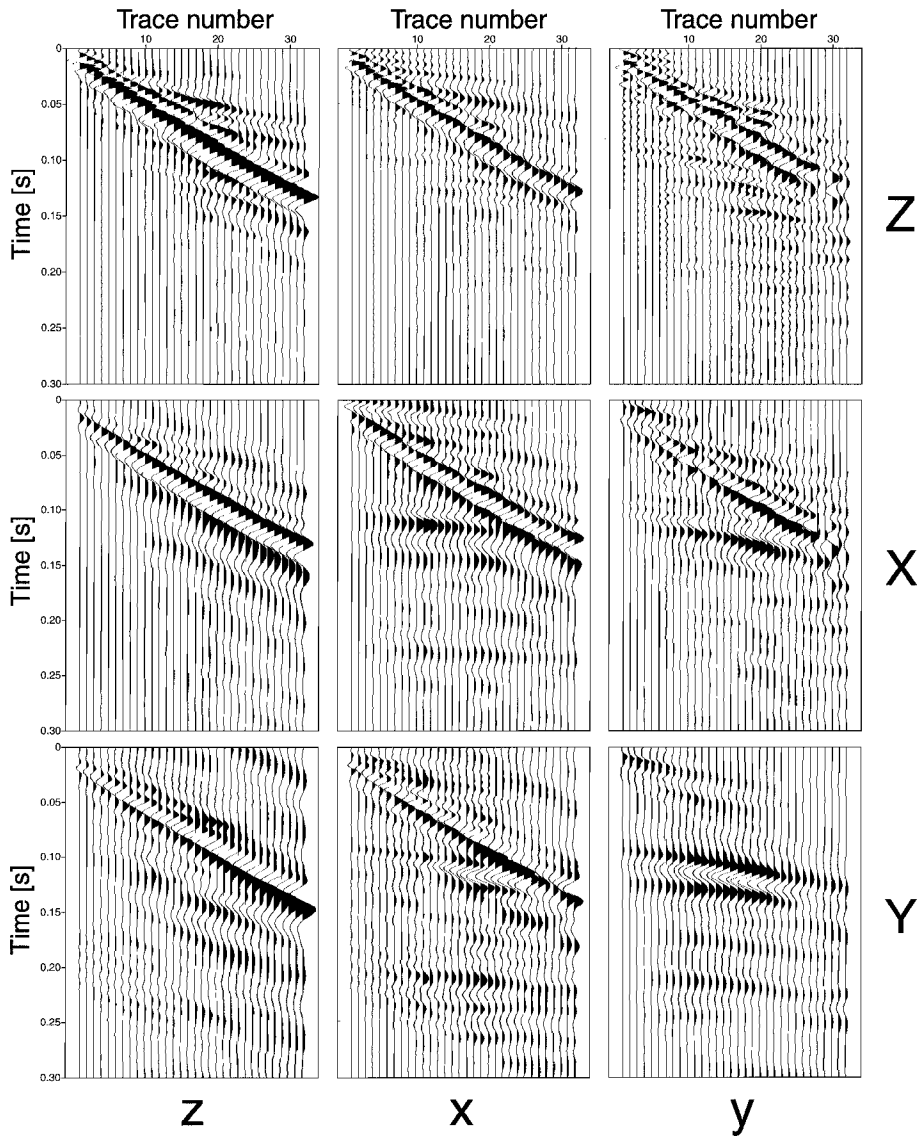

Figure 6.3: *Data matrix for shot #11 from the Nieuwegein data set. The upper and lower case letters indicate source and receiver directions, respectively. Each trace is balanced relative to the maximum amplitude found on the Zz-panel. The global mean amplitude values differ widely (see Table 6.2). Therefore, each panel has its own global scaling. The data have been high-cut filtered (cut-off at 170 Hz) to suppress spurious events.*

also be explained by a difference in coupling, since the S-wave vibrator had to be rotated by 90° between the two source orientations. Note, that even the S-wave vibrator operating in the crossline direction gives rise to a Rayleigh wave (see components Yz and Yx in Fig. 6.3).

In most of the panels of Fig. 6.3 a clear reflection is visible at 100 ms two-way traveltime for the shortest offset. Using the velocity profile from the VSP-survey this event can be identified as an S-wave reflection from the peat layer. At around 200 ms the S-wave reflection from the Holocene/Pleistocene sand interface arrives. There are more reflections masked by the Rayleigh-wave arrival.

	z	x	y
Z	100 %	46 %	31 %
X	72 %	33 %	21 %
Y	18 %	7 %	14 %

Table 6.2: *Mean amplitudes for the different components of the Nieuwegein survey (shot #11)*

shot number	Xz	Yz	Xz/Yz
4	59 %	38 %	1.55
5	66 %	10 %	6.60
6	38 %	44 %	0.86
7	30 %	16 %	1.86
8	71 %	59 %	1.20
9	35 %	14 %	2.50

Table 6.3: *Nieuwegein survey: Variation of the mean amplitudes with shot position on Xz- and Yz-component (scaled relative to the value on the Zz-component) and the ratio of the two components.*

The Yy-components of all the 11 shots show no clear Love wave arrival. The absence cannot be related to a high velocity top-layer at this location. A raw Yy-stack was produced using a velocity profile derived from fitting hyperbolas to the CMP-sorted data. As an example, CMP #30 before and after normal move-out (NMO) correction is shown in Fig. 6.4. The laterally varying velocity profiles are listed in Table 6.4. Generally, the deeper events (beneath the peat-layer reflection) show hardly any move-out on the CMP-panels which makes them stack for a broad range of velocities. No attempt has been made to improve the stack by applying static corrections or deconvolution.

The stack was then converted to the depth section shown in Fig. 6.5c. The peat layer is at a depth of less than 10 m on the left-hand side and dips slightly toward the right.

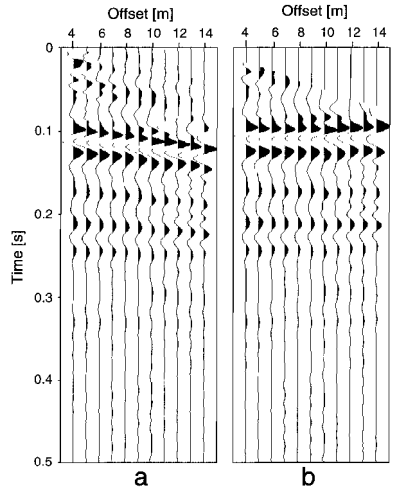

Figure 6.4: *CMP #30 from the Nieuwegein data: a: Before NMO correction. b: After correction using the velocity profile listed in Table 6.4.*

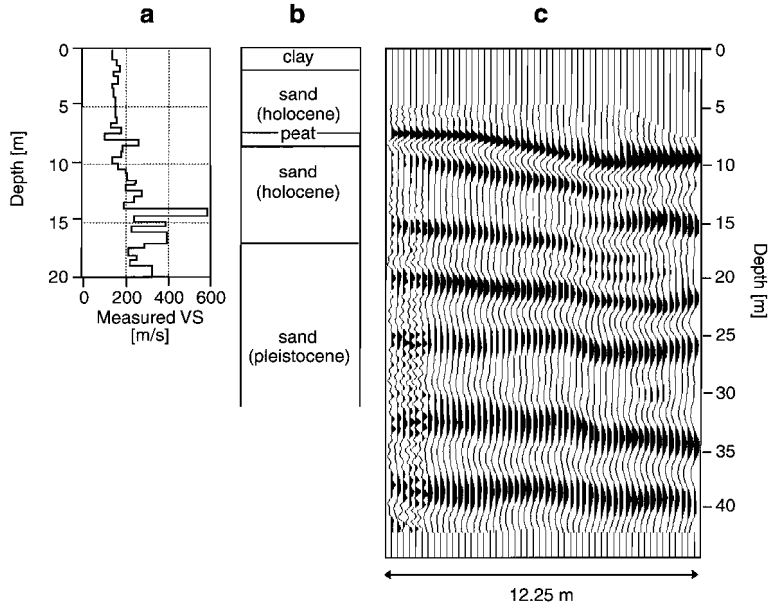

Figure 6.5: *Nieuwegein survey: a: S-wave interval velocity derived from VSP experiment. b: Lithology derived from CPT-measurement. c: Depth converted Yy-component stack with AGC applied (window length of 10 m). Figs. 6.5a and b were adapted from Brouwer et al. (1997).*

CMP location	7	20	25	30	35	40
TWT [ms]	stacking velocity [m/s]					
0	130	140	140	140	140	140
80	150	160	170	180	190	200
200	200	200	200	200	200	200
500	300	300	300	300	300	300

Table 6.4: *Nieuwegein survey: Laterally varying stacking velocities used for Yy-component stack and depth conversion. TWT stands for two-way travel time (at shortest offset).*

The change from Holocene to Pleistocene sands can be found at a depth of less than 20 m. Two recent CPT-tests also indicate that the peat layer is slightly dipping and that the sand interface stays at the same depth. There are two more reflections visible underneath, but the VSP as well as the CPT-profile are too shallow to give an indication where these events might be coming from.

3. **Evaluation:** This site has the advantage that much information about the shallow sub-surface is already available. The main energy on the vertical and inline-horizontal components travels as a Rayleigh wave. Surprisingly, the Love wave is absent on the cross-line component. In contrast to the results from SH-wave profiling, information from P-wave reflections can hardly be obtained.

6.3.2 Grevelingen: 9-component noise spread on the intertidal shoal 'Oude Tonge'

1. **Settings and targets:** Two decades ago, Utrecht University started investigating the possibility to obtain sedimentological information from tidal areas. The P-wave surveys provided excellent data since a weathering layer is absent. The area under investigation consists of water-saturated sands with some admixing of clay and peat. Holocene sediments deposited in a marine environment are underlain by Pleistocene sediments accumulated in aeolian, fluviatile and marine environments. Each lithostratigraphic unit has an internal structure that can give rise to reflections. For a summary on the results gained from many experiments conducted at the Grevelingen dam site (P-wave stacks and seismic facies interpretation) see Doornenbal and Helbig (1983) or Jongerius and Helbig (1988).

   We wanted to record a 9-component noise spread at the same location to see how much S-wave energy could be transferred into the water saturated sediments and whether the numerous P-wave reflections have S-wave equivalents. In April 1997 we laid out a noise spread during low tide on the intertidal shoal called 'Oude Tonge' near Bruinisse, The Netherlands. The location is situated south of the east-west running Grevelingen dam, connecting the two islands Goeree-Overflakke and

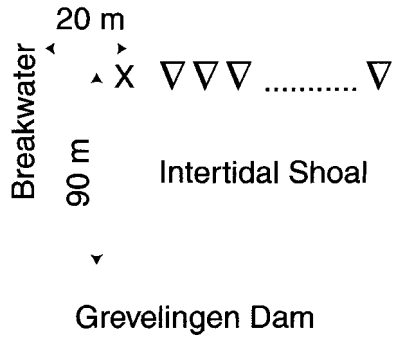

Figure 6.6: *A sketch of the Grevelingen survey location.*

Schouwen-Duiveland. We measured parallel to the dam at a distance of about 90 m, starting approximately 20 m south of the second breakwater (see Fig. 6.6). The acquisition parameters are listed in Table 6.5.

source	P- and S-vibrator
sweep type	linear up-sweep
sweep frequencies	50 - 500 Hz
sweep length	7500 ms
vertical stacks	4
shot distance	0.5 m
number of geophones	16
spread shifted	4 times
minimum offset	4 m
maximum offset	35.5 m
geophone distance	0.5 m

Table 6.5: *Acquisition parameters for the Grevelingen survey.*

2. **Results:**

Fig. 6.7 displays all components of the noise spread. Each trace is scaled individually for display purposes, so Table 6.6 has to be consulted in order to compare the mean amplitudes. The S-wave vibrator transferred more energy into the sub-surface than did the P-wave vibrator. Love waves (visible on the y-components) are excited by both vibrators, but are strongest on the Yy-component. There are hardly any other events visible apart from the dispersive surface waves.

The data of all components in Fig. 6.7 is dominated by surface wave arrivals. The Zz-component in this plot reveals some high-frequency events before the surface waves. Plotting this component with AGC shows that there are many events with

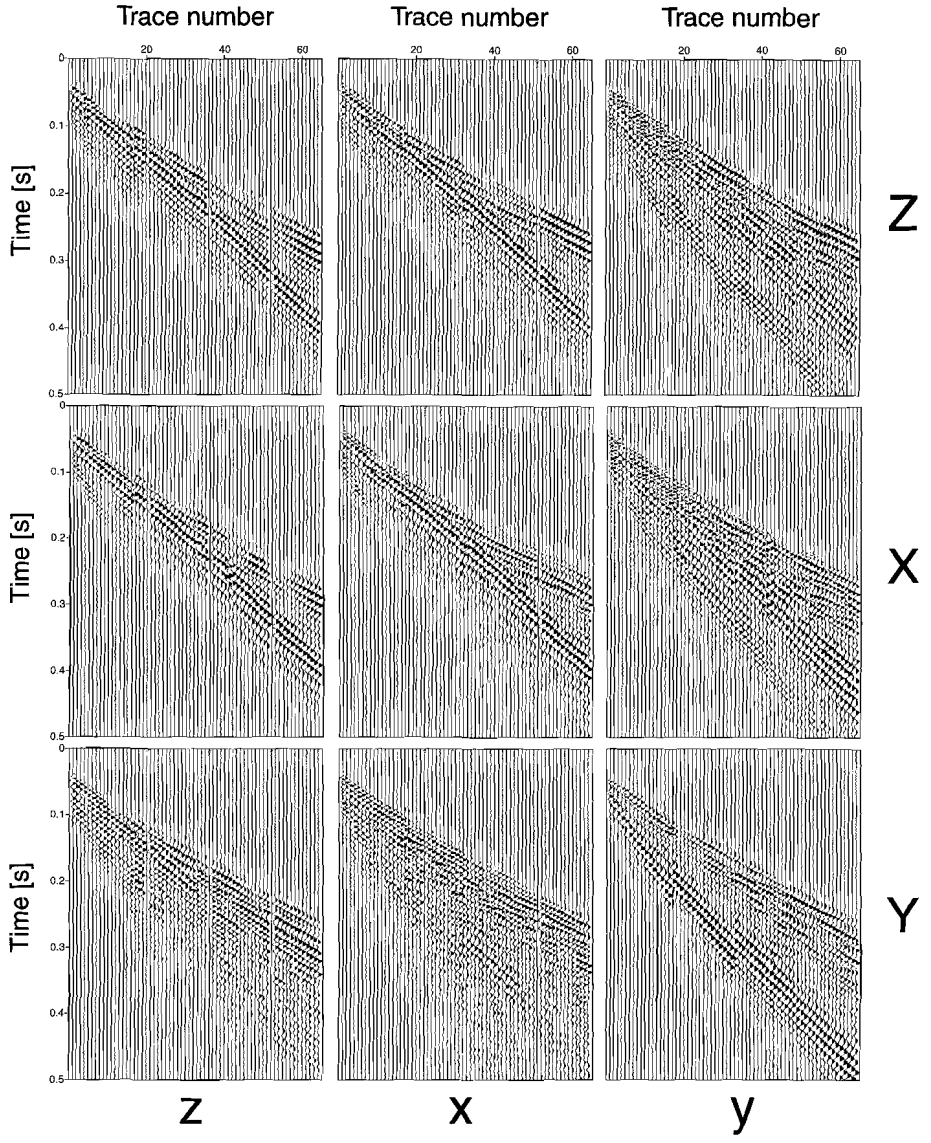

Figure 6.7: *Raw noise spreads from the Grevelingen survey. Each trace has been scaled individually.*

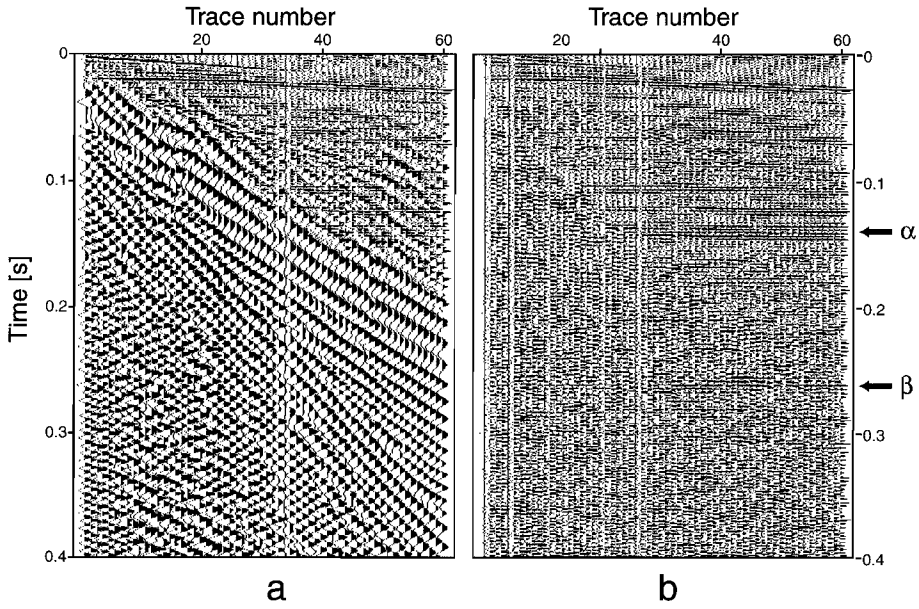

Figure 6.8: *Grevelingen noise spread: a: AGC-filtered record of Zz-component, window length 25 ms. b: AGC-filtered bandpassed record, corner frequencies for filter: 250,300,500,550 Hz, window length 25 ms. Events 'α' and 'β' are described in the text.*

little move-out (see Fig. 6.8a). If this very same component is bandpass filtered (see Fig. 6.8b) we see the reflections emerging from underneath the surface waves: e.g. the reflection labelled 'α' continues over more traces than in Fig. 6.8a, reflection 'β' becomes visible. This is possible since the surface waves have less higher frequency energy. The wavelet of the reflections, missing the lower frequency components, becomes ringy in this procedure which means loss of resolution.

Displaying the Zx-component in Fig. 6.9 in the same way as the Zz-component in Fig. 6.8, shows the differences in reflection signal between both components. The reflections seem to have less high-frequency content, are less numerous and event 'β' is not visible in the bandpass filtered record. S-wave reflections, due to stronger attenuation, should have lower frequencies compared to P-wave reflections. The reflection energy we see on the Zx-component is mainly due to non-vertical P-wave reflections. The mean energy of the bandpass filtered Zx-data, using a bottom mute which starts at 0 ms on trace #1 and ends at 100 ms on trace #60, is only 40 % of that of the Zz-data to have a fair comparison.

Repeating this analysis with the other components revealed no possible S-wave reflections on the x-components, but weak coherent energy on the Xy- and Yy-components: one reflection at 350 ms, and probable other reflections coming in later. Since they are on the y-component, they could also be side-scattered direct P-

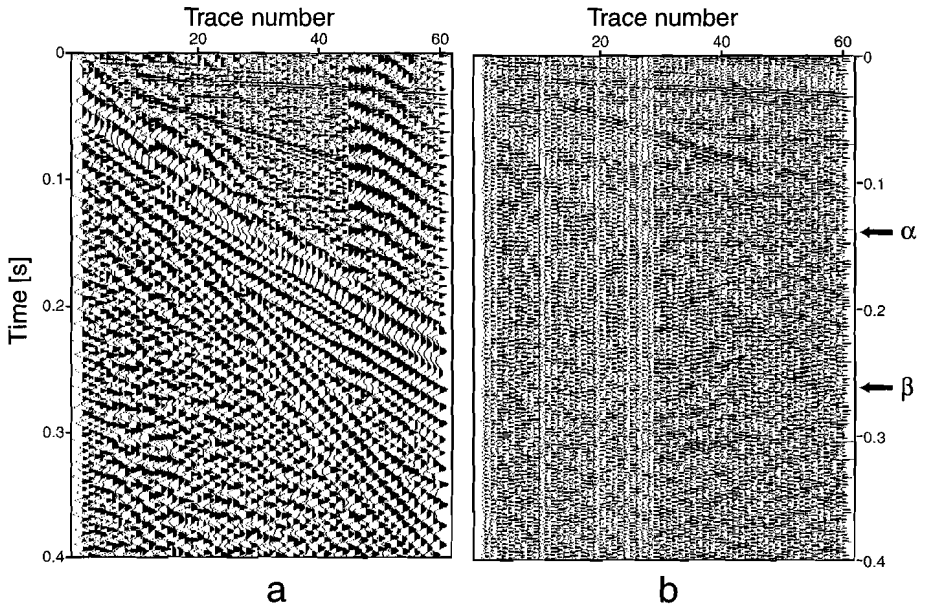

Figure 6.9: *Grevelingen noise spread: a: AGC-filtered record of Zx-component, window length 25 ms. b: AGC-filtered bandpassed record, corner frequencies for filter: 250,300,500,550 Hz, window length 25 ms. Events 'α' and 'β' are described in the text.*

wave energy from the dam. This energy, however, should arrive at the first receiver already at about 140 ms. The 350 ms event is also visible on the Yz-component.

	z	x	y
Z	55 %	49 %	37 %
X	75 %	72 %	55 %
Y	43 %	46 %	100 %

Table 6.6: *Mean amplitudes for the different components of the Grevelingen survey.*

3. **Evaluation:** This site is very good for P-wave reflection profiling due to the absence of the weathered layer. S-wave reflections, however, seem to be absent. The data are dominated by dispersive low-velocity surface waves.

6.3.3 Flevoland: 3-component noise spread

1. **Settings and targets:** This survey was carried out in May 1997 on a grass field in the Hosterwold near Zeewolde, Flevoland. The area is part of the former North Sea

inlet called Zuiderzee, now polder land. This region was on the border of the ice cap during the Saalian and the genesis of the deep basin (125 m) is explained by glacier surge (Zagwijn (1974)). The basin was then filled by alternating sequences of sand, clay and also peat. There are two26 G-124), the other approximately 2 km to the north (26 G-34, continued as 26 G-36). While the one to the north shows very similar lithology to the Nieuwegein site for the upper 20 m, the peat layer is absent in the borehole to the east (see Fig. 6.10).

Given the geologic history of the side it was expected to record reflections from a number of interfaces deposited during the filling of the basin. The S-vibrator was unfortunately not available for this survey, so we decided to use the railway sleeper source in order to test this source and to look for possible SH-wave reflections.

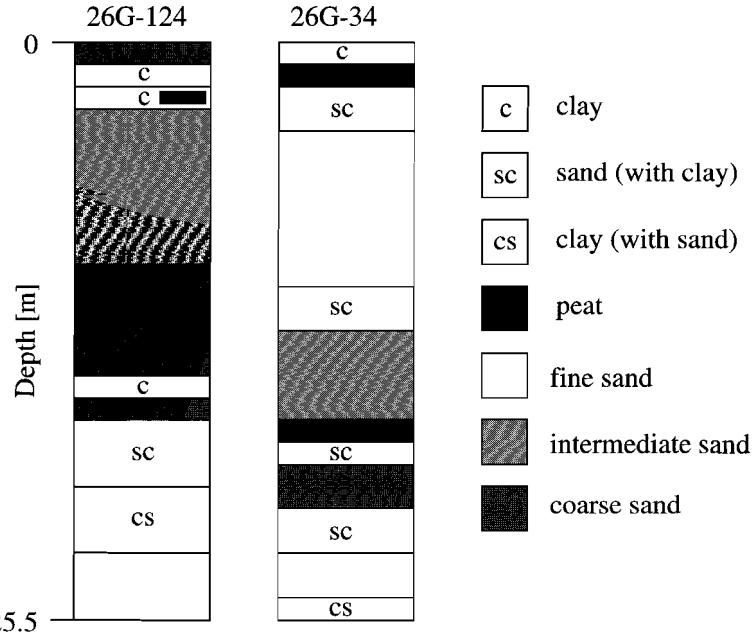

Figure 6.10: *Lithology from two boreholes near the area of the Flevoland survey. 26G-124: Borehole to the east. Note the absence of a peat layer. 26G-34: Borehole to the north.*

2. **Results:** Table 6.8 gives an indication about the relative amplitudes on the components. Note, that for these data all individual shot records were vertically stacked. The main energy, as expected, is recorded on the y-component and above all consists of dispersive Love waves and shear wave refractions. The velocity of the low-frequency part of the fundamental mode of the Love wave is roughly 60 m/s. Summing and subtracting records from opposite strokes leads to the panels shown in Fig. 6.11.

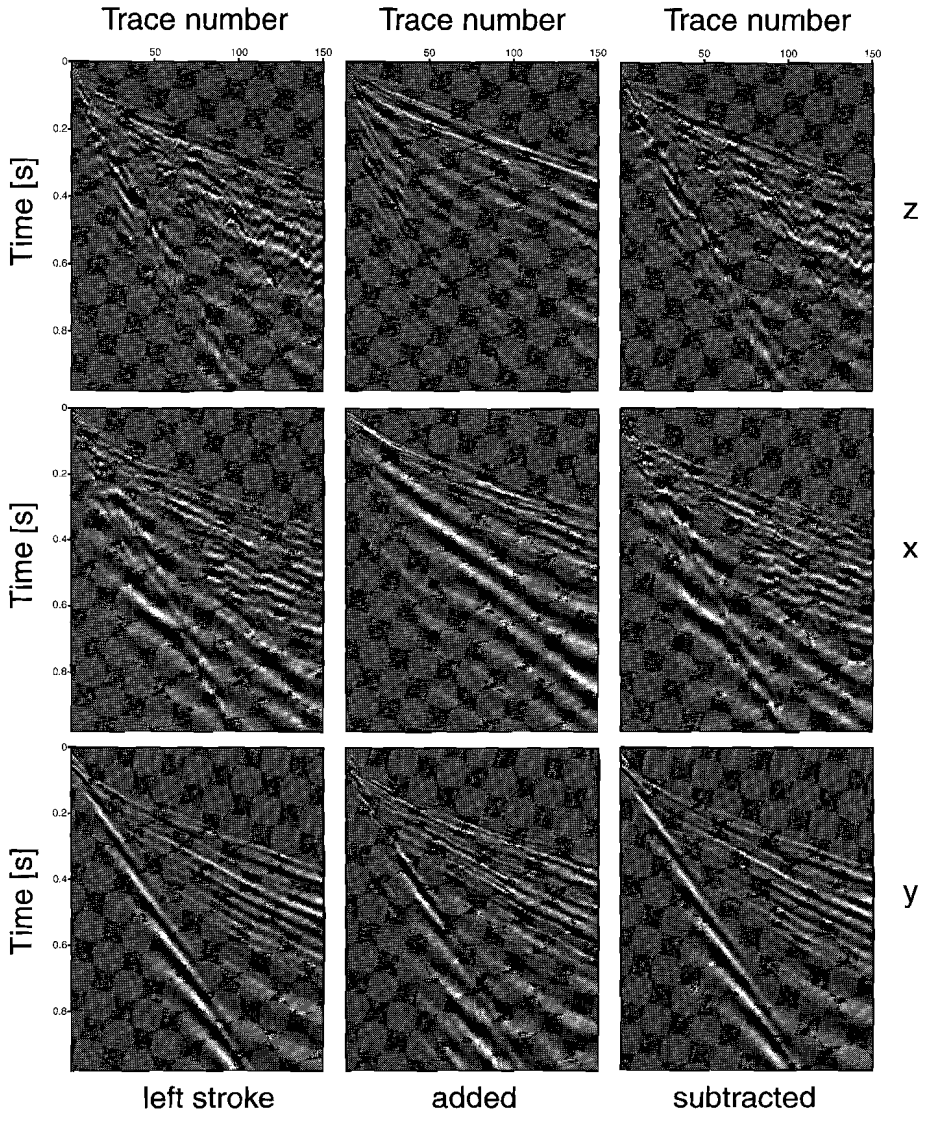

Figure 6.11: *Flevoland survey: Original data from left stroke (left-hand side) and the added (middle) and subtracted (right-hand side) panels for opposite strokes. The letters on the right-hand side indicate the receiver component. Individual trace scaling was used for plotting.*

source	railway sleeper
number of shots at same location	5 (shot #1, #2) or 10
number of geophones	15
spread shifted	10 times
minimum offset	0.5 m
maximum offset	74.5 m
geophone distance	0.5 m

Table 6.7: *Acquisition parameters for the Flevoland survey.*

	z	x	y
left	16 %	25 %	100 %
right	17 %	26 %	99 %
add	3 %	5 %	5 %
subtract	16 %	24 %	100 %

Table 6.8: *Mean amplitudes for the different components of the Flevoland survey and for the added or subtracted panels. Left and right stroke differ slightly. Trace balancing for each side was therefore performed independently.*

Figs. 6.11 and Table 6.8 indicate that only little P-wave energy was radiated by the railway sleeper source. Visually, there is no difference between the original y-component panel and the subtraction panel, which should enhance SH-waves. This indicates that the railway sleeper is a nearly pure SH-source. The added z- and x-component panels show events different from the subtracted panels: the dispersive Love wave is only visible on the subtracted panel, events seem to be more continuous on the added panels, and the air wave becomes visible (first arrival). There are no P-wave reflections visible on the added z-component before the air wave (checked with AGC). An extremely deep groundwater table could explain this absence, but is unlikely for this location. A peat layer close to the surface mat have blocked the P-wave energy instead (see Fig. 6.10, borehole G26-34).

3. **Evaluation:** Using the railway sleeper as source resulted in data dominated by Love wave and shear refractions. No P-wave energy seems to be present. It would be advisable to repeat the survey using a P-wave source in order to confirm this observation.

6.4 Two-component wavefield separation

6.4.1 Nieuwegein

The Zz- and Zx-components of shot #11 of the data recorded in Nieuwegein (see Fig. 6.3) were subjected to the iterative approach to see how much of the coherent energy on the records could be extracted and identified. Each data window was positioned such that a coherent wavefield, visible over a number of traces, was placed in its middle. Then an estimation of the parameters of this wavefield was attempted. After a first estimation the parameters of this dominant wave were interpolated. If there were no coherent parameters for the second wave over a number of analysis windows, it was tried to choose its parameters such that the energy of the dominant wave was best preserved. Several repetitions of this procedure were necessary to finally obtain a good estimate. The decision to continue with the next iteration was based on a visual comparison between the residual and the input data. After each iteration the mean energy level of each component was checked too. The results are shown in Fig. 6.13. The final estimates for each iteration which were used in the separation are listed in Table 6.9. Parameter estimation was always carried out for two waves. That allowed us to keep the analysis window small. Additionally, we run a parallel analysis using 15 traces. This often helped in smoothing the estimates for the short analysis windows, which often showed large scattering. We used the phase difference to group the parameter estimates because it was the most robust estimate.
In the following we give a brief explanation of the results achieved for each iteration. Fig. 6.12 shows the corresponding residual data sets, starting from the results after iteration #1. The solid lines in each panel of Fig. 6.12 indicate the data window that will be used for the next iteration.

1. **Iteration #1:** The Rayleigh wave is clearly the dominant wave. Using 5 traces in the analysis its parameters were determined. The energy of the lower amplitude wavefields could best be prevented from being mapped on the Rayleigh-wave panel by choosing a P-wave as second wave.

2. **Iteration #2:** In this and all following iterations 7 traces were used in the analysis. In the residual data after iteration #1 two strong waves are visible. One mainly on the Zz-, the other on the Zx-component. The estimation resulted in parameters for both waves, the one on the Zz-component having Rayleigh-wave character, that on the Zx-component S-wave character. In this iteration, the Rayleigh-type wave was removed. This wave is probably an S-wave arriving at the surface at an angle of incidence greater than the critical angle. The influence of the free surface makes this SV-P coupled system look like a Rayleigh wave. The arrival time of this wave coincides with that of an S-wave reflection from the clay-sand interface (inferred from VSP measurement).

3. **Iteration #3:** Now the S-wave mainly visible on the Zx-component was estimated together with a wave showing variable parameters, but generally lower apparent slowness. The character of the S-wave changes roughly half-way the spread: it

appears to be more low-frequent. This wave is too fast for a direct or refracted S-wave. It might be a converted wave.

4. **Iteration #4:** Now we tried to isolate the expected S-wave reflection arriving at 100 ms. The estimates however, showed a P-wave and parameters of a Rayleigh-type wave (which in iteration #6 was then confirmed as the S-wave reflection). The P-wave parameters mapped a number of arrivals on the output panel, but their interpretation is difficult. The problem may be due to the fact that the wave we want to isolate is actually not dominant. As shown in iteration #6 and #7 there are several events of somewhat equal amplitude that interfere with each other.

5. **Iteration #5:** This time a pro-grade Rayleigh wave showed up in the estimates. It arrives shortly before the fundamental mode and is interpreted as the first higher Rayleigh-wave mode. An S-wave was used as second wave to isolate the first higher mode well.

6. **Iteration #6:** We returned to the suspected S-wave arrival at 100 ms. A Rayleigh wave was estimated (due to the influence of the free surface). Projection was difficult and in the output panel no clear arrival is visible but rather a band of arrivals. As second wave an S-wave was estimated.

7. **Iteration #7:** We now concentrated on the S-wave from the previous iteration which had been estimated as second wave. We probably chose the time window not well, so the S-wave is mapped as a band of arrivals with a rather high apparent velocity.

8. **Iteration #8:** Now we attempted to isolate the arrival at 200 ms. This is the S-wave reflection from the Holocene/Pleistocene sand interface. Its parameters are highly variable and tend to Rayleigh wave and, very surprisingly, P-wave values. The isolated energy has no coherent waveform.

9. **Iteration #9:** There is a low-velocity low-frequency arrival at 200 ms, mainly on the Zz-component. Its parameters indicate that this is Rayleigh-wave energy.

10. **Iteration #10:** Lastly it was tried to identify the high-velocity high-frequency event early in the record. It was identified as S-wave energy and so we might have found another converted wave (compare with iteration #3).

Fig. 6.13 shows the decrease in mean energy for the original data (iteration #0) and for the residual data from all iterations. There is a sharp drop after the removal of the fundamental mode Rayleigh wave. The decrease in energy often occurs mainly on one of the receiver components, e.g. from iteration #1 to #2 on the Zz-component. From iteration #6 on there is only slight decrease although the residual data shown in Fig. 6.12 indicate that we still can explain coherent events. These coherent arrivals do not have significantly different amplitudes compared with other events inside the data window. Therefore, the additionally mapped energy caused by incorrect parameter estimation for the non-selected events shows up in the output panels of the selected waves.

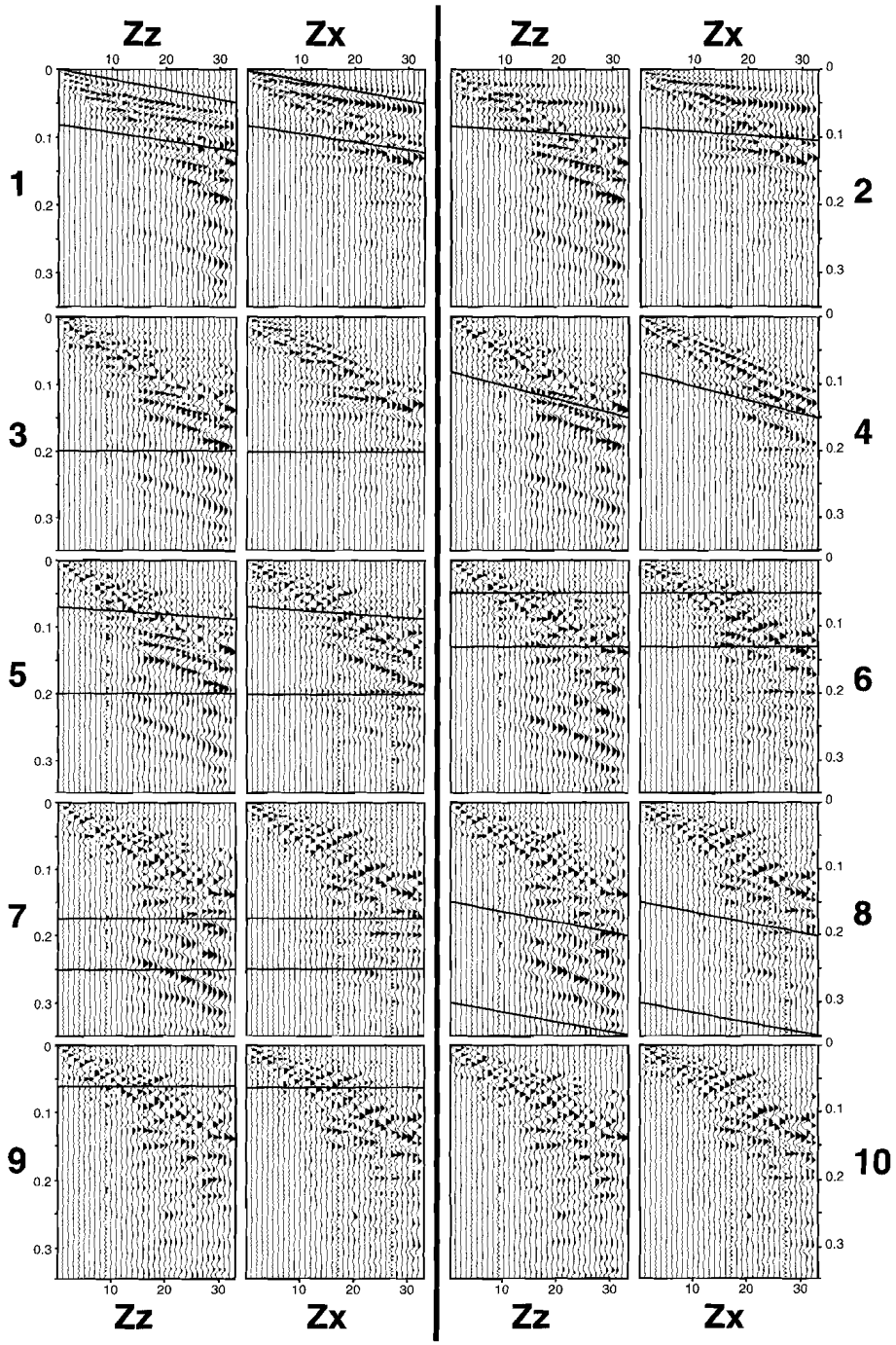

Figure 6.12: *Analysis of the Nieuwegein data: Residual data for all the 10 iterations after subtraction of the respective dominant wave. The solid lines indicate the data window that was used for the next iteration. Note, that each panel is scaled individually.*

Iteration	wave-type	ξ [°]	θ [°]	p [s/km]
#1	R	≈-90	60/73	8.2-5.7
	P	180	20	0.625
#2	R	≈-80	≈50/≈75	4.25-2.6
	S	0	30	1.5
#3	S	0	30	2.5-1.5/1.5
	P/R	≈150/≈-100	var	↓
#4	P	180	40-30	≈1.5
	R	-90	60	3.5
#5	R	120	20	8-6.5
	S	0	70	2-4
#6	R	var/≈-80	≈55	≈4
	S	≈10	≈55	≈1
#7	S	≈20	var	var
	P	180	var	var
#8	P/R	≈180/≈100	var	var
	R	≈-100	≈70	var
#9	R	≈-90	≈70/≈60	var
	R	≈100	var	var
#10	S	≈10	var	var
	R	≈-70/≈-90	var	var

Table 6.9: *Analysis of the Nieuwegein data: List of the parameters used in iteratively separating one coherent wave at a time from other arrivals. For an explanation of the symbols see Table,5.3.*

6.4.2 Grevelingen

The analysis shown in Fig. 6.9 did not reveal any S-wave reflections. It was suspected that there are S-wave reflections inside the Rayleigh-wave cone. Therefore, we attempted to estimate the parameters of the surface wave and subtract it from the data. There were 3 bad traces in the data which we filled in using a limited aperture τ-p forward and inverse transform. Since it was not applicable to the 4th trace in the panel we use the data only from trace 5 on, which results in a total number of 60 traces (compare with Fig. 6.7, which has the original 64 traces). In a first attempt the slowness was assumed to be constant with frequency (using 11 traces in the analysis). The data window was chosen to be around the Rayleigh-wave cone. In the first iteration the parameters of the fundamental Rayleigh-wave mode were estimated (see Table 6.10). Then we extracted the first higher mode, having a pro-grade ellipticity. The original data and the residual data after the second iteration are shown in Fig. 6.15. There is still much energy left in the Rayleigh-wave cone, but it is not coherent. A third iteration was attempted, but the analysis gave no conclusive results.

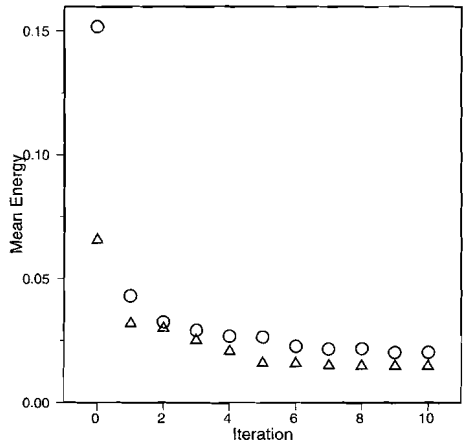

Figure 6.13: *Mean energy of Zz- (circles) and Zx-component of Nieuwegein data for each iteration. For comparison: the mean energy of the noise, taken from the last 50 ms of the original data, is approximately one order of magnitude smaller than the values given for iteration #10. The curves flattens out so quickly because there are still some high-energy fragments present in the region originally covered by the Rayleigh wave.*

Iteration	wave-type	ξ [°]	θ [°]	p [s/km]
#1	R	≈-90	≈50/≈55	≈10-≈8.5
	R	≈100	var	≈8-≈6
#2	R	≈100	54	≈8/≈7
	S	≈4	27	≈5

Table 6.10: *List of the parameters used in separating a dominant wave from the weaker arrivals for the Grevelingen data. For an explanation of the symbols see Table,5.3.*

In a second attempt we used a frequency dependent slowness directly estimated from the data (see Fig. 6.14). 9 traces were used in the analysis. The estimate for the higher slowness event is not complete beyond 100 Hz due to phase wrapping. Using the frequency-dependent slowness curves estimated for each analysis window did however not lead to a better separation (see Figs. 6.15b and 6.15c and Fig. 6.16). Interestingly, the polarisation angle also shows a dispersive behaviour. In contrast to Fig. 5.14, the angle increases for increasing frequencies, which means that the Poisson's ratio increases, implying that the increase of velocity with depth is greater for the S-wave than for the P-wave.

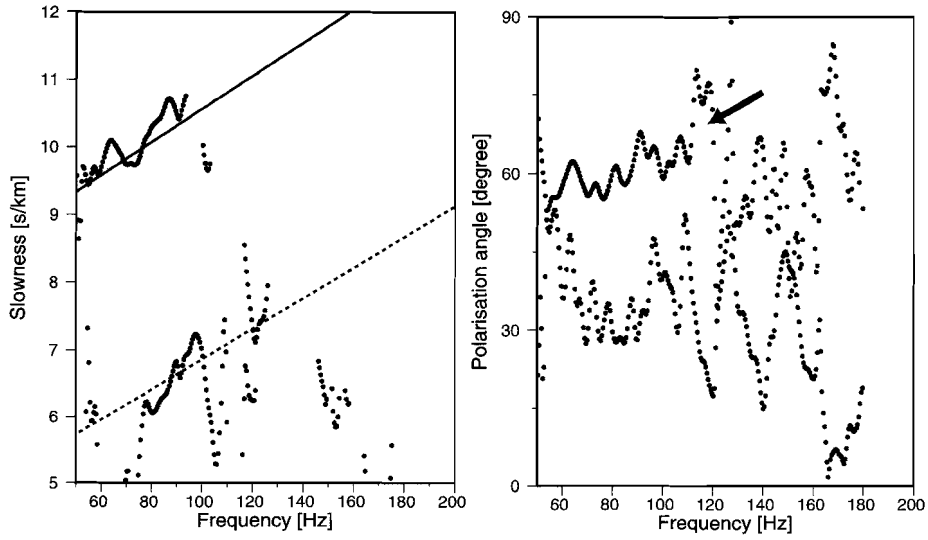

Figure 6.14: *Grevelingen data: Estimated slowness and fit for dispersion curve from the analysis of traces #30 till #38 (left-hand side). Right-hand side: polarisation angle for the same analysis window.*

6.5 Three-component wavefield separation

If the source is positioned inline, anisotropy is weak, the medium is stratified roughly horizontally and receivers are planted correctly (i.e. the inline-horizontal component is aligned with the spread direction), then events should be either recorded on the crossline-horizontal component or on the two other receiver components. The real data used for wavefield separation in this chapter contain events that are visible not only on the vertical and/or inline-horizontal, but also on the crossline-horizontal component (Fig. 6.3). Table 6.2 however shows for the Nieuwegein data that although the Rayleigh wave is recorded on the y-component, its energy is much smaller.

The extension of the method for application to three-component data was discussed in Chapter 2, but so far, examples illustrating the application of the extended method to synthetic data have not been shown. We refer at this point to the graduation thesis of Böhm (1999). He showed that three-component wavefield separation based on tracing back the slowness values did result in the correct individual wavefields. This also holds for data where noise was added. Estimation however failed for his example where 6 waves were present in the data. He finally showed that the Rayleigh wave on shot #1 of the Nieuwegein data, although only weakly present on the crossline-horizontal component, could be removed from all three receiver components, using 15 traces in the analysis. In the following we use the data from shot #11.

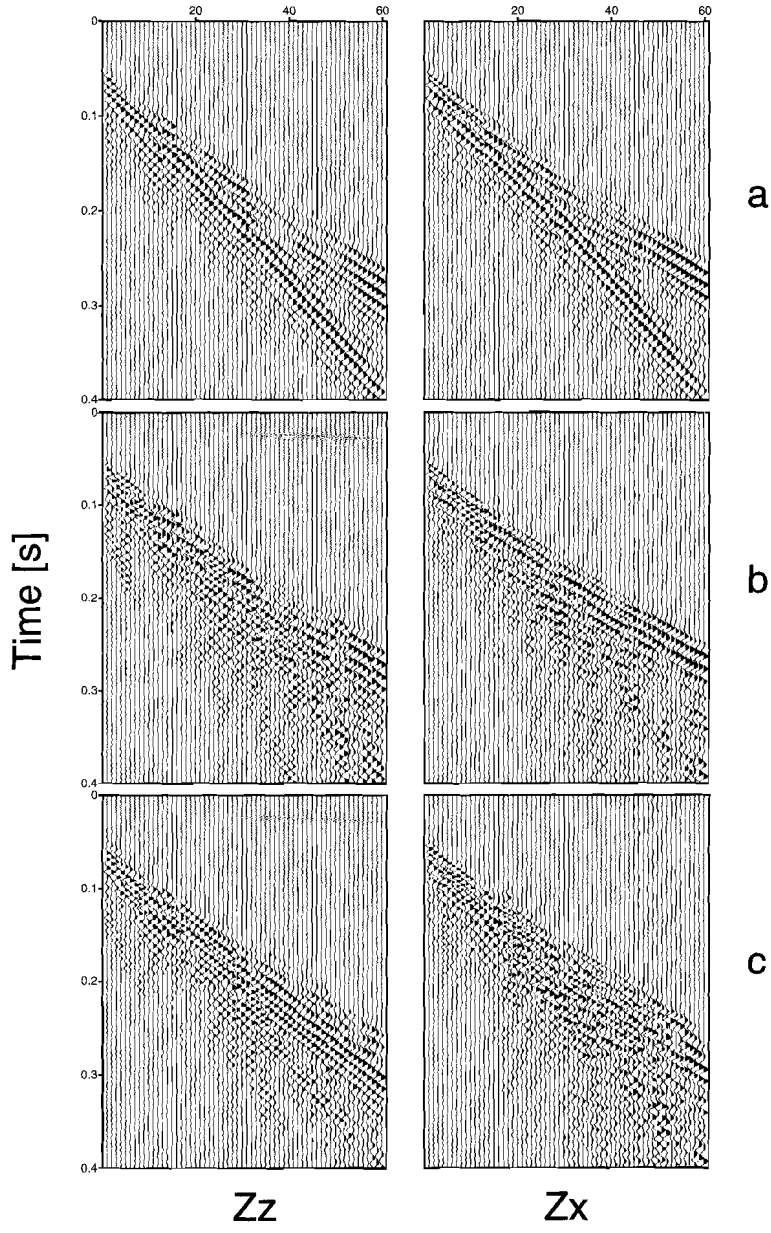

Figure 6.15: *Grevelingen noise spread: Comparison between a: Original Zz- and Zx-component. b: Residual data after second iteration, dispersion not taken into account. c: Residual data after second iteration, dispersion taken into account*

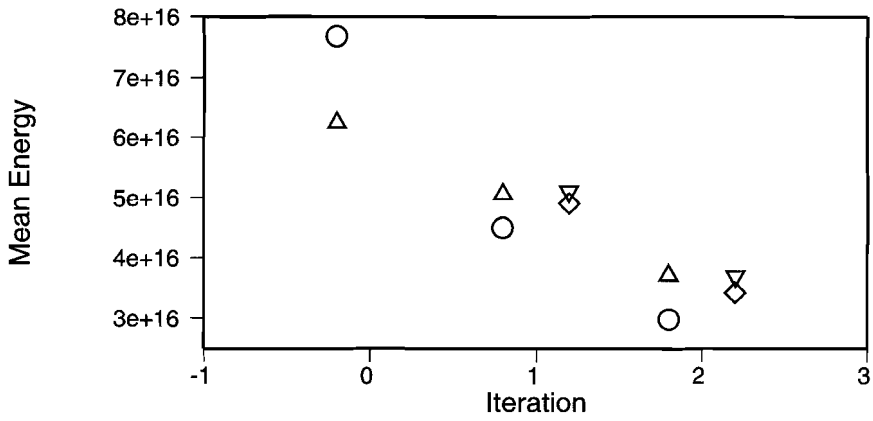

Figure 6.16: *Grevelingen noise spread: Mean energy of Zz- (circles) and Zx-component without taking dispersion into consideration. With dispersion we get the values represented by the inverted triangle (Zz) and the diamond (Zx). Note that the values are plotted with slight offset to their respective x-value for clarity.*

6.5.1 Nieuwegein: P-wave source

First, we attempted to remove the Rayleigh-wave energy from all three receiver components of shot #11 with (P-wave vibrator as source). This wave is also weakly present on the y-component. The data window was chosen to be the same as in the two-component analysis, but 7 instead of 5 traces were used in the analysis. The estimated parameters for the Rayleigh wave were similar to those for the two-component analysis (compare Table 6.11 with the iteration #1 in Table 6.9). The other two estimated waves resembled a P- and an S-wave, but their parameters were not consistent over the data window. Two waves with the very same parameters as for iteration #1 and #2 for the two-component data were then introduced to improve the separation procedure. The result after subtraction of the Rayleigh wave is shown in Fig. 6.17. The mean energy on the Zz-component was reduced to 33 % of that of the original data, and the Zx- and Zy-components to 51 and 75 %, respectively. For comparison, the two-component separation was a bit more successful: 28 and 49 % for Zz- and Zx-component, respectively. The separation was then repeated using also for the Rayleigh wave exactly the same parameters for slowness, polarisation angle and phase difference, which had been determined for the two-component separation. The values for directional angle and the phase difference between the horizontal component were taken from the previous estimation. The new mean energy percentages are 34, 51 and 76 % for Zz-, Zx- and Zy-component, respectively, which is a marginally worse result. The Rayleigh wave therefore has to be described by somewhat different parameters if we include the Zy-component, although the total energy on this component is weak. On the other hand, Rayleigh-wave removal is slightly better, if we only use two-component data, which indicates that the Rayleigh-wave energy on the Zy-component is less coherent.

wave-type	ξ [°]	θ [°]	p [s/km]	ζ [°]	ψ [°]
R	≈-90	60/73	8-6	50/80/110	≈20
S	0	30	1.5	0	0
P	180	20	0.625	0	0

Table 6.11: *Three-component analysis of the Nieuwegein data: List of the parameters used in separating a dominant wave from the weaker arrivals. For an explanation of the symbols see Table 5.3.*

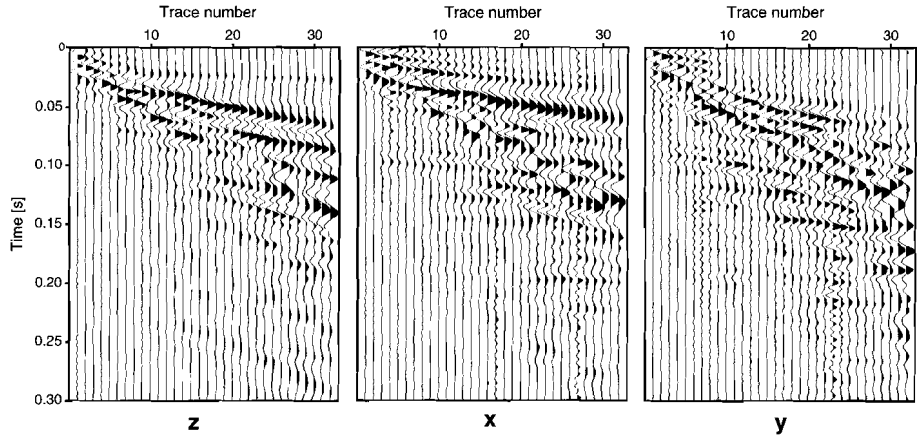

Figure 6.17: *Three-component wavefield separation: Residual data after subtracting the Rayleigh wave from the original Nieuwegein data (see Fig. 6.3). The letters below indicate the receiver components. Each panel has individual trace scaling.*

Further analysis of the wavefields analogous to the steps taken in Section 6.4.1 was not as successful. Most of the waves on the Zz- and Zx-component are hardly present on Zy. It is therefore very difficult to find appropriate parameters for the directional angle and the phase difference between the horizontal components, which may lead to a reduction of the mean energy on the Zy-component.

6.5.2 Nieuwegein: S-wave source

The analysis of the three-component data was repeated, this time using the data from the S-wave vibrator as source. For both source directions, X and Y, the Rayleigh wave was estimated well. The mean energy of the residual data sets after subtraction of the Rayleigh-wave are listed in Table 6.12. The Yy-component was not altered because the Rayleigh wave from the SH-source had no distinctive energy on this component.
Further analysis of the residual data did not result in stable estimates because the waves were not present on all components.

	z	x	y
Z	33 %	51 %	75 %
X	31 %	69 %	84 %
Y	52 %	76 %	100 %

Table 6.12: *Three-component analysis of the Nieuwegein data (S-wave vibrator): Mean energy for each residual data set after subtraction of the Rayleigh wave. The results for the P-wave source were added for comparison.*

6.6 Conclusions

The unsuccessful attempt to further analyse three-component data after removal of the Rayleigh wave for the Nieuwegein data is in contrast with the success on two-component data. The reason for this failure is that events recorded on the vertical and inline-horizontal component are present only weakly on the crossline-horizontal component and vice versa. The three-component wavefield separation is probably better suited for data which truly show events of similar energy on all the receiver components.

Appendix A

WINDOW PARAMETERS FOR ANALYSIS OF THE FD DATA SET

In Chapter 5 we analysed a noise-free data set modelled with an elastic 2D finite difference code. The window parameters for the different data windows are listed in Table A.1.

window	first trace	begin of window [ms]	end of window [ms]	last trace	begin of window [ms]	end of window [ms]
①	76	2180	2500	100	1970	2300
②	200	2300	2900	260	3100	3650
③	200	4250	5075	240	5100	5600
	241	4650	5175	259	5240	5860
	260	4750	5400	300	5250	5700

Table A.1: *Window parameters for the analysis of the FD data set.*

Appendix B

POLARISATION ANGLE OF RAYLEIGH WAVES

Wave equations for P- and SV-waves can be written in terms of potentials as (Sheriff and Geldart (1995)):

$$\begin{aligned} \nabla^2\Phi &= (1/\alpha^2)\frac{\partial^2\Phi}{\partial t^2} \\ \nabla^2\Xi &= (1/\beta^2)\frac{\partial^2\Xi}{\partial t^2}, \end{aligned} \tag{B.1}$$

where Φ and Ξ are P- and SV-waves potentials, respectively, and α and β are the P- and S-wave velocities, respectively. Rayleigh waves travelling along the free surface with amplitudes decaying away from the surface are solutions to Eqs. (B.1) with potentials:

$$\begin{aligned} \Phi &= Ae^{-m\kappa z}e^{i\kappa(x-V_R t)} \\ \Xi &= Be^{-n\kappa z}e^{i\kappa(x-V_R t)}, \end{aligned} \tag{B.2}$$

with V_R the Rayleigh wave velocity. Substituting Eqs. (B.2) into Eqs. (B.1) yields:

$$\begin{aligned} m^2 &= 1 - V_R^2/\alpha^2 \\ n^2 &= 1 - V_R^2/\beta^2 \end{aligned} \tag{B.3}$$

Applying the boundary conditions at $z = 0$ for the traction free surface finally leads to the following polynomial:

$$V_R^6 - 8\beta^2 V_R^4 + (24 - 16\beta^2/\alpha^2)\beta^4 V_R^2 + 16(\beta^2/\alpha^2 - 1)\beta^6 = 0.$$

The real root with a value $0 < V_R < \beta$ gives the Rayleigh wave velocity for a known Poisson's ratio. For a given S-wave velocity, n and m (Eqs. (B.3)) are known. The vertical and horizontal displacements can be computed from the potentials using:

$$\begin{aligned} u_3 &= \frac{\partial\Phi}{\partial z} + \frac{\partial\Xi}{\partial x} \\ u_1 &= \frac{\partial\Phi}{\partial x} - \frac{\partial\Xi}{\partial z}. \end{aligned} \tag{B.4}$$

Using Eqs. (B.2) at $z = 0$ with known parameters m and n we obtain for the displacements:

$$\begin{aligned} u_3 &= (-m\kappa A + i\kappa B)e^{i\kappa(x-V_R t)} \\ u_1 &= (i\kappa A + n\kappa B)e^{i\kappa(x-V_R t)}. \end{aligned}$$

If we use the amplitude relationship $B/A = i\frac{2m}{n^2+1}$ (from applying the boundary conditions) we can write for the displacement:

$$\begin{aligned} u_3 &= (-m - \frac{2m}{n^2+1})i\kappa A e^{i\kappa(x-V_R t)} \\ u_1 &= (1 + \frac{2nm}{n^2+1})\kappa A e^{i\kappa(x-V_R t)}. \end{aligned}$$

The polarisation angle for the Rayleigh wave can then be computed by taking the real part of the solution. This angle is plotted as a function of the Poisson's ratio in Fig. 5.14. Note, that (Sheriff and Geldart (1995)) use $-\Xi$ in Eqs. B.4 leading to the same polarisation angle.

References

Aki, K. and P. Richards (1980). *Quantitative seismology*. San Francisco: W.H.Freeman and Company.

Böhm, A. R. (1999). Wavefield separation using estimations of waveform characteristics. Master's thesis, Utrecht University.

Born, M. and E. Wolf (1964). *Principles of optics*. Pergammon Press, Oxford.

Brouwer, J., R. Ghose, K. Helbig, and V. Nijhof (1997). The improvement of geotechnical subsurface models through the application of S-wave reflection seismic exploration. In *Proccedings of the 3rd Meeting of the EGGS, Aarhus*, pp. 103–106.

Brouwer, J., R. Ghose, and V. Nijhof (1996). The use of vibratory sources in shallow shear-wave investigations. In *Proceeedings of the 2nd Meeting of the EEGS, Nantes*, pp. 355–358.

Brouwer, J. and K. Helbig (1998). *High-resolution seismic exploration*, Volume 19 of *Handbook of Geophysical Exploration: Seismic Exploration*. Elsevier Science Ltd.

Cho, W. H. (1991). *Decomposition of vector wavefield data*. Ph. D. thesis, Texas A&M University.

Cho, W. H. and T. W. Spencer (1992). Estimation of polarization and slowness in mixed wavefields. *Geophysics 57*(6), 805–814.

Dankbaar, J. W. M. (1983). The wavefield generated by two vertical vibrators in phase and counterphase. *Geophysical Prospecting 31*, 873–887.

Dankbaar, J. W. M. (1985). Separation of P- and S-waves. *Geophysical Prospecting 33*, 970–986.

Domenico, S. (1984). Rock lithology and porosity determination from shear and compressional wave velocity. *Geophysics 49*(8), 1188–1195.

Donati, M. S. and R. R. Stewart (1996). P- and S-wave separation at a liquid-solid interface. *Journal of seismic exploration 5*, 113–127.

Doornenbal, J. and K. Helbig (1983). High–resolution reflection seismics on a tidal flat in the Dutch Delta – acquisition, processing and interpretation. *First Break 5*, 9–20.

Ensley, R. (1984). Comparison of P- and S-wave seismic data: a new method for detecting gas reservoirs. *Geophysics 49*(9), 1420–1431.

Esmersoy, C. (1990). Inversion of P and SV waves from multicomponent offset vertical seismic profiles. *Geophysics 55*(1), 39–50.

Evans, R. (1984). Effects of the free surface on shear wavetrains. *Geophys. J. R. Astron. Soc. 76*, 165–172.

Gabriels, P., R. Snieder, and G. Nolet (1987). In situ measurements of shear–wave velocity in sediments with higher–mode rayleigh waves. *Geophysical Prospecting 35*, 187–196.

Ghose, R., J. Brouwer, and V. Nijhof (1996). A portable S-wave vibrator for high-resolution imaging of the shallow subsurface. In *58th EAGE Meeting, Amsterdam, Extended Abstracts*, pp. paper M037.

Greenhalgh, S. A., I. M. Mason, E. Lucas, D. Pant, and R. T. Eames (1990). Controlled direction reception filtering of P- and S-waves in τ-p. *Geophys. J. Int. 100*, 221–234.

Hemstra, N. (1999). P- and S-wave separation: A comparison of different methods. Master's thesis, Utrecht University.

Jin, S., R.-S. Wu, X.-B. Xie, and Z. Ma (1998). Wave-equation based decomposition and imaging for multicomponent seismic data. *Journal of seismic exploration 7*, 145–158.

Jongerius, P. and K. Helbig (1988). Onshore high-resolution seismic profiling applied to sedimentology. *Geophysics 53*(10), 1276–1283.

Kähler, S. and R. Meissner (1983). Radiaion and receiver pattern of shear and compressional waves as a functon of poisson's ratio. *Geophysical Prospecting 31*, 421–435.

Kneib, G., A. Kassel, and K. Lorenz (1999). Automatic seismic prediction ahead of the tunnel bore machine. In *Extended Abstracts of the 61st EAGE meeting, Helsinki*, pp. paper 4–45.

Krohn, C. (1984). Geophone ground coupling. *Geophysics 49*(6), 722–731.

Leaney, W. (1990). Parametric wavefield decomposition and applications. In *Expanded Abstracts*, pp. 1097–1100. Soc. Expl. Geophys.

Meissner, R. (1965). P– and SV–waves from uphole shooting. *Geophysical Prospecting 13*, 433–459.

Miller, R., S. Pullan, J. Waldner, and F. Haeni (1986). Field comparison of shallow seismic sources. *Geophysics 51*, 2067–2092.

Nijhof, V. P. B. J. (1989). Portable, high-frequency vibrator for high-resolution shallow seismic profiling. In *59th Annual Internat. Mtg., Soc. Expl. Geophys., Expanded Abstracts*, pp. 670.

Perelberg, A. I. and S. C. Hornbostel (1994). Application of seismic polarization analysis. *Geophysics 59*(1), 119–130.

René, R., J. Fitter, P. Forsyth, K. Kim, D. Murray, J. Walters, and J. Westerman (1986). Multicomponent seismic studies using complex trace analysis. *Geophysics 51*(6), 1235–1251.

Robertson, J. (1987). Carbonite porosity from S/P traveltime ratios. *Geophysics 52*(10), 1346–1354.

Robertsson, J. O., A., K. Hollinger, A. G. Green, and R. De Iaco (1996). Effects of near-surface waveguides on shallow high-resolution seismic refraction and reflection data. *Geophys. Res. Let. 23*(5), 495–498.

Sallas, J. J. (1984). Seismic vibrator control and the downgoing P-wave. *Geophysics 49*(6), 732–740.

Schalkwijk, K., K. Wapenaar, and E. Verschuur (1998). Decomposition of multicomponent ocean-bottom data in two steps. In *Expanded Abstracts*, pp. 1425–1428. Soc. Expl. Geophys.

Sheriff, R. and L. Geldart (1995). *Exploration Seismology* (2nd ed.). Cambridge University Press.

Squires, S. G., C. D. Y. Kim, and D. Y. Kim (1989). Interpretation of total wave-field data over Lost Hills field, Kern County, California. *Geophysics 54*(11), 1420–1429.

Steeples, D. W., A. G. Green, T. V. McEvilly, R. D. Miller, W. E. Doll, and J. W. Rector (1997). A workshop examination of shallow seismic reflection surveying. *The Leading Edge 16*(11), 1641–1647.

Tatham, R. H. and M. D. McCormack (1991). *Multicomponent seismology in petroleum exploration*. Society of Exploration Geophysicists.

van der Hoff, G. J., J. A. C. Meekes, K. Roy-Chowdhury, and B. C. Scheffers (1996). Source-depth optimisation in high resolution seismics. In *Proceedings of the 2nd Meeting of the Environmental and Engineering Geophysical Society (European Section)*, pp. 47–50. EEGS.

van der Veen, M., P. Wild, R. Spitzer, and A. Green (1999). Design characteristics of a seismic land streamer for shallow data acquisition. In *Extended Abstracts*, pp. 4–41. EAGE.

Wapenaar, C. P. A., G. C. Haimé, and A. J. Berkhout (1991). Elastic wavefield decomposition: Before or after extrapolation? In *Expanded Abstracts*, pp. 1001–1004. Soc. Expl. Geophys.

Winterstein, D. and M. Meadows (1991). Shear-wave polarizations and subsurface stress directions at lost hills field. *Geophysics 56*(9), 1331–1348.

Zagwijn, W. (1974). The paleogeographic evolution of the Netherlands during the Quaternary. *Geologie en Mijnbouw 53*, 369–385.

Epilogue

We have studied one out of many wavefield separation methods in detail and applied it with varying success to real data. The main advantage of the method, originally published by Cho and Spencer (1992), is that we do not need a priori information about the subsurface, which makes it attractive for shallow applications. The drawback of this method is that it depends heavily on data quality. Hemstra (1999) made a comparison between this method and the methods presented by Dankbaar (1985) and Esmersoy (1990). None of the methods is really superior to the others. Data quality and amount of a priori information available will determine which method gives better results. A general disadvantage of the data-dependent methods is their restriction to (small) data windows. It will therefore be difficult and laborious, but not impossible if the data quality is high enough, to analyse and separate waves from industry data. A general remark on successful wavefield separation can be stated as: the closer the individual wave types in the parameter spaces are, the better the quality of the data set has to be for a good estimation.

Shallow data recorded at the different sites have proven to be quite diverse in data quality as well as information content. We cannot yet recommend one of the sites for further research that will focus on combined inversion of the different wave-types. S-waves seemed to be absent on the Grevelingen site, while P-waves are strongly attenuated at the Nieuwegein site. The Flevoland survey should be repeated with vibratory sources to either confirm or contradict the absence of P-wave events.

Samenvatting

In de seismiek worden kunstmatige bronnen aan het aardoppervlak en in boringen gebruikt om elastische golven op te wekken. Men heeft vooral belangstelling in de in longitudinale richting gepolariseerde P-golven, waarmee men een seismisch beeld van de ondergrond verkrijgt. Naast de diepte van de grensvlakken wil men ook weten wat voor soort materiaal er is en welke eigenschappen het heeft, bijvoorbeeld de porositeit en de vorm van de poriën, de inhoud van de poriën (gas, olie, water) of de voorkeursrichting van scheuren. Deze parameter kunnen beter worden geschat met behulp van informatie afkomstig uit transversaal gepolariseerde S-golven. Verder is het ook nuttig om de informatie te gebruiken, die men uit de analyse van dispersieve oppervlaktegolven kan halen.
In de meer-komponenten seismiek poogt men dus met behulp van geschikte bronnen en ontvangers, die in elke richting van de ruimte gevoelig zijn, het totale golfveld op te nemen. Dataverwerking is noodzakelijk om de informatie uit de data te halen, en wordt het best voor elke golfsoort apart toegepast. Het is dus belangrijk dat van ieder aankomst in het seismogram de golfsoort bepaald wordt. Dit is moeilijk als de aankomsten met elkaar interfereren.
In de loop van de tijd zijn er veel verschillende methodes ontwikkeld om golven van elkaar te scheiden, elk methode met zijn voor- en nadelen. Men kan een onderscheiding maken tussen grofweg twee groepen: aan de ene kant filter- en elastische dekompositiemethodes, elk aangewezen op a priori informatie, en data-afhankelijke methodes aan de andere kant. Op basis van de datakwaliteit en de beschikking van a priori informatie moet men beslissen welke methode men wilt gebruiken.
In dit proefschrift wordt een van de data-afhankelijke methodes nader onderzocht met betrekking tot zijn toepassingsmogelijkheid en verder ontwikkelt. De methode is afkomstig van Cho and Spencer (1992) en heeft het voordeel, dat het voor elk golfsoort bruikbaar is, geen a priori informatie vereist en het toelaat, dat de parameters frequentieafhankelijk zijn. Alleen een afschatting van het aantal golven is nodig, dat men binnen een dataven-ster verwacht. De bepaling van de parameters (de horizontale slowness en de polarisatie) gebeurt binnen een analysevenster dat over het datavenster heen wordt geschoven. De minimale breedte van het analysevenster is afhankelijk van het verwachte aantal golven, de maximale breedte wordt door het gewenste oplossingsvermogen bepaalt. Niet of nauwelijks van belang is hoe sterk de golven met elkaar interfereren, of de bandbreedte hetzelfde is of dat de golven van dezelfde soort zijn. Het is alleen van belang dat de golven zich in de totaliteit van hun parameters van elkaar onderscheiden. De belangrijkste aanvaarding is de mogelijkheid, om de golven als platte golven te kunnen beschouwen, hetgeen betekent, dat de parameters binnen het analysevenster constant moeten zijn.
In **hoofdstuk 2** wordt de theorie waarop de methode gebaseerd is afgeleid en de extensie van twee- naar drie-komponenten data gedaan. Belangrijk is het berekenen van de zogenaamde transfer matrix, waarmee men in staat is de data van een ontvanger naar de volgende ontvanger te extrapoleren. Door middel van een eigenwaardeanalyse zijn de

gezochte parameters verkrijgbaar, waarmee de golfscheiding kan worden doorgevoerd. Zowel over methodieke als over op de data gebaseerde problemen gaat het in **hoofdstuk 3**. Bijvoorbeeld moet men er niet van uit gaan, dat één eigenwaarde alleen met één golf verbonden is voor alle frequenties. Een statistische analyse kan hier hulp bieden. Zij verbetert meteen ook de afschatting van de parameters als er ruis aanwezig is. Voor het geval dat de ruimtelijke aftasting te grof was en een golf aliasing-effekten vertoont, is er een aanpassing van de statistische analyse mogelijk. Als er aankomsten in de data zijn, welke qua amplitude sterk van elkaar verschillen, is het verstandig, om de methode iteratief toe te passen. Als er ruis in de data zit kan men naast een verbreding van het analysevenster, wat een verlaging van het oplossingsvermogen ten gevolge heeft, ook een dempingsfaktor invoeren. Verder werd de gevoeligheid van de methode met betrekking tot overeenkomst tussen twee signalen onderzocht en werd de statistische methode voor het bepalen van de parameters naar onderzoek van dispersieve golven uitgebreid.
Gemeten data kunnen vaak niet als vlakke golven worden benaderd. Als gevolg hiervan hoeft de schatting van de parameters niet helemaal te mislukken, maar verkrijgt men afwijkende waarden. Bijvoorbeeld is de invloed van de verweeringslaag op de aankomsttijden van groot belang. Overigens kan deze laag ook als natuurlijke golfscheider werken. De kwaliteit van de koppeling van de ontvangers aan de ondergrond heeft invloed op de gemeten amplitudes en het is dus verstandig om de ontvangers op dezelfde manier te koppelen, zoals veldtests in **hoofdstuk 4** aantonen. De invloed van het vrije oppervlak op de deeltjesbeweging kan men alleen meten, maar zonder verder informatie over de ondergrond is het niet mogelijk, om een correctie aan te brengen. Het wordt aangetoond hoe men in principe deze informatie uit de data met behulp van een inversie kan verkrijgen.
De toepassing van de methode op data uit de industrie wordt in **hoofdstuk 5** bekeken. Om in staat te zijn, de noodzakelijke laterale oplossing te behouden, moet men met datavensters werken, wat de methode nogal lastig maakt om toe te passen. Verder is het natuurlijk van belang in hoever de aankomsten als vlakke golven kunnen worden beschouwt. Terwijl de analyse van het eerste data set uit de industrie nog resultaten voor de dispersieve oppervlaktegolven opleverde, mislukte de toepassing op het tweede data set omdat de kwaliteit niet voldoende was. De golven in deze data set waren overigens al door de invloed van de verweringslaag min of meer gescheiden. Interessant was de frequentieafhankelijkheid van de polarisatie hoek afgeschat uit de analyse van dispersieve oppervlaktegolven (data set #1). De interpretatie komt met deze uit de analyse van de slowness overeen.
In **hoofdstuk 6** worden de data getoond welke met behulp van hoogresolutie meerkomponenten seismiek in Nederland zijn opgenomen. De bronnen waren twee minivibratoren, waarmee het mogelijk is, in tegenstelling tot impulsbronnen, een qua frequentie stuurbaar signaal de ondergrond in te zenden. Één meeting kon alleen maar worden voltooid met behulp van een horizontale impulsbron. Omdat in de hoogresolutieseismiek vaak geen a priori informatie beschikbaar is en de verweringslaag door de ondiepe penetratiediepte van de golven niet als golfscheider optreedt, is het mogelijk, dat de besproken methode de énige van toepassing is. Met behulp van de iteratieve aanpak was het mogelijk om uit de in Nieuwegein opgenomen data 10 verschillende golven te isoleren. De nauwkeurigheid van de bepaling hangt natuurlijk sterk af van de mogelijke benadering van de golven als vlakke golven en hun sterkte. Voor de bij de Grevelingendam

opgenomen data was het mogelijk om voor de interpretatie van zowel de slowness als de polarisatie hoek tot de dezelfde conclusie te komen. De inzet van de drie-komponenten methode heeft alleen zin als er ook echt energie van golven op alle drie de ontvangerkomponenten aanwezig is.

Zusammenfassung

In der Seismik werden künstliche Quellen an der Erdoberfläche oder in Bohrlöchern zur Erzeugung elastischer Wellen benutzt. Primär ist man an den longitudinal polarisierten P-Wellen interessiert, durch welche man ein seismisches Bild vom Untergrund erhält. Neben der Tiefenlage der einzelnen Grenzflächen ist man auch an der Art des Materials und seinen Eigenschaften interessiert, z.B. seine Porosität und die Porenform, der Poreninhalt (Gas, Öl, Wasser) oder die Vorzugsrichtung von Rissen. Diese Parameter kann man besser abschätzen, wenn man auch die transversal polarisierten S-Wellen in die Untersuchung einbeziehen kann. Zusätzliche Information kann die Analyse der dispersiven Oberflächenwellen bieten.

In der Mehrkomponentenseismik versucht man deshalb mittels geeigneter Quellen und Empfänger, die in alle drei Raumrichtungen empfindlich sind, das gesamte Wellenfeld aufzunehmen. Um die in den Daten vorhandene Information extrahieren zu können, müssen die Daten bearbeitet werden, am besten jede Wellenart gesondert. Dazu muß man für jeden Einsatz in den Seismogrammontagen die Wellenart bestimmen, was durch etwaige Interferenz der Einsätze erschwert wird.

Im Laufe der Zeit sind deshalb viele verschiedene Methoden zur Wellentrennung entwickelt worden, jede mit Vor- und Nachteilen. Man kann diese Methoden grob in zwei Gruppen einteilen: auf der einen Seite Filter- und elastische Zerlegungsmethoden, die beide angewiesen sind auf a priori Information, und datenabhängige Methoden auf der anderen. Je nach Datenqualität und vorhandener a priori Information sollte man die am besten geeignete Methode benutzen.

In dieser Dissertation wird eine dieser datenabhängigen Methoden auf ihre Anwendbarkeit überprüft und weiterentwickelt. Sie stammt ursprünglich von Cho and Spencer (1992) und hat den Vorteil, daß sie auf jede Wellenart anwendbar ist, keine a priori Information benötigt und die Bestimmung frequenzabhängiger Parameter zuläßt. Man benötigt nur eine Abschätzung der Anzahl der Wellen, die im gewählten Datenfenster vorhanden sind. Die Bestimmung der Parameter (horizontale Slowness und Polarisation) geschieht innerhalb eines Analysefensters, das über das Datenfenster geschoben wird. Die minimale Breite des Analysefensters wird durch die erwartete Anzahl der Wellen bestimmt, während die maximale Breite an das gewünschte laterale Auflösungsvermögen gekoppelt ist. Es spielt keine bzw. kaum eine Rolle, wie stark die Wellen miteinander interferieren, ob die Wellen denselben Frequenzinhalt haben oder ob sie vom derselben Art sind. Sie müssen sich nur in der Gesamtheit ihrer Parameter voneinander unterscheiden. Die wichtigste Annahme ist die Approximierbarkeit von Wellen als ebene Wellen, d.h. die Parameter müssen innerhalb des Analysefensters konstant sein.

In **Kapitel 2** wird die der Methode zugrunde liegende Theorie hergeleitet und die Erweiterung des Ansatzes von Zwei- auf Drei-Komponentendaten durchgeführt. Wichtig ist die Berechnung und Analyse der sogenannten Transfermatrix, die beschreibt, wie man die an einem Empfänger gemessenen Daten zur nächsten Empfängerposition extrapolieren

kann. Mittels einer Eigenwertanalyse erhält man dann die gesuchten Parameter, mit deren Hilfe man die Wellen voneinander trennen kann.
Mit sowohl methodischen als auch dateninherenten Problemen beschäftigt sich **Kapitel 3**. Zum Beispiel ist jeder Eigenwert nicht exklusiv für alle Frequenzen mit einer Welle verbunden. Eine statistische Analyse bietet hier einen Ausweg. Sie verbessert zusätzlich die Abschätzung der Parameter in der Anwesenheit von Rausch. Falls die räumliche Abtastung zu grob war und eine Welle aliasing-Effekte zeigt, kann man die statistische Analyse anpassen. Für Datenfenster, in denen die Einsätze stark unterschiedliche Amplituden haben, empfiehlt es sich, die Methode iterativ anzuwenden. Im Fall von Rausch kann man neben einer Verbreiterung des Analysefensters, was den Nebeneffekt hat, daß das laterale Auflösungsvermögen vermindert wird, auch einen Dämpfungsfaktor einführen. Weiterhin wurde die Sensitivität der Methode in bezug auf die Ähnlichkeit zweier Signale untersucht und die statistische Analyse auf dispersive Wellen ausgeweitet.
Gemessene Daten kann man oft nicht als ebene Wellen annähern. Die Parameterbestimmung muß deshalb noch nicht scheitern, aber man erhält verfälschte Werte. Zum Beispiel spielt der Einfluß der Verwitterungsschicht auf die Ankunftszeiten der Einsätze eine große Rolle. Übrigens kann diese Schicht auch als natürlicher Wellentrenner dienen. Die Güte der Ankopplung des Empfängers an den Untergrund beeinflußt die gemessenen Amplituden und sollte deshalb nicht zu unterschiedlich sein, wie Feldtests in **Kapitel 4** zeigen. Der Einfluß der freien Oberfläche auf die Partikelbewegung kann nur wahrgenommen, ohne zusätzliche Information über den Untergrund aber nicht korrigiert werden. Es wird gezeigt, wie man diese Information im Prinzip aus den Daten mittels einer Inversion ableiten kann.
Die Anwendbarkeit der Methode auf Industriedaten wird in **Kapitel 5** diskutiert. Um die notwendige laterale Auflösung zu erhalten, muß man die Anzahl der Wellen pro Analysefenster klein halten, d.h. man muß mit Datenfenstern arbeiten, was die Anwendung der Methode aufwendig macht. Weiterhin ist es natürlich wichtig, inwieweit die Einsätze als ebene Wellen angenähert werden können. Während die Analyse des ersten Industriedatensatzes noch Resultate für die dispersiven Oberflächenwellen ergab, scheiterte die Methode am zweiten datensatz ganz durch die unzureichende Datenqualität. Bei diesem Datensatz waren die Wellen übrigens schon mehr oder weniger durch den Einfluß der Verwitterungsschicht getrennt. Interessanterweise wurde eine Abhängigkeit des Polarisationswinkels mit der Frequenz für dispersive Oberflächenwellen festgestellt (Datensatz #1). Die Interpretation stimmte mit der aus der Frequenzabhängigkeit der Slowness gefundenen überein.
In **Kapitel 6** werden die mit Hilfe von hochauflösender Mehrkomponentenseismik in den Niederlanden gemessenen Daten vorgestellt. Als Quellen dienten zwei Mini-Vibratoren, die im Gegensatz zu Impulsquellen (z.B. Fallgewicht) ein im Bezug auf den Frequenzinhalt kontrollierbares Signal aussenden. Bei einer Messung konnte nur eine horizontale Impulsquelle eingesetzt werden. Da in hochauflösenden Experimenten oft keine a priori Information vorhanden ist und die Verwitterungsschicht wegen der geringen Eindringtiefe der Wellen nicht als natürlicher Wellenseparator dienen kann, kann die vorgestellte Methode eventuell die einzig anwendbare sein. Aus den in Nieuwegein aufgenommenen Daten konnten mit Hilfe der iterativen Methode 10 verschiedene Wellen isoliert werden. Die

Genauigkeit der bestimmung hängt natürlich von der Approximierbarkeit der jeweiligen Welle als ebene Welle und ihrere Amplitude ab. Für die Daten vom Grevelingendamm konnte ine konsistente Interpretaion für die Dispersionskurven von Slowness und Polarisationswinkel gefunden werden. Der Aufwand einer Drei-Komponentenanalyse lohnt sich nur, wenn Welen tatsächlich auf allen Komponenten anwesend sind.

End Credits

Producer
Jaap Mondt

Co-Producer
Kabir Roy-Chowdhury

The supervision committee
Jan Brouwer ❇ Henk Hake ❇ Jan Douma

Additional scientific advice
Axel Röhm ❇ Dirk Kraaijpoel ❇ Huub Douma

Technical Support
Henk van der Meer

Separation doubles
Abir Abdul Aziz ❇ Nanne Hemstra ❇ Alain Böhm

Parenting
Erika and Michael Richwalski

Additional parenting
Rita Verheij and Georg Richwalsky

Soundtrack available at
Harmonie Orchest Utrecht

No waves were harmed during separation

Extras
Everbody who has not been mentioned yet but has contributed either scientificly or non-scientificly to keep this project going.

THANKS !!!!!!!!!!

Curriculum Vitae

18 September 1969	Born in Bad Mergentheim, Germany
1976-1980	Primary School in Bad Mergentheim, Germany
1980-1989	Deutschorden-Gymnasium (secondary school) in Bad Mergentheim, Germany
1989-1995	Study of Geophysics at Karlsruhe University, Germany
1995-1999	PhD student (AIO) in the Exploration Geophysics group, Institute of Earth Sciences, Utrecht University, The Netherlands